

SPECTRUM OF LIGHT SCATTERED FROM
THERMAL FLUCTUATIONS IN GASES

by

Thomas John Greytak

S. B. and S. M., Massachusetts Institute of Technology

(1963)

SUBMITTED IN PARTIAL FULFILLMENT
OF THE REQUIREMENTS FOR THE
DEGREE OF DOCTOR OF
PHILOSOPHY

at the

MASSACHUSETTS INSTITUTE OF
TECHNOLOGY

June 1967

Signature of Author ...
Department of Physics, January 25, 1967

Certified by
Thesis Supervisor

Accepted by
Chairman, Departmental Committee
on Graduate Students

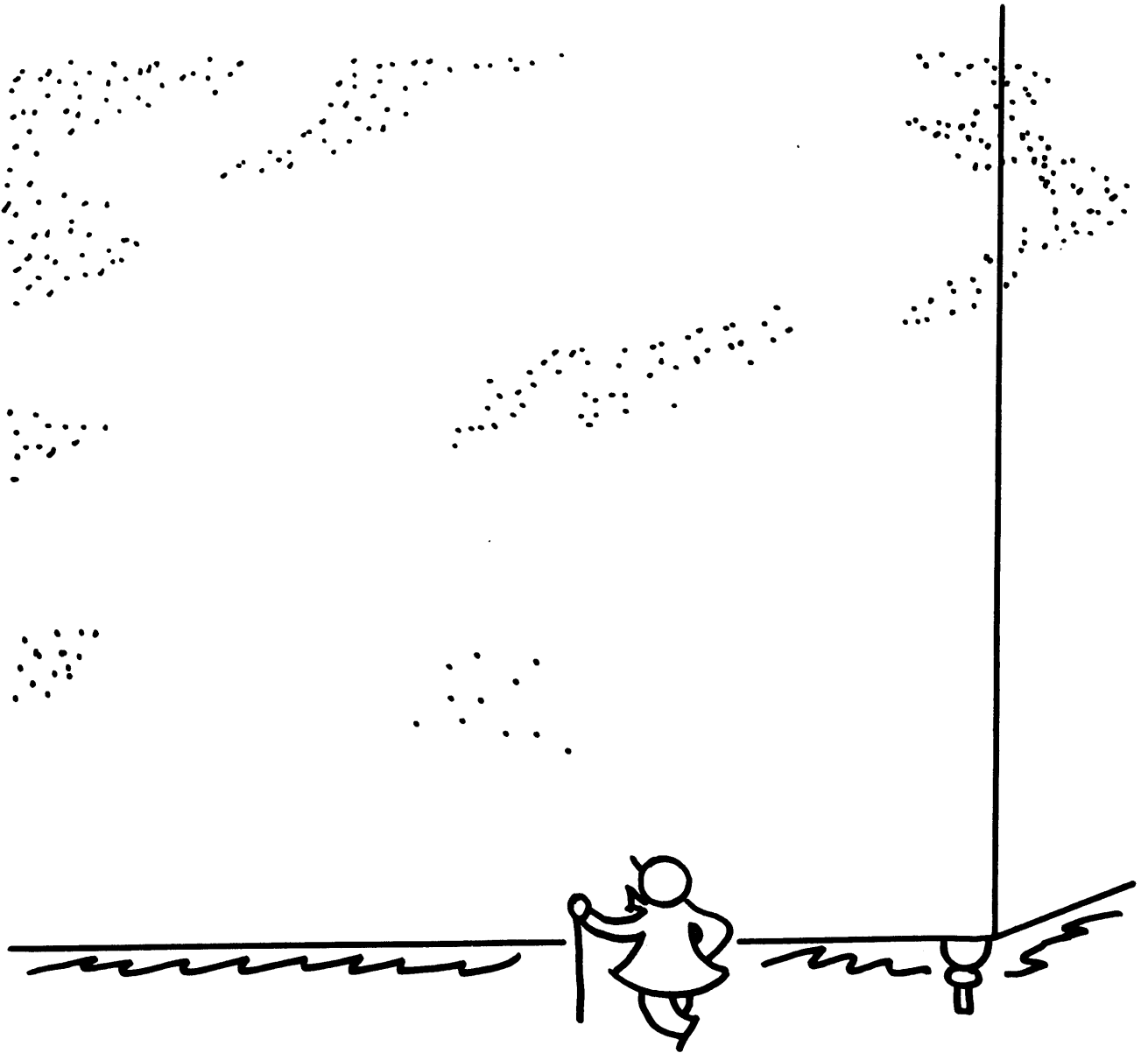
Prepared under
ARPA Contract SD-90
and a Grant from the
Sloan Fund for Basic Research (MIT)

SPECTRUM OF LIGHT SCATTERED FROM
THERMAL FLUCTUATIONS IN GASES

By

Thomas J. Greytak

Department of Physics
Massachusetts Institute of Technology
Cambridge, Massachusetts 02139



ATOMYRIADES *

Nature, it seems, is the popular name
for milliards and milliards and milliards
of particles playing their infinite game
of billiards and billiards and billiards.

* Piet Hein Grooks (MIT Press, Cambridge, 1966)

Spectrum of Light Scattered from
Thermal Fluctuations in Gases

by

Thomas John Greytak

Submitted to the Department of Physics on January 25, 1967, in partial fulfillment of the requirement for the degree of Doctor of Philosophy.

Abstract

This thesis is a study of the thermal fluctuations in five gases (Ar, Xe, N₂, CO₂, and CH₄) at a pressure of one atmosphere by the technique of inelastic scattering of light. The spectral power distribution is measured for density fluctuations whose characteristic wavelengths are 3.41×10^{-4} , 1.61×10^{-4} , and 3.18×10^{-5} cm, corresponding to scattering angles of 10.6° , 22.7° , and 169° respectively.

The spectra obtained are compared to theoretical ones computed for the following equations of motion for the fluctuations: the linearized equations of hydrodynamics, the linearized Krook equation, and the linearized Boltzmann equation for Maxwell molecules.

At 10.6° the spectra are well represented by hydrodynamics. The velocities and lifetimes of sound waves in the 100 MHz region are obtained. A detailed comparison between the experimental and theoretical spectra shows that a relaxation in the internal degrees of freedom of the polyatomic molecules must be taken into account in the hydrodynamic equations at these frequencies.

At 22.7° thermal diffusion and sound propagation are no longer completely independent modes of the medium and a 'sound velocity' is not well defined. The hydrodynamic equations, however, still describe the spectra in this region.

At 169° the spectra differ qualitatively from the hydrodynamic predictions and must be described in terms of kinetic theory. The theoretical spectrum for Maxwell molecules ($1/r^4$ repulsive potential) is in qualitative but not quantitative agreement with the data for Xe.

Table of Contents

<u>Chapter</u> I.	Introduction	8
<u>Chapter</u> II.	Theory	14
	A. Introduction	14
	B. Spectrum of the Scattered Light	16
	1. Derivation in Terms of the Density Correlation Function	16
	2. Connection between the Density Correlation Function, Conditioned Single Particle Distribution Function, and the Boltzmann Equation	38
	C. Approximate Solutions of the Boltzmann Equation	45
	1. Hydrodynamics	45
	2. Maxwell Molecules	54
	3. Kinetic Models	60
<u>Chapter</u> III.	Experimental Apparatus and Methods	69
	A. Introduction	69
	B. The Laser	72
	1. Description of the Laser	72
	2. Details of the Servo-Control System	73
	C. The Scattering Cell	78
	D. The Fabry-Perot Interferometers	87
	1. The Flat Fabry-Perot	87
	2. The Spherical Fabry-Perot	94
	E. The Photon Detection System	104
	F. Sensitivity	107

<u>Chapter IV.</u>	Experimental Results	111
	A. Scattering at 10.6°	112
	B. Scattering at 22.7°	127
	C. Scattering at 169°	132
	D. Calculation of the Experimental Efficiency	143
<u>Chapter V.</u>	Conclusions	147
Appendix A.	Calculation of Optical Path Lengths in the Spherical Fabry-Perot	149
	Acknowledgements	154
	Biographical Note	156

List of Illustrations

Fig. 2.1	Schematic arrangement of a light scattering experiment.	15
Fig. 2.2	Construction involved in the evaluation of the phases of the scattered waves.	27
Fig. 2.3	Effect of a finite beam diameter on the determination of the scattering vector.	37
Fig. 2.4	Construction involved in the interpretation of $G(r, t)$.	39
Fig. 3.1	Block diagram of experimental arrangement for forward scattering.	70
Fig. 3.2	Response of the laser to a change in the voltage on the piezoelectric element.	75
Fig. 3.3	Block diagram of the servo-control system.	77
Fig. 3.4	Full scale drawing of the scattering cell.	79
Fig. 3.5	A scattering cell using a conical reflector.	85
Fig. 3.6	Division and recombination of a ray in a flat Fabry-Perot.	88
Fig. 3.7	Path of a particular ray in a spherical Fabry-Perot cavity.	95
Fig. 3.8	Path of a general ray in a spherical Fabry-Perot cavity.	98
Fig. 3.9	The spherical Fabry-Perot mount.	102
Fig. 3.10	Pulse height spectrum for the phototube.	106
Fig. 4.1	Experimental traces taken at $\theta = 10.6^\circ$.	113
Fig. 4.2	Xe spectrum at $\theta = 10.6^\circ$.	120
Fig. 4.3	CO ₂ spectrum at $\theta = 10.6^\circ$.	121
Fig. 4.4	CH ₄ spectrum at $\theta = 10.6^\circ$.	122

Fig. 4.5	Effect of convolution on the spectrum of CH_4 at $\theta = 10.6^\circ$.	123
Fig. 4.6	Xe spectrum at $\theta = 22.7^\circ$.	129
Fig. 4.7	CO_2 spectrum at $\theta = 22.7^\circ$.	130
Fig. 4.8	Effect of convolution on the spectrum of CO_2 at $\theta = 22.7^\circ$.	131
Fig. 4.9	Experimental traces taken at $\theta = 169^\circ$.	133
Fig. 4.10	Xe spectrum at $\theta = 169^\circ$ and the hydrodynamic theory.	135
Fig. 4.11	Xe spectrum at $\theta = 169^\circ$ and the Krook model.	136
Fig. 4.12	Xe spectrum at $\theta = 169^\circ$ and the Maxwell molecule theory.	137
Fig. 4.13	Effect of convolution on the Maxwell molecule spectrum at $\theta = 169^\circ$.	138
Fig. 4.14	CO_2 spectrum at $\theta = 169^\circ$ and the hydrodynamic theory.	140
Fig. 4.15	Effect of a pressure increase on the spectrum of Xe at 169° .	142
Fig. A.1	End and side views of a ray in a spherical Fabry-Perot.	150

List of Tables

Table	Page
Table 2.1 Index of Refraction and Scattering Cross Section for Selected Gases	34
Table 2.2 Thermodynamic Parameters for Selected Gases	51
Table 2.3 Parameters Determining the Hydrodynamic Spectra of Gases	52
Table 3.1 Data for the Conical Lenses	83
Table 4.1 Brillouin Shifts and Velocities for Scattering at an Angle of 10.6°	115

Chapter I

Introduction

The spectral distribution of light scattered from thermal fluctuations in five gases (Ar, Xe, N₂, CO₂, and CH₄) has been measured⁽¹⁾ at one atmosphere using a frequency stabilized single mode laser, high resolution Fabry-Perot interferometers, and a detection system with a dark count of three photoelectrons per second. This spectrum is the space-time Fourier transform of the particle distribution function. The characteristics of the spectrum change as the scattering angle is increased from the forward to the backward direction; this corresponds to a transition from a hydrodynamic to a kinetic behavior of the fluctuations giving rise to the spectrum. Nelkin and Yip⁽²⁾ have recently proposed that experiments of this sort can be used as a test of the Boltzmann equation.

The experimental arrangement was first developed to study the velocities and lifetimes of thermally excited hypersonic sound waves⁽³⁾ and the lifetimes of entropy fluctuations⁽⁴⁾ in normal liquids. The sensitivity and resolution of the system were improved to their present state to study the spectrum of the light scattered from liquid helium below its λ -point. The measurements reported here on gases began as a check of the overall efficiency of the improved experimental arrangement. Preliminary results have subsequently been obtained in liquid helium, and a report of that work will be presented elsewhere.

The laser delivers 0.6 mW. at 6328 Å in a single longitudinal mode locked electronically to the bottom of the Lamb dip. The

scattering angles θ , are determined by conical lenses and the spread in angle accepted, $\Delta\theta$, is of the order of 10^{-3} radians. The scattering toward the forward direction was analyzed with a spherical Fabry-Perot interferometer⁽⁵⁾ of 750 MHz free spectral range and an instrumental profile of 28 MHz full width at half height. For the back scattering a flat Fabry-Perot was used of 4.96 GHz free spectral range and a width (depending on the reflectivity of the mirrors used) as narrow as 125 MHz. The light was detected with an uncooled ITT model FW 130 phototube. Pulse height discrimination⁽⁶⁾ was used to reduce the dark count to about three photoelectrons per second while maintaining an effective quantum efficiency of 2.5%. With this system the primary noise in the experiment was the shot noise due to the signal itself.

The fluctuations in the dielectric constant, ϵ , are responsible for the scattering of light. These fluctuations are caused, in turn, by the fluctuations in the density, in the temperature, and in the orientation of the molecules. In gases near one atmosphere the fluctuations in the number density, ρ , completely predominate. The probability per unit length $\sigma(\vec{K}, \omega)$ that a given photon in an incident polarized beam will be scattered into a region dK^3 about \vec{K} and $d\omega$ about ω can be shown to be

$$\sigma(\vec{K}, \omega) = \frac{\rho_0}{2\pi} \left(\frac{n^2 - 1}{4\pi\rho_0} \right)^2 k_0^4 \sin^2\phi$$

1.1

$$\times \iint dr^3 dt G(\vec{r}, t) \exp(i\vec{K} \cdot \vec{r} - i\omega t)$$

where $\omega/2\pi$ is the frequency shift of the scattered light, ϕ is the angle

between the electric field of the incident light and the wave vector \vec{k} of the scattered light, \vec{k}_0 is the wave vector of the incident light in the medium, n is the index of refraction of the gas and ρ_0 is its average number density. The wavevector of the fluctuation being observed \vec{K} is the vector difference between \vec{k} and \vec{k}_0 . Its magnitude is given by $K = 2k_0 \sin \phi/2$ since $k_0 \approx k$. $G(\vec{r}, t)$ is the classical limit of Van Hove's density correlation function⁽⁷⁾ in a homogenous medium:

$$G(\vec{r}, t) = \frac{1}{\rho_0} \langle \rho(\vec{0}, 0) \rho(\vec{r}, t) \rangle . \quad 1.2$$

Van Leeuwen and Yip⁽⁸⁾ have shown that for a dilute gas

$$G(\vec{r}, t) = \rho_0 + \int d\vec{v}^3 f(\vec{r}, \vec{v}, t) \quad 1.3$$

where $f(\vec{r}, \vec{v}, t)$ is the particle distribution function satisfying the linearized Boltzmann equation subject to the initial condition

$$f(\vec{r}, \vec{v}, 0) = \left(2\pi k_B T/m \right)^{-3/2} \exp \left(- \frac{m\vec{v}^2}{2k_B T} \right) \delta(\vec{r}). \quad 1.4$$

Here m is the mass of the molecule, k_B is the Boltzmann constant, and \vec{v} is the particle velocity. It follows that $\sigma(\vec{K}, \omega)$ is proportional to the double Fourier transform of the space and time distribution function for the gas molecules. The trace recorded experimentally is the convolution of $\sigma(\vec{K}, \omega)$ with the instrumental profile of the optical spectrometer.

The form of the spectrum of the scattered light is determined by

a parameter y which is a measure of the ratio of the wavelength of the fluctuation observed to the collision mean free path:

$$y = (2\pi/K) / (2\pi/\alpha) (2k_B T/M)^{1/2} \quad 1.5$$

where α is an effective collision frequency. When $y > 10$ the hydrodynamic description is very good. The spectrum consists of three distinct, non-overlapping lines: an unshifted component due to non-propagating fluctuations (the Rayleigh component) and a symmetrically shifted doublet due to the scattering from thermally excited sound waves (Brillouin scattering). In the region $y \sim 5$ the three lines begin to overlap since their widths increase faster with K than does their splitting; yet, the spectrum can still be described rather accurately by the hydrodynamic equations. However, when $y < 2$ the hydrodynamic equations no longer adequately describe the spectrum. A kinetic theory must be used to take into account the effects of the distribution in molecular velocities. At a pressure of one atmosphere each of these regions is investigated in turn by changing the scattering angle from the forward to the backward direction. This work represents the results of measurements at three scattering angles: 10.6° , 22.7° , and 169.4° . Previous measurements have been made at 90° in A and H_2 by May, Rawson, and Welsh⁽⁹⁾.

The experimentally measured spectra are compared with the theoretical spectra based on an exact solution of the linearized hydrodynamic equations recently obtained by Mountain⁽¹⁰⁾. At 169° the spectra are also compared with two kinetic calculations. One of these

is based on an exact solution of the linearized Boltzmann equation obtained by Ranganathan and Yip⁽¹¹⁾ for the special case of point molecules interacting by means of a repulsive $1/r^4$ potential (Maxwell molecules). The other kinetic spectrum which is compared to the data represents an exact solution⁽¹²⁾ of the linearized Krook equation⁽¹³⁾, which is the Boltzmann equation with the collision integral replaced by a phenomenological term that maintains conservation of particle number, momentum, and energy.

The results obtained in the kinetic region have a particular significance. It is shown that the inelastic scattering of light from gases can provide detailed information on the molecular distribution function and can serve as a delicate test of the validity of various theoretical solutions of the Boltzmann equation or its extensions to higher densities. This technique gives results which compliment those obtained by studying the transport coefficients and the propagation of forced sound waves. Formally, the transport coefficients are proportional to the integral over all time of various correlation functions in the medium⁽¹⁴⁾; in practice they are related to various integrals over the distribution function⁽¹⁵⁾. The forced sound wave experiments deal with the solutions of the boundary value problem⁽¹⁶⁾ in kinetic theory. The inelastic light scattering experiments, on the other hand, deal with a well-posed initial value problem⁽²⁾ in kinetic theory. They have the advantage of determining directly, for a certain range of wave vectors, the space-time Fourier transform of the distribution function.

References for Chapter I

1. This work was first reported in T. J. Greytak and G. B. Benedek, *Phys. Rev. Lett.* 17, 179 (1966).
2. M. Nelkin and S. Yip, *Phys. Fluids* 9, 380 (1966).
3. G. B. Benedek and T. J. Greytak, *Proc. IEEE* 53, 1623 (1965).
4. T. Greytak, *Bul. Am. Phys. Soc.* 11, 404 (1966).
5. P. Connes, *Jour. de Physique et le Radium* 19, 262 (1958).
6. E. H. Eberhardt, *IEEE Transactions on Nuclear Science* NS-11, 48 (1964).
7. L. Van Hove, *Phys. Rev.* 95, 249 (1954).
8. J. M. J. Van Leeuwen and S. Yip, *Phys. Rev.* 139, A1138 (1965).
9. A. D. May, E. G. Rawson, and H. L. Welsh in *Physics of Quantum Electronics*, edited by P. L. Kelley, B. Lax, and P. E. Tannenwald (McGraw-Hill, N. Y. 1965).
10. R. Mountain, *Rev. Mod. Phys.* 38, 205 (1966).
11. S. Ranganathan and S. Yip, *Phys. Fluids* 9, 372 (1966).
12. S. Yip and M. Nelkin, *Phys. Rev.* 135, A1241 (1964).
13. P. F. Bhatnagar, E. P. Gross, and M. Krook, *Phys. Rev.* 94, 511 (1954).
14. P. A. Egelstaff, *Reports on Progress in Physics* 29 part 1, 333 (1966).
15. S. Chapman and T. G. Cowling, *The Mathematical Theory of Non-uniform Gases* (Cambridge University Press, Cambridge, England, 1952).
16. L. Sirovich and J. K. Thurber, *JASA* 37, 329 (1965).

Chapter II

Theory

A. Introduction

In this chapter the classical theory of light scattering from a transparent medium is reviewed. Figure 2.1 shows the physical situation under consideration. A beam of monochromatic light with wave vector \vec{k}_0 and frequency $\omega_0/2\pi$ passes through the medium. The scattered light is characterized by a new wave vector \vec{k}_s and a frequency shift of $\omega/2\pi$. The scattering vector \vec{K} is defined as the difference between \vec{k}_s and \vec{k}_0 :

$$\vec{K} \equiv \vec{k}_s - \vec{k}_0. \quad 2.1$$

If the frequency shift is small, the magnitude of \vec{k}_s is equal to \vec{k}_0 to a term of order ω/ω_0 . These experiments deal with frequency shifts of $10^8 - 10^9$ Hz and the light frequency is about 5×10^{14} Hz so $\omega/\omega_0 \sim 2 \times 10^{-7} - 2 \times 10^{-6}$. In this case the magnitude of K is determined only by \vec{k}_0 and the scattering angle θ :

$$K = 2k_0 \sin \frac{\theta}{2}. \quad 2.2$$

The light which is scattered in a specific direction, and therefore corresponds to the specific K given by equation 2.2, is singled out for analysis by a lens and detector system.

In section B.1 the spectral power density $S_E(\vec{K}, \omega)$ of the

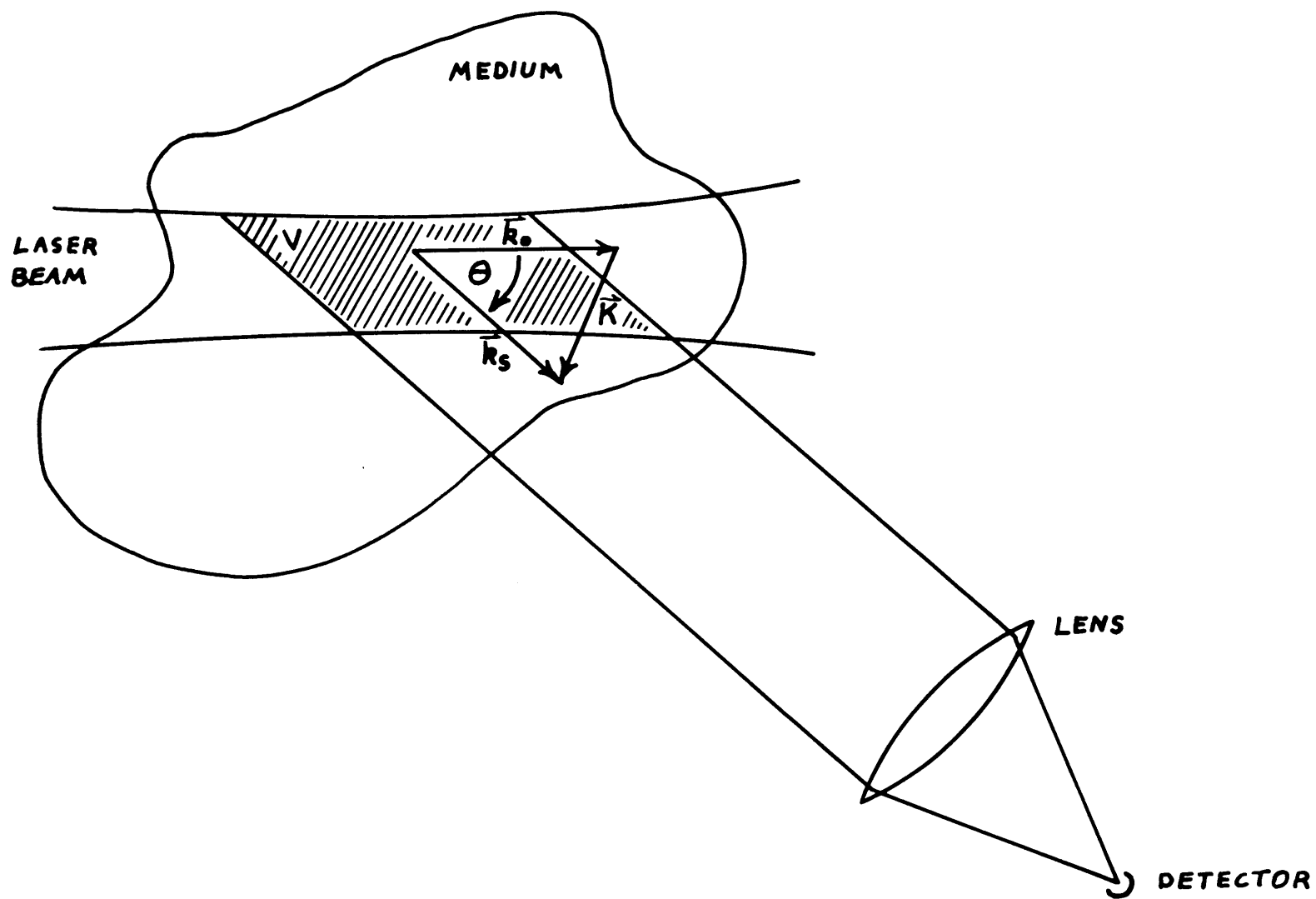


Fig. 2.1 Schematic arrangement of a light scattering experiment.

scattered electric field at the detector is introduced in terms of the time displaced correlation function of the field. $S_E(\vec{K}, \omega)$ is proportional to the fraction of the scattered intensity that corresponds to a scattering vector \vec{K} and a frequency shift $\omega/2\pi$. It is therefore also proportional to the differential inelastic cross section of the medium. The electric field at the detector is expressed in terms of the positions and orientations of the particles of the medium. After making suitable assumptions about the individual particle polarizabilities, S_E is shown to be proportional to the space-time Fourier transform of the density correlation function. In section B.2 it is shown that the density correlation function can be interpreted as the evolution of the particle distribution function in response to a specific initial condition. For a gas under suitable conditions this particle distribution function is demonstrated to be the space-time portion of the solution of the Boltzmann equation.

The Boltzmann equation cannot be solved in general, but approximate solutions have been obtained. In section C three classes of solutions are discussed. These give rise to the theoretical spectra which are compared with the experimental results in chapter IV.

B. Spectrum of the Scattered Light

1. Derivation in Terms of the Density Correlation Functions

The conventional approach to the scattering of light in a medium is a thermodynamic one.⁽¹⁾ One observes that electromagnetic plane waves will propagate undeflected in a continuous medium if the

dielectric constant ϵ is an absolute constant. Fluctuations in the dielectric constant $\delta\epsilon$ with some characteristic wave vector $\vec{\kappa}$ would, however, give rise to scattering in a direction determined by the Bragg condition:

$$\vec{\kappa} = \vec{K}. \quad 2.3$$

The dielectric constant is taken to be a thermodynamic variable of the medium and as such is expanded in a complete set of independent thermodynamic variables for the medium (for a simple fluid these are usually chosen to be either pressure P and entropy S , or density ρ and temperature T). The time correlation function of $\delta\epsilon(\vec{K}, t)$, which determines the frequency spectrum of the scattered light, is then expressed as the correlation function of a sum of the independent variables with coefficients (or coupling constants) which are thermodynamic derivatives. For example in a simple fluid one would have

$$\begin{aligned} < \delta\epsilon(K, t) \delta\epsilon(K, t + \tau) > = \\ < \left\{ \frac{\partial\epsilon}{\partial\rho} \Big|_T \delta\rho(K, t) + \frac{\partial\epsilon}{\partial T} \Big|_\rho \delta T(K, t) \right\} \times \\ \left\{ \frac{\partial\epsilon}{\partial\rho} \Big|_T \delta\rho(K, t + \tau) + \frac{\partial\epsilon}{\partial T} \Big|_\rho \delta T(K, t + \tau) \right\} >. \end{aligned} \quad 2.4$$

In this case if the equations of motion governing the thermodynamic fluctuations in $\delta\rho$ and δT are known along with the coupling constants, then the spectrum of the scattered light can be found.

The total light scattered corresponding to a given K (that is, the integral over the spectrum of frequency shifts) is proportional to the mean square fluctuation in $\delta\epsilon(K)$. This mean square fluctuation can be obtained from equation 2.4 by setting $\tau = 0$. In the resulting expression the cross term vanishes because the fluctuations in the independent variables taken at the same time are uncorrelated. It follows that

$$\langle \delta\epsilon(K)^2 \rangle = \left(\frac{\partial\epsilon}{\partial\rho} \Big|_T \right)^2 \langle \delta\rho(K)^2 \rangle + \left(\frac{\partial\epsilon}{\partial T} \Big|_\rho \right)^2 \langle \delta_t(K)^2 \rangle. \quad 2.5$$

By using the theory of thermodynamic fluctuations⁽²⁾ the mean square fluctuation in the independent variables in equation 2.5 may be evaluated directly in terms of such parameters of the medium as the specific heats, compressibility, and thermal expansion coefficient.⁽¹⁾ Therefore the total light scattered for a given K can be determined explicitly from the thermodynamic parameters of the medium, without a knowledge of the time dependence of the fluctuations.

The results stated above are independent of the particular set of independent variables chosen to represent the medium. In particular if the entropy and pressure had been chosen, equations 2.4 and 2.5 would be modified by the substitution of S for ρ and P for T . The advantage of choosing the variables S and P is that in the long wavelength region of hydrodynamic behavior, the equations of motion for the fluctuations have two independent normal modes, one governing only δP (sound waves, which are known to be adiabatic so $\delta S = 0$) and

one involving only δS (thermal diffusion which involves no pressure change so $\delta P = 0$). As a result $\delta P(K, t)$ and $\delta S(K, t + \tau)$ are uncorrelated for all τ and the equivalent of equation 2.4 for the $\delta\epsilon$ correlation function reduces to the sum of the correlation functions for each of the independent variables:

$$\begin{aligned} \langle \delta\epsilon(K, t) \delta\epsilon(K, t + \tau) \rangle = & \\ & 2.6 \\ \left(\frac{\partial\epsilon}{\partial S} \Big|_P \right)^2 \langle \delta S(K, t) \delta S(K, t + \tau) \rangle + \left(\frac{\partial\epsilon}{\partial P} \Big|_S \right)^2 \langle \delta P(K, t) \delta P(K, t + \tau) \rangle. \end{aligned}$$

This separation will break down, however, when the spectrum due to the first term (the diffusion mode with a spectrum centered about $\omega = 0$) starts to overlap the spectrum due to the second term (the sound waves whose spectrum is Doppler shifted by an amount $\omega = \pm v_s K$ where v_s is the sound velocity). This overlap is expected to occur for large values of K (short wavelengths of the fluctuations) since in the absence of dispersion the width of spectrum of each mode grows as K^2 while their separation only grows as K .

The thermodynamic approach to light scattering outlined above has two major defects which limit its applicability. First, there are some processes which give rise to scattering that cannot be described in terms of a macroscopic thermodynamic variable of the medium. An example of such a process is the fluctuation in the orientation of the molecules of the medium. These fluctuations make the instantaneous local dielectric constant anisotropic, and the scattering they cause contains a depolarized part. In liquids the amount of light scattered

by these fluctuations in the molecular orientation (referred to as anisotropy scattering) is of the same order of magnitude as that scattered by fluctuations in the thermodynamic variables.

The second defect of the thermodynamic approach lies in the fact that thermodynamics is basically an equilibrium theory. When one speaks of a local fluctuation in some thermodynamic quantity, the temperature T for example, it is understood that $\delta T(\vec{r}, t)$ represents a quasi-equilibrium state of a large number of molecules (large enough to determine a meaningful statistical average) in a region about the point \vec{r} . Also it is understood that the time variation of δT must be slow compared to the time which the molecules around \vec{r} require to adjust to the quasi-equilibrium state.⁽²⁾ For example if the population of the rotational energy levels of the molecules requires t_R seconds to adjust to a change δT , then $\delta T(\vec{r}, t)$ can only be defined for fluctuations whose characteristic behavior involves times much larger than t_R . If δT is changed with a frequency $\omega \ll 1/t_R$, then the population of the energy levels will follow the change, and the change in average energy of the molecules will be described by a certain specific heat which is independent of ω . Were ω to be increased until it was comparable to $1/t_R$, the population of the energy levels would not be able to follow the changes in δT . The specific heat measured under these conditions would be less than its low frequency value. This example suggests, therefore, that the assumptions about quasi-equilibrium break down at those frequencies at which thermodynamic parameters become frequency dependent.

Thermodynamics, because of its assumptions about equilibrium, is a low frequency theory and cannot be expected to apply to those frequencies at which the mechanical and thermal properties of the medium - for example specific heats, transport coefficients, and the coupling to the dielectric constant - become frequency dependent. From a hydrodynamic point of view, however, the dispersion in the velocity of sound observed in liquids and gases can only be explained on the basis of such frequency-dependent parameters.⁽³⁾ This is of importance here because thermally excited sound waves are one of the sources of the $\delta\epsilon$ mentioned above. In fact light scattering has made it possible to study the velocities and lifetimes of sound waves in liquids at frequencies up to about 7 GHz,^(4, 5) and a number of the liquids studied exhibited dispersion in this region.

In those cases for which the above considerations preclude the use of the thermodynamic approach, a phenomenological approach of the same general form has been used.⁽⁶⁾ In this method non-thermodynamic variables are introduced which can describe the scattering processes otherwise neglected. For example the anisotropy scattering is described in terms of the elements of a mechanical deformation tensor and mechanical-optical coupling constants. The phenomenological method treats media in which dispersion is present by maintaining the form of the relations derived using thermodynamics, however it replaces all the thermal constants appearing in these relations with frequency dependent parameters. This phenomenological method, although useful in a number of cases, is in part based on an extension of thermo-

dynamics into a frequency region in which local equilibrium is not established, and therefore it is not entirely satisfactory.

The procedure outlined above will not be carried out. Rather, the derivation of the scattered spectrum given here will deal only with microscopic variables. This approach is similar to that used by Van Hove⁽⁷⁾ to describe inelastic neutron scattering and was first applied to the scattering of light by Komarov and Fisher.⁽⁸⁾ The scattering medium considered here is a simple one and the relationship between the spectrum and the density correlation function obtained could also be derived by the "thermodynamic" procedure (after assumptions are made about the relation of the thermodynamic variables and coupling constants to the microscopic variables). It is felt, however, that the derivation in terms of microscopic variables leads to a better understanding of the way in which the physical processes involved determine the spectrum.

In figure 2.1 the shaded portion of the medium represents that volume, designated by V , which is both illuminated by the source and observed by the detector. Only particles in this region will contribute to the scattered electric field $\vec{E}(\vec{K}, t)$ at the detector.

The spectral power density for the electric field at the detector is defined as the Fourier transform of the time displaced correlation function of the field:⁽⁹⁾

$$S_E(\vec{K}, \omega) \equiv \int_{-\infty}^{\infty} d\tau e^{-i\omega\tau} \langle \vec{E}(\vec{K}, t) \cdot \vec{E}^*(\vec{K}, t + \tau) \rangle. \quad 2.7$$

The $\langle \rangle$ indicate an ensemble average over similarly prepared systems. The process giving rise to the scattered field is assumed to be stationary, so the ensemble average is independent of the initial time t . As the name implies, $S_E(\vec{K}, \omega) \Delta \omega$ is proportional to the amount of power in the scattered electric field between the frequency shifts $\omega/2\pi$ and $(\omega + \Delta \omega)/2\pi$. To calculate the constant of proportionality first note that the mean square field at the detector is given by the integral of S_E over all frequency shifts:

$$\int_{-\infty}^{\infty} d\omega S_E(\vec{K}, \omega) = 2\pi \langle |\vec{E}(\vec{K})|^2 \rangle . \quad 2.8$$

But the total power I in watts per unit area in a complex plane wave of the form $E = E_0 e^{i(\omega t - \vec{k} \cdot \vec{r})}$ is given by

$$I = \frac{c}{8\pi} \langle |\vec{E}|^2 \rangle . \quad 2.9$$

Therefore if $I(\vec{K}, \omega) \Delta \omega$ is used to denote the power per unit area in the direction indicated by \vec{K} and lying between ω and $\omega + \Delta \omega$, it follows that

$$I(\vec{K}, \omega) = \frac{c}{(4\pi)^2} S_E(\vec{K}, \omega) . \quad 2.10$$

Now the expression for $\vec{E}(\vec{K}, t)$ will be derived. Without loss of generality the lens and detector can be assumed to be immersed in the medium. Thus we avoid considering the boundary between the scattering medium and the laboratory. In practice the behavior of the

scattered light at that point is handled by geometrical optics. Let the mean or observed incident electric field in the medium $\vec{E}_0(\vec{r}, t)$ be a complex plane wave

$$\vec{E}_0(\vec{r}, t) = \vec{E}_0 \exp(i\omega_0 t - i\vec{k}_0 \cdot \vec{r}). \quad 2.11$$

The effective electric field $\vec{E}_E(\vec{r}, t)$, that which would be measured at the site of one of the particles of the medium, is linearly related to the mean incident field by a constant B:

$$\vec{E}_E(\vec{r}, t) = B \vec{E}_0(\vec{r}, t). \quad 2.12$$

This constant is determined by the dielectric susceptibility η of the medium:⁽¹⁰⁾

$$B = 1 + \frac{4\pi}{3} \eta. \quad 2.13$$

For light waves the relationship between η and the index of refraction n of the medium allows B to be expressed as

$$B = \frac{n^2 + 2}{3}. \quad 2.14$$

At distances which are large compared to the dimensions of the particle, the response of the particle to the effective field of the incident light can be viewed in terms of an induced dipole moment. This moment is linear in the effective field but may point in a different direction. Under these conditions one may express the dipole moment

of the m^{th} particle $\vec{P}_m(t)$ in terms of a time dependent polarizability tensor $\bar{\alpha}_m(t)$:

$$\vec{P}_m(t) = \bar{\alpha}_m(t) \cdot \vec{E}_E(\vec{r}_m, t). \quad 2.15$$

Here $\vec{r}_m(t)$ indicates the position of the m^{th} particle. All particles are assumed to be identical (not a necessary assumption, but a convenient one). However, the tensor differs from one particle to another since the particles' principal axes may make different angles with the reference coordinate system. The tensor is time dependent through the rotation or vibration of the particle. Equation 2.15 can break down in the case of solids, not because of the highly correlated motion of the constituent particles (which can be handled as a correlation among the various $\bar{\alpha}_m$), but because of the sharing of outer electrons. This sharing of electrons blurs the identity of the individual polarizable units implicit in equation 2.15. On the other hand, the majority of the electrons in most solids are tightly bound to the nuclei, forming units called cores in the theory of lattice vibrations. When the major portion of the polarizability of a solid comes from the cores (which do maintain their individuality and can be assigned an effective $\bar{\alpha}_m$), then calculations based on equation 2.15 should be in qualitative if not quantitative agreement with actual results. In fact an assumption of the form of equation 2.15 is used as basis of most quantum mechanical treatments of Raman scattering in solids. ⁽¹¹⁾

The dipole $\vec{P}_m(t)$ is time varying and will therefore radiate. Its contribution $\vec{E}_m(\vec{K}, t)$ to the electric field at the detector is given by

$$\vec{E}_m(\vec{K}, t) = \frac{1}{d_m c^2} \vec{l} \times \left(\vec{l} \times \dot{\vec{P}}_m(t') \right)_{t' = t_r} . \quad 2.16$$

Here \vec{l} is a unit vector in the direction of \vec{k}_s , t_r is the retarded time

$$t_r = t - d_m/c, \quad 2.17$$

and d_m is the optical path length from the m^{th} particle to the detector. To simplify equation 2.16 it should be noted that the time dependence of $\vec{P}_m(t)$ due to the particle rotation and vibration is very slow compared to that due to the $e^{i\omega_0 t}$ factor in the effective field, therefore only the latter need be included in the double time derivative and in the evaluation at the retarded time. Figure 2.2 shows the construction to be used to evaluate d_m . Let R be the optical path distance from the center of the coordinate system to the detector. Then d_m is given exactly by the relation

$$d_m = R - \frac{\vec{r}_m \cdot \vec{k}_s}{k_s} . \quad 2.18$$

Equation 2.16 can now be rewritten as

$$\begin{aligned} \vec{E}_m(\vec{K}, t) = & \frac{c}{R} \vec{k}_s \times (\vec{\alpha}_m(t) \cdot \vec{E}_0 \times \vec{k}_s) \\ & \exp(i\omega_0 t - ik_0 R) \exp(i\vec{K} \cdot \vec{r}_m(t)). \end{aligned} \quad 2.19$$

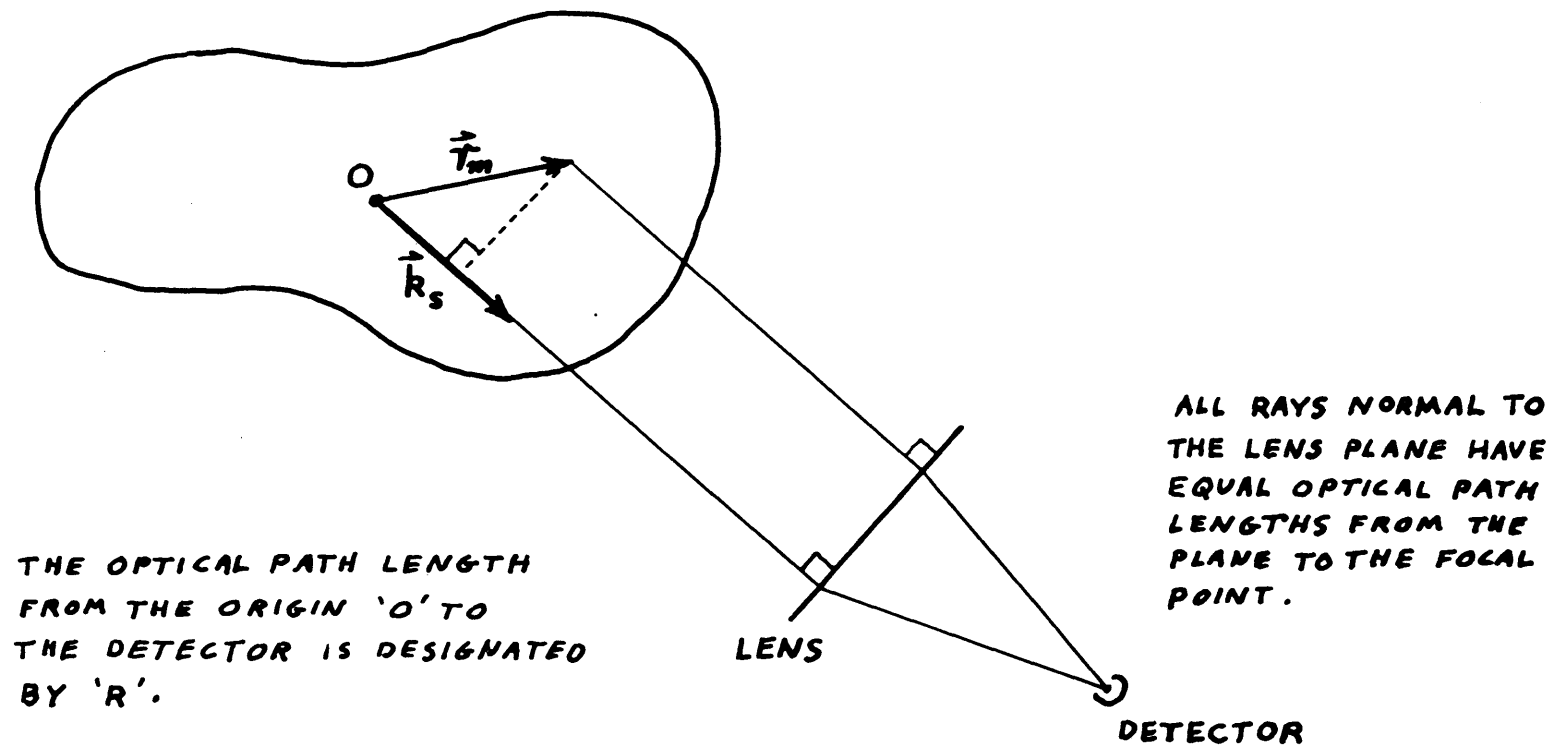


Fig. 2.2 Construction involved in the evaluation of the phases of the scattered waves.

The total field at the detector is then found by summing the contributions from each particle:

$$\vec{E}(\vec{K}, t) = \sum_m E_m(\vec{K}, t). \quad 2.20$$

Equation 2.19 is quite general and forms the basis for the classical explanation of a wide range of scattering phenomena. The tensor nature of $\bar{\alpha}_m$ gives rise to depolarization scattering, that is, components of $\vec{E}(\vec{K}, t)$ perpendicular to the electric field of the incident light. The time dependence of $\bar{\alpha}_m$ due to rotation or vibration of the particle gives the classical Raman effect. Raman scattering involves frequency shifts which are large compared to the quasi-elastically scattered light being investigated here. Therefore this part of the time dependence of $\bar{\alpha}_m$ can be dropped from consideration. This can be put another way. Since the experiments investigate a range of frequencies up to about 1 GHz, they obtain information about processes occurring over periods of time no shorter than about 10^{-9} seconds. In deriving the quasi-elastic spectrum, therefore, changes in the orientation or the structure of the particles occurring over times less than this may be 'averaged over' when calculating $\bar{\alpha}_m$. The rotation of the molecules in a gas is so rapid that the averaging process reduces $\bar{\alpha}_m$ to a time independent scalar polarizability α . In the case of liquids, however, the molecular rotation is hindered by neighboring molecules. In most liquids the rotational part of the spectrum (called anisotropy scattering or the wing of Rayleigh line) is still much broader than the quasi-elastic portion,⁽¹²⁾ but Starunov et. al.⁽¹³⁾ have found that in at

least one case, nitrobenzene, the two portions have a comparable extent. In general, though, the quasi-elastic scattering in liquids can also be represented by a scalar polarizability.

In terms of a constant scalar polarizability α , equation 2.20 can be written as

$$\vec{E}(\vec{K}, t) = \frac{\alpha B E_0 k_0^2 \sin \phi}{R} \exp(i \omega_0 t - i k_0 R) \quad 2.21$$

$$\times \sum_m \exp(i \vec{K} \cdot \vec{r}_m(t))$$

where ϕ is the angle between \vec{E}_0 and \vec{k}_s . It is convenient to define a particle density $\rho(\vec{r}, t)$ such that its integral over a region of space gives the number of particles in that region:

$$\rho(\vec{r}, t) = \sum_m \delta(\vec{r} - \vec{r}_m(t)). \quad 2.22$$

Here $\delta(\vec{r})$ is the Dirac delta function. The sum involved in equation 2.21 can be expressed simply in terms of the density:

$$\sum_m \exp(i \vec{K} \cdot \vec{r}_m(t)) = \int_V d\vec{r}^3 \rho(\vec{r}, t) \exp(i \vec{K} \cdot \vec{r}). \quad 2.23$$

Now S_E may be found by substituting equations 2.21 and 2.23 into 2.7:

$$S_E(\vec{K}, \omega) = \left(\frac{\alpha B E_0 k_0^2 \sin \phi}{R} \right)^2$$

$$\int_V \int_V \int_{-\infty}^{\infty} dr^3 dr'^3 d\tau \langle \rho(\vec{r}', t) \rho(\vec{r}' + \vec{r}, t + \tau) \rangle \exp(i\vec{K} \cdot \vec{r} - i\omega\tau). \quad 2.24$$

To simplify notation, define the density correlation function

$$G(\vec{r}, t) \text{ as} \quad 2.25$$

$$G(\vec{r}, t) \equiv \frac{1}{N} \int_V dr'^3 \langle \rho(\vec{r}', 0) \rho(\vec{r}' + \vec{r}, t) \rangle ;$$

and also define the spectral power density $S_\rho(\vec{K}, \omega)$ for the particle density as

$$S_\rho(\vec{K}, \omega) \equiv \int_V \int_{-\infty}^{\infty} dr^3 dt G(\vec{r}, t) \exp(i\vec{K} \cdot \vec{r} - i\omega t). \quad 2.26$$

The normalization is chosen so that $G(r, t)$ approaches the average density $\rho_0 = N/V$ for large r and T . $G(r, t)$ is the classical limit of Van Hove's correlation function.⁽⁷⁾ N is the total number of particles in the region V . The spectral power density function S_ρ used here differs, however, from Van Hove's spectral function; the latter is $N/2\pi$ times larger than S_ρ . When the medium is homogeneous in space, the expectation value inside the integral in equation 2.25 is independent of the starting point \vec{r}' . In this case the integration may be carried out and one

obtains

$$G(r, t) = \frac{1}{\rho_0} \langle \rho(0, 0) \rho(r, t) \rangle. \quad 2.27$$

Equation 2.24 can be expressed concisely in terms of S_ρ :

$$S_E(\vec{K}, \omega) = N \left(\frac{\alpha B E_0 k_0^2 \sin \phi}{R} \right)^2 S_\rho(\vec{K}, \omega). \quad 2.28$$

The most practical way to express the information contained in equation 2.28 is through an inelastic differential scattering cross section $\sigma(\vec{K}, \omega)$ for the medium. Let $\sigma(\vec{K}, \omega) L P \Delta \Omega \Delta \omega$ be the power in watts scattered into a solid angle $\Delta \Omega$ about the direction corresponding to \vec{K} within a range of frequency shifts $\Delta \omega/2\pi$ about $\omega/2\pi$ when a length L of the medium is crossed by a light beam of total power P watts. It should be noted that $\sigma(\vec{K}, \omega) \Delta \Omega \Delta \omega$ is then the probability per unit length that a given incident photon will be scattered from the beam into $\Delta \Omega$ and $\Delta \omega$. If the beam has a cross sectional area A then $P = (AcE_0^2)/(8\pi)$ and $AL = V$. Using these facts equation 2.28 may be used together with equation 2.10 to give the principal result of this section:

$$\sigma(\vec{K}, \omega) = \frac{\rho_0}{2\pi} (\alpha B k_0^2 \sin \phi)^2 S_\rho(\vec{K}, \omega). \quad 2.29$$

This shows that the cross section corresponding to \vec{K} and ω is simply a constant times the space-time Fourier transform (evaluated at \vec{K} and

ω) of the particle density correlation function. The constant has the k_0 and ϕ dependence characteristic of dipole scattering.

For the case of gases the constant multiplying S_ρ in equation 2.29 can be evaluated easily. The polarizability α for gases is known to be given quite accurately in terms of the index of refraction n and the mean particle density ρ_0 by the Lorentz-Lorenz formula⁽¹⁰⁾:

$$\alpha = \frac{3}{4\pi\rho_0} \frac{n^2 - 1}{n^2 + 2}. \quad 2.30$$

Using this expression for α and equation 2.14 for B , equation 2.29 becomes

$$\sigma(\vec{K}, \omega) = \frac{\rho_0}{2\pi} \left(\frac{n^2 - 1}{4\pi\rho_0} \right)^2 \left(k_0^2 \sin \phi \right)^2 S_\rho(\vec{K}, \omega). \quad 2.31$$

It is convenient to know the cross section for scattering into a direction corresponding to K regardless of frequency shift:

$$\sigma(\vec{K}) \equiv \int_{-\infty}^{\infty} d\omega \sigma(K, \omega). \quad 2.32$$

Carrying out this operation on equation 2.29 and using 2.26 one finds

$$\sigma(\vec{K}) = \rho_0 (dB k_0^2 \sin \phi)^2 \int_V d r^3 G(\vec{r}, 0) e^{i\vec{K} \cdot \vec{r}}. \quad 2.33$$

The instantaneous density correlation function $G(\vec{r}, 0)$ is a sum⁽⁷⁾ of

the self part $\delta(\vec{r})$ and the pair distribution function $g(\vec{r})$ which is of interest in X-ray scattering:

$$G(\vec{r}, 0) = \delta(\vec{r}) + g(\vec{r}). \quad 2.34$$

In the case of dilute gases for $\vec{K} \neq 0$, $g(\vec{r})$ contributes a negligible amount to the integral in equation 2.33 and it follows that

$$\begin{aligned} \sigma(K) &= \rho_0 \left(\frac{(n^2 - 1) k_0^2 \sin^2 \phi}{4\pi \rho_0} \right)^2 \\ &= \frac{3}{8\pi} \sigma_t \sin^2 \phi \end{aligned} \quad 2.35$$

where σ_t is the total scattering cross section. Using the fact that $n \approx 1$, the total cross section can be written as

$$\sigma_t = \frac{2}{3\pi} \frac{1}{\rho_0} (n - 1)^2 k_0^4. \quad 2.36$$

σ_t can be interpreted as the probability that a photon, while traversing one cm. of the medium, will be deflected from the beam. Table 2.1 gives the values of σ_t for a number of gases at standard temperature and pressure.

Before leaving this discussion of the spectrum of the scattered light one should observe that S_ρ is not exactly the Fourier transform of G . The spatial integration in equation 2.26 is carried out only over the region V , therefore S_ρ is determined not only by G , but also by the

Table 2.1

Index of refraction and scattering cross section
for selected gases

Gas	$(n - 1)^*$	σ_T
A	2.81×10^{-4}	6.06×10^{-8}
Kr	4.26	13.9
N ₂	2.96	6.72
Ne	.67	.35
O ₂	2.71	5.63
Xe	7.00	37.6
CO ₂	4.46	15.3
CH ₄	4.41	14.9
C ₂ H ₂	5.63	24.3

*International Critical Tables, Vol. VII (McGraw Hill, N. Y. 1930)
Values referred to STP and 6300 Å

extent of V . If every dimension of V is large compared to $1/K$, then S_ρ will approach the transform of G . In practice the smallest dimension of V is usually the cross section of the illuminating laser beam. If the power distribution across the beam is given by $p(r)$ such that

$$\int dA p(r) = P, \quad 2.37$$

then $p(r)$ can be placed inside the integral in equation 2.26 and the limits of integration extended to infinity. The dimension of V along the beam is assumed to be much larger than $1/K$ and will be neglected. To determine the transverse \vec{K} dependence of $S(\vec{K}, \omega)$ one now has an exact Fourier transform, but of the product of $p(r)$ and G instead of G alone. The form of S_ρ can be visualized when one recalls that the Fourier transform of a product of two functions is the convolution of the transforms of the individual functions. For example assume the beam travels along the z axis and has a Gaussian profile with a radius (at the $1/e$ point) of a :

$$p(r) = \frac{P}{a^2 \pi} \exp\left(-\frac{x^2 + y^2}{a^2}\right) \quad 2.38$$

The transform of $p(r)$, denoted by $p(K)$ is then given by

$$p(K) = P \exp\left(-\frac{a^2}{4} \{K_x^2 + K_y^2\}\right) \quad 2.39$$

a Gaussian in K with a radius (at the $1/e$ point) of $2/a$. Its effect on the scattering is shown in figure 2.3. In order to determine the S_ρ measured in the experiment one must convolve the true spatial Fourier transform of G with $p(K)$. This has the effect of smearing out the values of K_x and K_y examined by the detector. The spectra corresponding to a range of \vec{K} vector are superimposed. K_z is still exact but a range of K_x and K_y are accepted with a Gaussian distribution about the average.

In these experiments the beam radius is no smaller than 10^{-2} cm. This implies that K_x is known to $\pm 2 \times 10^2 \text{ cm}^{-1}$. The finite radius of the beam will have the largest percentage effect in the forward direction where K is smallest (and the uncertainty is mostly parallel to the direction of \vec{K}). At 10.6° , the smallest scattering angle used in these experiments, $K = 2 \times 10^4 \text{ cm}^{-1}$. The uncertainty in K will produce a distribution of Brillouin shifts ω_s for the sound wave contribution to the spectrum since $\omega_s = v_s K$ where v_s is the sound velocity:

$$\frac{\Delta \omega_s}{\omega_s} = \frac{\Delta K}{K} \sim 2 \times 10^{-2}. \quad 2.40$$

The $\omega_s/2\pi$ is of the order of 100 MHz at 10.6° for the gases and the spurious frequency broadening of about 2 MHz is well below the instrumental resolution of about 28 MHz and therefore is unimportant in these measurements.

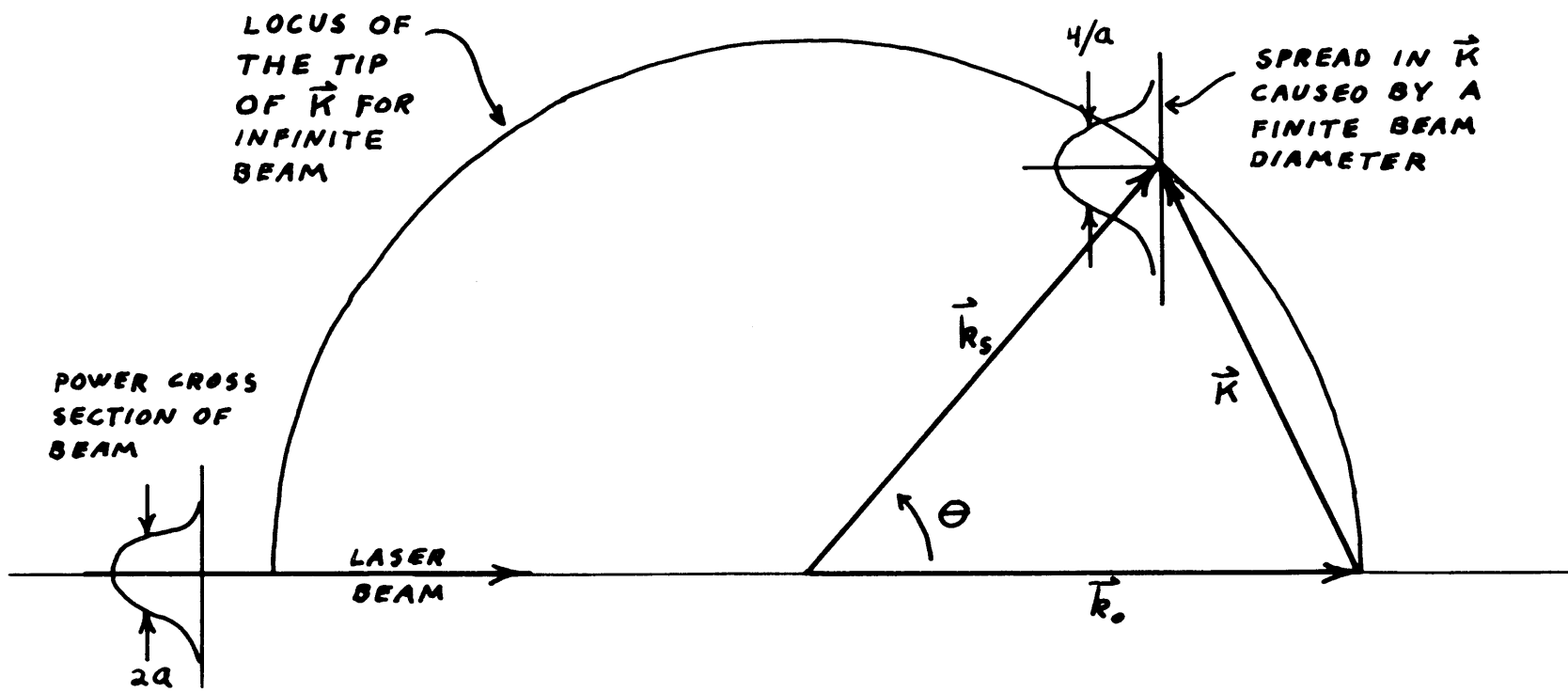


Fig. 2.3 Effect of a finite beam diameter on the determination of the scattering vector.

2. Connection between the Density Correlation Function, the Conditioned Density Distribution, and the Boltzmann Equation

In this section only homogeneous systems are considered (that is, crystalline solids are excluded), and $G(\vec{r}, t)$ can therefore be given by equation 2.27. In this case $G(r, t)$ is shown to be equal to the particle density distribution for times $t > 0$ when it is specified that at $t = 0$ there was a particle at $r = 0$. The spectrum of scattered light is then related to the evolution of an initial density disturbance in the medium. The equation of motion of such a disturbance is known only for dilute gases where it is related to the solution of the Boltzmann equation.

The correlation function for a homogeneous medium is

$$G(\vec{r}, t) = \frac{1}{\rho_0} \langle \rho(0, 0) \rho(r, t) \rangle. \quad 2.41$$

The physical meaning of $G(\vec{r}, t)$ can be visualized with the aid of figure 2.4. Consider an ensemble of M similarly prepared systems. In each system one notes the number of particles n_1 in a fixed increment of volume ΔV about $\vec{r} = 0$ at the time $t = 0$. At t seconds later one notes the number of particles n_2 in a region ΔV about the position \vec{r} . $G(\vec{r}, t)$ is then formed by averaging the product $n_1 n_2$ over all M systems:

$$G(r, t) = \frac{1}{\rho_0} \lim_{\substack{M \rightarrow \infty \\ \Delta V \rightarrow 0}} \frac{1}{M} \sum_{i=1}^M \left(\frac{n_1}{\Delta V} \right)_i \left(\frac{n_2}{\Delta V} \right)_i. \quad 2.42$$

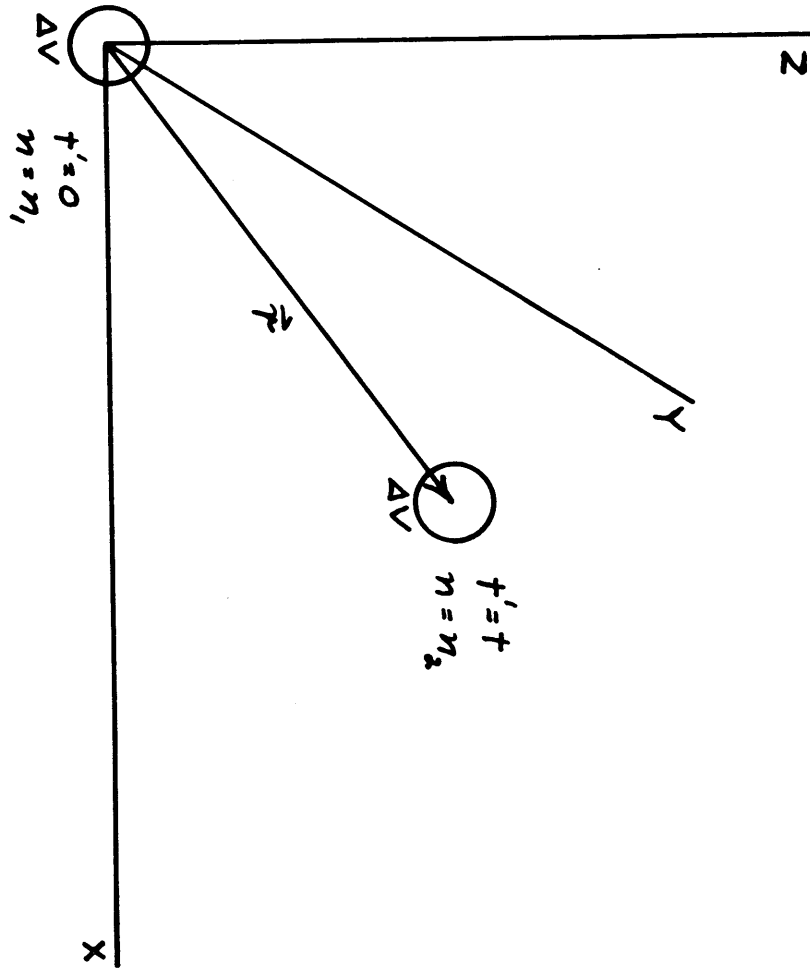


Fig. 2.4 Construction involved in the interpretation of $G(\vec{r}, t)$.

In the language of probability theory this expression can be written in terms of the joint probability $P(n_1, n_2)$ of finding n_1 particles at $(0, 0)$ followed by finding n_2 particles at (r, t) :

$$G(\vec{r}, t) = \frac{1}{\rho_0} \lim_{\Delta V \rightarrow 0} \left(\frac{1}{\Delta V} \right)^2 \sum_{n_1 n_2} n_1 n_2 P(n_1, n_2). \quad 2.43$$

Since one is required to let $\Delta V \rightarrow 0$, it is permissible to imagine a ΔV so small that the probability of finding two or more particles in ΔV is much smaller than the probability of finding only one particle. In this case the sum in equation 2.43 can be terminated at $n = 1$ with no loss of generality. Of the four remaining terms only one is non-zero and one has

$$G(\vec{r}, t) = \frac{1}{\rho_0} \lim_{\Delta V \rightarrow 0} \left(\frac{1}{\Delta V} \right)^2 P(n_1 = 1, n_2 = 1). \quad 2.44$$

Next one uses the fundamental law of conditional probability to express the probability $P(n_1 = 1, n_2 = 1)$ that $n_1 = 1$ and $n_2 = 1$ as a product of the probability $P(n_1 = 1)$ that $n_1 = 1$, times the conditional probability $P(n_2 = 1/n_1 = 1)$ that $n_2 = 1$ given that $n_1 = 1$. But $P(n_1 = 1)$ is just the average particle density ρ_0 times the volume element ΔV .

Similarly $P(n_2 = 1/n_1 = 1)$ is ΔV times the particle density distribution at \vec{r} and t given that there was a particle at the origin at the 0 of time, $P(\vec{r}, t / 0, 0)$. These facts allow equation 2.44 to be put in its final form:

$$G(\vec{r}, t) = \rho(\vec{r}, t / 0, 0). \quad 2.45$$

The conditional density distribution $\rho(\mathbf{r}, t/0, 0)$ can be defined for any system, regardless of its average density, and is of central importance in the theory of liquids and dense gases. The behavior of ρ , for distances large compared to the mean free path of a molecule in the medium and for times long compared to the mean time between collisions, can be determined from macroscopic equations of hydrodynamics or elasticity. However, at the present time a tractable microscopic equation of motion exists only for dilute gases.

For a dilute gas, the density of molecules $f(\vec{\mathbf{r}}, \vec{\mathbf{v}}, t)$ in a region about $\vec{\mathbf{r}}$ with velocities $\vec{\mathbf{v}}$ at a time t is given in terms of the collision cross section for the molecules by the Boltzmann equation⁽¹⁴⁾(BE),

$$\left(\frac{\partial}{\partial t} + \vec{\mathbf{v}} \cdot \nabla_{\mathbf{r}} + \frac{\vec{\mathbf{F}} \cdot \nabla_{\mathbf{v}}}{m} \right) f(\vec{\mathbf{r}}, \vec{\mathbf{v}}, t) = \left(\frac{\partial f}{\partial t} \right)_{\text{coll}}, \quad 2.46$$

and by the initial conditions. Here m is the mass of the molecule, $\vec{\mathbf{F}}$ is the external force acting on the molecules (henceforth assumed to be zero) and $\left(\frac{\partial f}{\partial t} \right)_{\text{coll}}$ is the collision term, a functional of f and the collision cross section. The validity of this equation is restricted to times long compared to the mean duration of a collision. The BE, as it is almost always treated, deals with point molecules interacting by way of a central potential. This precludes the discussion of the effects of internal degrees of freedom on the evolution of the distribution function. Therefore the results discussed here, which are based on equation 2.46, are limited to monatomic gases. A discussion of the

Boltzmann equation for polyatomic gases can be found in an article by Wang Chang, Uhlenbeck and DeBoer.⁽¹⁵⁾

The original derivation of the BE, and that given in most textbooks, is based on 'a priori' assumptions about the nature of the motion of the molecules (the assumption of molecular chaos or the collision number ansatz). Recent attempts⁽¹⁴⁾ to find an equation for f valid for higher densities lead to an exact expression relating f to the two-particle correlation function. This is the lowest equation of a hierarchy of N coupled equations, each relating the n -particle correlation function to an $(n + 1)$ - particle correlation function. The BE can be obtained from the equation for f on the basis of specific approximations. Under less severe approximations this approach could lead to an equation for f which is valid for dense gases.

The specification that a particle is located at the origin at $t = 0$ causes only a small deviation of f from its equilibrium value. Let f be made up of the sum of the equilibrium part $\rho_0 \phi(v)$ and a part $\phi(v)h(\vec{r}, \vec{v}, t)$ due to the perturbation:

$$f(\vec{r}, \vec{v}, t) = \phi(v) \left[\rho_0 + h(\vec{r}, \vec{v}, t) \right]. \quad 2.47$$

$\rho_0 \phi$ corresponds to the equilibrium distribution of N particles,

$$\phi(v) = \left(\pi v_0^2 \right)^{-3/2} \exp \left(- \frac{v^2}{v_0^2} \right) \quad 2.48$$

where v_0 is defined by the relation

$$v_0^2 = \frac{2k_B t}{m}. \quad 2.49$$

The equation of motion of h is obtained by substituting equation 2.47 into 2.46, and the resulting linearized BE is⁽¹⁴⁾

$$\left(\frac{\partial}{\partial t} + \vec{v} \cdot \nabla_{\vec{r}} \right) h = \int d v_1^3 \int d \Omega g \sigma(g, \theta) \times \rho_0 \phi(v_1) (h' + h_1' - h - h_1). \quad 2.50$$

Here the prime and index 1 refer to the velocity variables only, so that $h_1 \equiv h(\vec{r}, \vec{v}_1, t)$; and, the four velocity variables refer to the velocities of the binary collision in such a way that $(\vec{v}, \vec{v}_1) \rightarrow (\vec{v}', \vec{v}_1')$. Also $g \equiv |\vec{v} - \vec{v}_1|$ is the relative velocity which in a collision turns over the angle θ , and $\sigma(g, \theta)$ is the differential scattering cross section.

The particle density $\rho(\vec{r}, t)$ is found by integrating $f(\vec{r}, \vec{v}, t)$ over all velocities; the conditional density is therefore the integral over velocities of the f given in equation 2.47:

$$\begin{aligned} \rho(r, t / 0, 0) &= \int d v^3 \phi(v) \left[\rho_0 + h(\vec{r}, \vec{v}, t) \right] \\ &= \rho_0 + \int d v^3 \phi(v) h(\vec{r}, \vec{v}, t). \end{aligned} \quad 2.51$$

The constant term contributes only to scattering in the forward direction and can be shown to give rise to the index of refraction of the medium.⁽¹⁴⁾ Therefore for $\vec{K} \neq 0$, the spectrum of the scattered light is related to $h(\vec{r}, \vec{v}, t)$ by the relation

$$S_{\rho}(\vec{K}, \omega) = \int dr^3 dv^3 dt \phi(v) h(\vec{r}, \vec{v}, t) \quad 2.52$$

$$\times \exp(i\vec{K} \cdot \vec{r} - i\omega t)$$

Finally the initial value of h must be specified. Since $\rho(\vec{r}, t/0, 0) = \delta(\vec{r})$, it follows from equation 2.51 that $h(\vec{r}, \vec{v}, 0)$ must be some velocity function times $\delta(\vec{r})$. It is consistent to allow the particle at the origin at $t = 0$ to have a Maxwellian probability distribution in velocities, ϕ . Since ϕ is already present as a factor in equation 2.47, the initial value of h is given simply by

$$h(\vec{r}, \vec{v}, 0) = \delta(\vec{r}). \quad 2.53$$

It has been shown in this section that the density correlation function $G(\vec{r}, t)$ for homogeneous media can be equated to the conditional density distribution $\rho(\vec{r}, t/0, 0)$. The macroscopic or continuum behavior of ρ can be described by the linearized equations of elasticity or hydrodynamics. Such a description is adequate for treating the scattering of light from solids and liquids since the wavelength of light is much larger than the particle mean free path. However, in the case of gases at pressures of one atmosphere and lower, the mean free path is comparable to the wavelength of light. In this case a microscopic or kinetic equation must be used to compute ρ and thereby obtain the spectrum of the scattered light. For dilute gases this leads to a well-posed initial value problem concerning the linearized Boltzmann equation. Solutions of this problem are discussed in the next section.

C. Approximate Solutions of the Boltzmann Equation

1. Hydrodynamics

For times long compared to the mean free time of the molecules of a medium, and for instances large compared to their mean free path, the evolution of disturbances in the density $\rho(\mathbf{r})$, in the average velocity $\vec{u}(\mathbf{r})$, and in the temperature $T(\mathbf{r})$ of a medium are described by the equations of hydrodynamics. For monatomic gases these equations may be obtained from the appropriate limiting behavior of the Boltzmann equation.⁽¹⁷⁾ The spectra for monatomic gases derived from these equations should be accurate as long as the magnitude of the scattering vector \vec{K} is much less than the reciprocal of the mean free path, and the frequencies involved, $\omega/2\pi$, are much less than the mean collision frequency.

A more general form of these equations, applicable to dense monatomic and polyatomic gases and to liquids, can be derived from the conservation laws for the macroscopic density, momentum, and energy.⁽¹⁸⁾ This derivation is essentially a thermodynamic one, and it requires the existence of local thermodynamic equilibrium. For this reason the spectra obtained from these more general hydrodynamic equations are accurate only for frequencies at which this local equilibrium can be maintained. As pointed out in section B. 1, this will be the case up to those frequencies for which the thermal parameters of the medium begin to exhibit a frequency dependence. It should be pointed out that the thermal parameters may deviate from

their low frequency values at frequencies well below the mean collision frequency of the molecules. This point will be taken up again later in this section. First the spectrum of the scattered light will be found for low frequency fluctuations on the basis of the more general hydrodynamic equations.

The linearized hydrodynamic equations are:⁽¹⁹⁾ the continuity equation

$$\frac{\partial \rho_1}{\partial t} + \rho_0 \nabla \cdot \vec{u} = 0, \quad 2.54$$

the Navier-Stokes equation

$$\rho_0 \frac{\partial \vec{u}}{\partial t} + \frac{C^2}{\gamma} \nabla \rho_1 + \frac{C^2 \beta \rho_0}{\gamma} \nabla T_1 \quad 2.55$$

$$- \left(\frac{4}{3} \eta_S + \eta_B \right) \nabla \nabla \cdot \vec{u} = 0,$$

and the energy transport equation

$$\rho_0 c_V \frac{\partial T_1}{\partial t} - \frac{c_V(\gamma-1)}{\beta} \frac{\partial \rho_1}{\partial t} - \Lambda \nabla^2 T_1 = 0. \quad 2.56$$

Here ρ_1 is the deviation of the number density from its equilibrium value ρ_0 , T_1 is the deviation of the temperature from its equilibrium value T_0 , and \vec{u} is the average local velocity. Also γ is the ratio of the specific heat at constant pressure c_P to that at constant volume c_V , η_S and η_B are the shear and bulk viscosities, Λ is the thermal

conductivity, β is the thermal expansion coefficient, and C is the low frequency limit of the sound velocity. Mountain⁽¹⁸⁾ has solved these equations for the space-time transformed density and temperature

$$\rho_1(\mathbf{K}, s) = \int_V d\mathbf{r}^3 \int_0^\infty dt \rho_1(\mathbf{r}, t) \exp(-i\vec{\mathbf{K}} \cdot \vec{\mathbf{r}} - st) \quad 2.57$$

$$T_1(\mathbf{K}, s) = \int_V d\mathbf{r}^3 \int_0^\infty dt T_1(\mathbf{r}, t) \exp(-i\vec{\mathbf{K}} \cdot \vec{\mathbf{r}} - st)$$

in terms of the initial values

$$\rho_1(\mathbf{K}) = \int_V d\mathbf{r}^3 \rho_1(\mathbf{r}, 0) \exp(-i\vec{\mathbf{K}} \cdot \vec{\mathbf{r}}) \quad 2.58$$

$$T_1(\mathbf{K}) = \int_V d\mathbf{r}^3 T_1(\mathbf{r}, 0) \exp(-i\vec{\mathbf{K}} \cdot \vec{\mathbf{r}})$$

Notice that the time transform is a Laplace transform to facilitate the handling of the initial conditions. In the most general case $\rho_1(\mathbf{K}, s)$ depends on the initial temperature distribution $T_1(\mathbf{K})$ as well as the initial density distribution $\rho_1(\mathbf{K})$. Because ρ and T can be used as independent thermodynamic variables, their values at a certain instant of time can be specified independently. In particular, one can choose $T_1(\mathbf{K})$ independently of $\rho_1(\mathbf{K})$. For the calculation of the density response function, one may therefore use as $T_1(\mathbf{K})$ its ensemble average, which is simply zero.

Using the initial condition $T_1(\mathbf{K}) = 0$, Mountain shows that

$$\rho_1(K, s) = \rho_1(K) \frac{s^2 + (a+b)K^2 s^2 + abK^4 + C^2(1-1/\gamma)K^2}{s^2 + (a+b)K^2 s^2 + (C^2 K^2 + abK^4) s + aC^2 K^4 / \gamma} \quad 2.59$$

where

$$a \equiv \frac{\Lambda}{\rho_0 c_V} \quad 2.60$$

$$b \equiv \left(\frac{4}{3} \eta_s + \eta_B \right) / \rho_0.$$

In order to relate this solution to $S_\rho(K, \omega)$ first note that

$$G(\vec{r}, t) = \rho(\vec{r}, t/0, 0) = \rho_0 + \rho_1(\vec{r}, t), \quad 2.61$$

and

$$\rho_1(\vec{r}, 0) = \delta(\vec{r}). \quad 2.62$$

By substituting 2.62 into 2.58 one finds that

$$\rho_1(K) = 1. \quad 2.63$$

Then by comparing equation 2.57 for $\rho_1(K, s)$ with equation 2.26 for $S_\rho(K, \omega)$ one finds that for $K \neq 0$

$$\begin{aligned} S_\rho(K, \omega) &= 2 \operatorname{Re} \left[\rho_1(K, s = i\omega) \right] \\ &= 2 \frac{N_R(\omega)D_R(\omega) + N_I(\omega)D_I(\omega)}{D_R(\omega)^2 + D_I(\omega)^2} \end{aligned} \quad 2.64$$

where $N(\omega)$ and $D(\omega)$ are the numerator and denominator of expression 2.59 with $s = i\omega$ and the subscripts R and I refer to their real and imaginary parts.

Mountain shows that for long wave length fluctuations, that is for small K , equation 2.64 represents three Lorentzian lines. The diffusion mode gives rise to a line unshifted in frequency with a full width at half height $\delta\nu_D$ given by

$$\begin{aligned}\delta\nu_D &= \frac{K^2 a}{\gamma\pi} \\ &= \frac{K^2}{\pi} \frac{\Lambda}{\rho_0 c_P}\end{aligned}\tag{2.65}$$

The sound wave mode gives rise to two lines (the Brillouin components) corresponding to frequency shifts ν_B of

$$\nu_B = \pm \frac{C}{2\pi} K\tag{2.66}$$

and whose full widths at half height $\delta\nu_B$ are given by

$$\begin{aligned}\delta\nu_B &= \frac{K^2}{2\pi} (b + (1-1/\gamma) a) \\ &= \frac{K^2}{2\pi} \left(\frac{\frac{4}{3} \eta_s + \eta_B}{\rho_0} + (\gamma-1) \frac{\Lambda}{\rho_0 c_P} \right)\end{aligned}\tag{2.67}$$

The ratio of the area under the central line to that under both of the sound wave lines is known as the Landau-Placzek ratio and is given by

$$\frac{\text{POWER IN CENTRAL LINE}}{\text{POWER IN BRILLOUIN DOUBLET}} = \gamma - 1. \quad 2.68$$

The thermodynamic parameters which pertain to these calculations are assembled in table 2.2 for a number of gases. Table 2.3 lists the values of $\delta\nu_D$, ν_B , $\delta\nu_B$, and the Landau-Placzek ratio computed on the basis of these parameters.

When the central line and the Brillouin lines begin to overlap, the spectrum no longer has the simple form discussed above. In this case one can evaluate equation 2.64 numerically to obtain the spectrum. A computer program has been written which evaluates equation 2.64 as a function of ω for given values of the parameters K , a , b , C and γ . The results of this program are compared with the experimental spectra in Chapter IV.

The use of the hydrodynamic equations to describe the spectra of polyatomic gases is made suspect by the fact that all these gases exhibit relaxation phenomena⁽²⁰⁾ and an associated dispersion in the sound velocity at frequencies which are less than those characteristic of the spectra observed in these experiments. This implies that some of the degrees of freedom of the molecule are not in equilibrium with the fluctuations which are being observed. Therefore the thermal parameters listed in table 2.2 (which are static or low frequency values based on an equilibrium with all the degrees of freedom) will no longer be appropriate to the equation of motion for the fluctuations. Consequently, the spectra are no longer represented by the

Table 2.2

Thermodynamic parameters for selected gases*

	m^a physical AMU	ρ^a g cm^{-3}	Λ^b $\text{cal sec}^{-1} \text{cm}^{-1} \text{ } ^\circ\text{C}^{-1}$	$\mu^{c, a}$ $\text{g cm}^{-1} \text{sec}^{-1}$	C_P^b cal g^{-1}	γ^d
A	39.94	1.634×10^{-3}	42.36	226.4×10^{-6}	.124	1.666
Kr	83.80	3.429	22.71	253.2	.059	1.666
N ₂	28.02	1.145	62.13	178.0	.249	1.405
Ne	20.18	0.824	115.26	317.3	.246	1.666
O ₂	32.00	1.309	63.37	206.4	.219	1.396
Xe	131.30	5.401	13.4	231.0	.0379	1.666
CO ₂	44.01	1.811	39.40	148.9	.202	1.302
CH ₄	16.04	0.657	81.49	111.5	.532	1.310
C ₂ H ₂	26.04	1.075	50.37	95	.403	1.280

* All values have been corrected to 25°C and 760 mm Hg.

a. AIP Handbook, 2nd edition.

b. CRC Handbook, 47th edition.

c. J. Kestin and W. Leidenfrost, *Physica* 25, 1033 (1959).

d. S. Chapman and T. G. Cowling, The Mathematical Theory of Non-Uniform Gases, (Cambridge University Press, Cambridge, England, 1952)

Table 2.3
Parameters Determining the Hydrodynamic Spectra of Gases

Landau-Placzek Ratio	Central Line Width*			Brillouin Line Width*			
	$\frac{\delta\nu}{n^2 \sin^2 \theta/2}$	$\theta = 10.6^\circ$	$\theta = 22.7^\circ$	$\frac{\delta\nu}{n^2 \sin^2 \theta/2}$	$\theta = 10.6^\circ$	$\theta = 22.7^\circ$	
A	.666	2.62 GHz	22.2 MHz	101 MHz	2.03 GHz	17.2 MHz	78.5 MHz
Kr	.666	1.41	12.0	55	1.09	9.24	42.1
N ₂	.405	2.74	23.2	106	1.86	15.8	71.9
Ne	.666	7.14	60.5	276	5.55	4.71	21.5
O ₂	.396	2.77	23.5	107	1.87	15.9	72.3
Xe	.666	.822	6.97	32	.631	5.35	24.4
CO ₂	.302	1.36	11.5	53	.892	7.56	34.5
CH ₄	.310	2.92	24.8	113	1.87	15.9	72.3
C ₂ H ₂	.280	1.46	12.4	56	.943	8.00	36.4

*The full width of the Lorentz line at its half power point is given.

characteristics given in table 2.3 which are based on the low frequency thermal parameters.

Mountain⁽²¹⁾ has proposed that the spectrum in the presence of these relaxation phenomena can be described simply by replacing the bulk viscosity η_B in equation 2.55 by a frequency dependent value. One of the features of the resulting theory, the appearance of a second unshifted mode in media exhibiting relaxation (this behavior is also present in the theory of Rytov⁽⁶⁾), has been confirmed in liquid carbon tetrachloride by Gornall et. al.⁽²²⁾ and by unpublished work in this laboratory⁽²³⁾. Those spectra in gases which arise from hydrodynamic fluctuations (scattering toward the forward direction at one atmosphere and for larger angles at higher pressures) will be very sensitive to these relaxation effects. Since the relaxation processes in gases are better understood than those in liquids, and can in fact be explained from first principles, the light scattering experiments on polyatomic gases may serve as a more sensitive test of the theories relating to these phenomena than can be obtained from the scattering in liquids. In these first experiments, however, stray light and limited resolution obscure most of the effects that relaxation processes might cause on the spectrum. The velocities of sound measured from the Brillouin shift, however, correspond to the highest frequency sound wave velocity measurements made in gases, and will show a dispersion due to any relaxation phenomena of lower or comparable characteristic frequencies.

2. Maxwell Molecules

The term Maxwell molecules refers to a hypothetical model in which molecules repel each other at all separations by means of a mutual potential energy V_{12} of the form

$$V_{12} = \frac{a}{|r_1 - r_2|^4} \cdot \quad 2.69$$

This form of the potential is of interest because the associated molecular collision cross section which appears in the collision term of equation 2.50 is independent of the relative velocity of the molecules. This mathematical simplification allows the eigenfunctions and eigenvalues of the collision operator to be found explicitly,⁽²⁴⁾ and as a result the solutions of the linearized BE (equation 2.50) can be found to any desired degree of approximation. Ranganathan and Yip⁽²⁵⁾ have computed the spectrum of the light scattered from a Maxwell gas. A brief outline of their method is given next.

The collision term in the linearized BE is a linear operator $L(h)$ operating on the velocity variables of the function h .

$$L(h) = \rho_0 \int dv_1^3 \int d\Omega g I(g, \theta) \phi_1 (h' + h'_1 - h - h_1) \quad 2.70$$

Equation 2.50 may be written as

$$\left(\frac{\partial}{\partial t} + \vec{v} \cdot \nabla \right) h(\vec{r}, \vec{v}, t) = L(h) \quad 2.71$$

where the perturbation of the equilibrium distribution function is

$$f_1(\vec{r}, \vec{v}, t) = \phi(v) h(\vec{r}, \vec{v}, t). \quad 2.72$$

Here ϕ is a normalized Maxwellian distribution:

$$\phi(v) = (\pi v_0^2)^{-3/2} \exp(-v^2/v_0^2), \quad 2.73$$

$$v_0^2 = \frac{2k_B T}{m}.$$

The parameter v_0 used throughout this thesis is consistent with most of the literature, but it is $\sqrt{2}$ times larger than that employed in reference 25. Now define the inner product of two functions of the velocity, $p(\vec{v})$ and $q(\vec{v})$ for example, as

$$(p, q) = \int dv^3 \phi(v) p(v) q(v). \quad 2.74$$

Let the eigenfunctions of the collision operator L be denoted by $\psi_n(\vec{v})$. In general these eigenfunctions are labelled by more than one subscript; but for the sake of clarity, and without loss of generality, the multiple subscripts are contracted to a single one in this presentation.⁽²⁶⁾ By definition the ψ_n have the property that

$$L(\psi_n(\vec{v})) = \lambda_n \psi_n(\vec{v}), \quad 2.75$$

and they are normalized in the sense that

$$(\psi_n, \psi_m) = \delta_{nm}. \quad 2.76$$

For any potential, there are five eigenfunctions which can be found by inspection and have eigenvalues equal to zero. These correspond to the quantities which are conserved in a collision, the particle number, momentum, and kinetic energy: 1, $m\vec{v}$, and $\frac{1}{2}m\vec{v}^2$. For any of these quantities the term in parentheses in equation 2.70 for $L(h)$ vanishes identically. The proper combination and normalization of these five quantities must be chosen to agree with the orthonormality condition 2.76 and as a result one obtains

$$\begin{aligned}\psi_0 &= 1 \\ \psi_i &= \sqrt{2} \frac{v_i}{v_0} \quad i = 1, 2, 3 \\ \psi_4 &= \sqrt{\frac{2}{3}} \left(\frac{\vec{v}^2}{v_0^2} - \frac{3}{2} \right).\end{aligned}\tag{2.77}$$

It can be shown⁽¹⁴⁾ that all the other eigenfunctions must have negative eigenvalues. It is assumed that the ψ_n form a complete set.

The solutions of the linearized BE can now be expanded in terms of the eigenfunctions:

$$h(\vec{r}, \vec{v}, t) = \sum_{n=0}^{\infty} a_n(\vec{r}, t) \psi_n(\vec{v}),\tag{2.78}$$

$$a_n = (\psi_n, h)$$

The first of the expansion coefficients $a_0(r, t)$ is just the density

disturbance in the medium. To understand this, recall that the non-equilibrium part of the conditional density response $\Delta \rho$ is found from equation 2.51 to be

$$\begin{aligned}
 \Delta \rho(\mathbf{r}, t) &\equiv \rho(\mathbf{r}, t/0, 0) - \rho_0 \\
 &= \int d\mathbf{v}^3 \phi(\mathbf{v}) h(\mathbf{r}, \mathbf{v}, t) \\
 &= (\psi_0, h) \\
 &= a_0(\mathbf{r}, t).
 \end{aligned}
 \tag{2.79}$$

The substitution of the expansion 2.78 into the BE given in 2.71 will give the equations of motion for the $a_n(\mathbf{r}, t)$.

The spectrum of $h(\vec{\mathbf{r}}, \vec{\mathbf{v}}, t)$ is measured experimentally, thus it is advantageous to deal with the transform of the space-time solution h . Let $g(\vec{\mathbf{K}}, \vec{\mathbf{v}}, \omega)$ be the Fourier space and Laplace time (with s already set equal to $i\omega$ as in section C.1) transform of h :

$$\begin{aligned}
 g(\vec{\mathbf{K}}, \vec{\mathbf{v}}, \omega) &= \int_V d\mathbf{r}^3 \int_0^\infty dt h(\vec{\mathbf{r}}, \vec{\mathbf{v}}, t) \\
 &\quad \exp(i\vec{\mathbf{K}} \cdot \vec{\mathbf{r}} - i\omega t).
 \end{aligned}
 \tag{2.80}$$

Now g may be expanded in terms of the eigenfunctions of L :

$$\begin{aligned}
 g(\vec{\mathbf{K}}, \vec{\mathbf{v}}, \omega) &= \sum_{n=0}^{\infty} b_n(\vec{\mathbf{K}}, \omega) \psi_n(\vec{\mathbf{v}}) \\
 b_n &= (\psi_n, g).
 \end{aligned}
 \tag{2.81}$$

Again, it is the lowest expansion coefficient that pertains to the scattering of light. Starting with equation 2.64 one has

$$\begin{aligned}
 S_{\rho}(\vec{K}, \omega) &= 2 \operatorname{Re} \left[\Delta\rho(\vec{K}, \omega) \right] \\
 &= 2 \operatorname{Re} \left[\int dv^3 \phi(v) g(\vec{K}, \vec{v}, \omega) \right] \quad 2.82 \\
 &= 2 \operatorname{Re} \left[b_o(\vec{K}, \omega) \right].
 \end{aligned}$$

Therefore the spectral power density of the fluctuations in the number density is simply twice the real part of the lowest expansion coefficient.

The b_n are found by substituting the expansion 2.81 into the transformed BE together with the initial condition 2.53. The result, an infinite set of coupled algebraic equations for the b_n , is shown in equation 7 of the paper by Ranganathan and Yip.⁽²⁵⁾ This procedure is valid for any molecular potential, however, it can be carried out explicitly only for Maxwell molecules because the eigenfunctions of L and their inner products with the velocity (\vec{v}, ψ_n) are known only for the $1/r^4$ repulsive potential. The spectrum is found by truncating the infinite set of equations, leaving N equations for the first N expansion coefficients. Ranganathan and Yip have programmed a digital computer to solve the N algebraic equations for the coefficient $b_o(\omega)$ as a function of the parameter $y = |\lambda_{11}|/(Kv_o)$. λ_{11} is one of the Maxwell molecule eigenvalues and is dependent on the constant a in the molecular potential 2.69. Physically, y is proportional to the ratio of the wave length of the

fluctuations being observed λ_F (that is $\lambda_F = 2\pi/K$) to the mean free path L of molecules in the gas:

$$y = A \frac{\lambda_F}{L} . \quad 2.83$$

A is a dimensionless constant of the order of 0.1. To determine the value of y corresponding to a particular experiment one uses the relations between y and the viscosity η or thermal conductivity Λ of the gas:⁽²⁷⁾

$$\eta = \frac{m \rho_0 v_0}{3 y K}$$

$$\Lambda = \frac{5}{4} \frac{k_B \rho_0 v_0}{y K} \quad 2.84$$

The Maxwell molecule calculation gives self consistent values for the transport coefficients since the Eucken factor,⁽²⁸⁾ $\Lambda/(\eta c_V)$, calculated from equation 2.84 gives the kinetic theory value for a monatomic gas of 5/2.

The solutions for $y \gg 1$ correspond to the hydrodynamic region where the medium exhibits the behavior characteristic of a continuum. For these values of y the Maxwell molecule spectra coincide with that discussed in section C.1 with the values of $\delta\nu_D$, ν_s , $\delta\nu_s$ and the Landau-Placzek ratio corresponding to a monatomic gas.

Physically one expects the spectra for $y \ll 1$ to be that characteristic of a Doppler shift from independent molecules moving with a Maxwell distribution of velocities. The spectrum would then be

Gaussian:

$$S_{\rho}(K, \omega) = 2\pi (\pi v_0^2 K^2)^{-\frac{1}{2}} \exp \left[-\frac{\omega^2}{(v_0 K)^2} \right]. \quad 2.85$$

Equation 2.85 can be derived directly on the basis of a Doppler shift from independent molecules. A more formal way of arriving at the spectrum involves observing that in the limit of freely propagating independent molecules the solution of the linearized Boltzmann equation will be

$$h(\vec{r}, \vec{v}, t) = \delta(\vec{r} - \vec{v}t). \quad 2.86$$

This relation can be inserted directly into equation 2.52 for $S(K, \omega)$, and by carrying out the indicated integrations over \vec{r} , \vec{v} , and t the result stated in 2.85 is obtained.

The expansion 2.81 converges slowly for small y . Ranganathan and Yip obtained $S(K, \omega)$ for y greater than or equal to 0.4, and at $y = 0.4$ it was found that the results converged with $N = 80$.

Dr. Ranganathan has given us a copy of his computer program which calculates $S(K, \omega)$ for Maxwell molecules. With this we are able to generate spectra to compare with the experimental results. Initially, Dr. Ranganathan was kind enough to supply us with the results of his own calculations to compare with our early data.

3. Kinetic Models

The Maxwell molecule calculations discussed above solve

the linearized Boltzmann equation exactly for a very specific force law. This force law is only an approximation to the actual force between molecules. It is chosen for its mathematical convenience and not for its similarity to forces based on physical interactions. An alternative approach to tractable calculations based on the BE involves replacing the collision term in the BE, $\frac{\partial f}{\partial t}|_{\text{coll}}$, with a term (called a kinetic model) which resembles it in some sense, yet allows the resulting 'model equation' to be solved. Such a kinetic model would have parameters which depend upon the exact nature of the force law. The same model applied to different force laws would yield different distribution functions, and therefore different spectra. The application of kinetic models to the problem of light scattering is discussed in this section.

Perhaps the simplest kinetic model is that used in the mean free path treatment of transport phenomena:

$$\frac{\partial f}{\partial t}|_{\text{coll}} = \frac{1}{\tau(\mathbf{v})} \left\{ f_0 - f(\vec{r}, \vec{v}, t) \right\}. \quad 2.87$$

Here f_0 is the equilibrium distribution and $\tau(\mathbf{v})$ is an effective mean free time which may depend on the velocity. In order to understand the physical basis for this model and its extension introduced later, it is convenient to express the exact collision term in the form⁽¹⁷⁾

$$\frac{\partial f}{\partial t}|_{\text{coll}} = \bar{R} - R \quad 2.88$$

where

$R \delta t dr^3 dv^3 =$ no. of collisions occurring during the time between t and $t + \delta t$ in which one of the molecules involved is in $dr^3 dv^3$ about (\vec{r}, \vec{v}) before the collision, and

$\bar{R} \delta t dr^3 dv^3 =$ no. of collisions occurring during the time between t and $t + \delta t$ in which one of the molecules is in $dr^3 dv^3$ about (\vec{r}, \vec{v}) after the collision.

The model in equation 2.87 corresponds to a loss rate R from (\vec{r}, \vec{v}) which is proportional to the instantaneous distribution function $f(\vec{r}, \vec{v}, t)$. The constant of proportionality, $1/\tau$, is the average collision frequency. The rate of gain \bar{R} of particles in the region (\vec{r}, \vec{v}) is proportional to the absolute equilibrium distribution function f_0 . Of course, in the general case the loss rate and the gain rate are coupled by the collision process. Therefore one may say that the model in equation 2.87 corresponds to collisions which immediately reduce each particle involved to a state characteristic of absolute equilibrium. It is easily shown⁽²⁹⁾ that the model collision term 2.87 will not conserve particle number, momentum, or energy on an instantaneous basis. For this reason the model is not satisfactory for the description of kinetic processes, although it can be used as a basis for a hydrodynamic description of transport phenomena.

Bhatnagar, Gross, and Krook⁽²⁹⁾ proposed a model which satisfies the conservation laws on an instantaneous basis. This model (referred to simply as the Krook model) can be written in the form

$$\frac{\partial f}{\partial t} \Big|_{\text{coll}} = \frac{\underline{n}}{\sigma} \left\{ f_{\text{local}} - f(\vec{r}, \vec{v}, t) \right\} \quad 2.89$$

$$f_{\text{local}} = \underline{n} \left(\frac{m}{2\pi k_B \underline{T}} \right)^{3/2} \exp \left\{ -m(\vec{v} - \underline{\vec{q}})^2 / 2k_B \underline{T} \right\}.$$

Here $\underline{n}(r, t)$, $\underline{\vec{q}}(r, t)$, and $\underline{T}(r, t)$ are the local values of the density, flow velocity, and temperature defined as velocity averages over the distribution function:

$$\begin{aligned} \underline{n}(r, t) &= \int dv^3 f(r, v, t) \\ \underline{\vec{q}}(r, t) &= \underline{n}^{-1} \int dv^3 \vec{v} f(r, v, t) \\ \underline{T}(r, t) &= \frac{m}{3k_B \underline{n}} \int dv^3 (\vec{v} - \underline{\vec{q}})^2 f(r, v, t). \end{aligned} \quad 2.90$$

A comparison of equation 2.89 with 2.88 shows that the loss rate R is still proportional to the instantaneous distribution function. The constant of proportionality \underline{n}/σ can be interpreted as collision frequency which depends on the local value of the density. The gain rate \bar{R} is proportional to the local equilibrium distribution function f_{local} , where f_{local} is a Maxwell-Boltzmann distribution based on the local instantaneous values of the density, flow velocity, and temperature. A collision, then, adjusts the particles involved to a local equilibrium. The Krook model can be shown to maintain the collision invariants of particle number n , momentum $m\vec{v}$, and kinetic energy $\frac{1}{2} m\vec{v}^2$.

The linearized form of the Krook equation for a uniform gas with

no external forces is given by⁽³⁰⁾

$$\left[\frac{\partial}{\partial t} + \vec{v} \cdot \nabla \right] h = \alpha \left[Z + \frac{2\vec{v} \cdot \vec{Q}}{v_0^2} + \left(\frac{v^2}{v_0^2} - \frac{3}{2} \right) \frac{\tau}{T_0} \right] - \alpha h, \quad 2.91$$

where

$$\begin{bmatrix} Z(r, t) \\ Q_i(r, t) \\ \tau(r, t) \end{bmatrix} = \int dv^3 \phi(v) h(r, v, t) \begin{bmatrix} 1 \\ v_i \\ T_0 \left(\frac{v^2}{3v_0^2} - 1 \right) \end{bmatrix}. \quad 2.92$$

ϕ and v_0 are given in equation 2.73. Equations 2.91 and 2.92 can be obtained by substituting into equations 2.89 and 2.90 the relations $\underline{n} = \rho_0 + Z(r, t)$, $\underline{q} = \vec{Q}(r, t)$, and $T = T_0 + \tau(r, t)$. Z , \vec{Q} , and τ are the deviations of the local density, velocity, and temperature from their equilibrium values. α is the adjustable parameter in this model and is interpreted as a collision frequency. The initial value problem (as discussed in section B.2) corresponding to equation 2.91 has been solved in terms of the transformed variables by Yip and Nelkin.⁽³⁰⁾ This involves a set of 6 simultaneous equations (corresponding to equations 2.91 and 2.92) in the transforms of h , Z , \vec{Q} , and τ . The result for $S_\rho(K, \omega)$, proportional to the real part of the transform of Z , is given explicitly as a complicated algebraic expression by Yip and Nelkin. The frequency dependence of S_ρ depends only on the parameter y given by

$$y = \frac{\alpha}{Kv_0}. \quad 2.93$$

This y has the same physical significance in the Krook model as it does in the case of Maxwell molecules. The equations for the transport coefficients in terms of y which pertain to the Krook model are⁽³⁰⁾

$$\eta = \frac{m\rho_0 v_0}{2yK} \quad 2.94$$

$$\Lambda = \frac{5}{4} \frac{k_B \rho_0 v_0}{yK}.$$

The Eucken factor calculated for the Krook model from equation 2.94 is $5/3$ which is inconsistent with the kinetic theory value of $5/2$. This means that in the hydrodynamic limit (large y) the value of y may be chosen to give either the proper central line width or the proper Brillouin line width, but the Krook model spectrum cannot fit both relaxation times simultaneously. Otherwise, the spectrum for large y is at least in qualitative agreement with the proper hydrodynamic spectrum for a monatomic gas in that it gives the correct Brillouin shift and a Landau-Placzek ratio of ~ 0.69 ($\gamma - 1$ is $2/3$ for a monatomic gas). In the limit of $y \ll 1$ the Krook spectrum reduces to the proper collisionless limit given in equation 2.85. The expression for $S_\rho(K, \omega)$ derived by Yip and Nelkin has been programmed on a digital computer and the Krook spectrum will be compared with the experimental data in Chapter IV.

More elaborate kinetic models have been proposed⁽³¹⁾⁽³²⁾ than the two considered here. In general they contain a larger number of adjustable parameters. It may be possible to see how well these models

represent the BE by adjusting the parameters to correspond to Maxwell molecules and comparing the results with the exact Maxwell molecule calculation. This was done for several models, including the Krook model, by Ranganathan and Yip.⁽²⁵⁾ In those models for which this test leads to a good agreement, the parameters can be changed to represent other molecular force laws. A comparison of the resulting spectra with the light scattering experiments in the region $y \sim 1$ would then be a means of choosing between various force laws.

References for Chapter II

1. For a discussion of the thermodynamic derivation and interpretation of spectra in liquids see I. L. Fabelinskii, *Usp. Fiz. Nauk* 63, 355 (1957) [Translation: *Soviet Physics Usp.* 63, 474 (1957)].
2. L. Landau and E. Lifshitz, *Statistical Physics*, Chapter 12 (Addison-Wesley, Reading, Mass., 1958).
3. K. F. Herzfeld and T. A. Litovitz: *Absorption and Dispersion of Ultrasonic Waves* (Academic Press, Inc., New York 1959).
4. G. Benedek and T. Greytak, *Proc. IEEE*, 53, 1623 (1965).
5. P. A. Fleury and R. Y. Chiao, *JASA* 39, 751 (1966).
6. A thorough treatment of this phenomenological approach to light scattering is given by S. M. Vytun, *J. Exptl. Theoret. Phys.* (U.S.S.R.) 33, 514-524 (1957) [Translation: *Soviet Physics JETP* 6, 401 (1958)]
7. L. Van Hove, *Phys. Rev.* 95, 249 (1954).
8. L. I. Komarov and J. Z. Fisher, *J. Exptl. Theoret. Phys.* (U.S.S.R.) 43, 1927 (1962) [Translation: *Soviet Physics JETP* 16, 1358 (1963)]
9. W. B. Davenport and W. Root, *An Introduction to the Theory of Random Signals and Noise* (McGraw-Hill, Inc., New York, 1958).
10. M. Born and E. Wolf, *Principles of Optics*, section 2.3 (Macmillan Co., New York 1964).
11. M. Born and M. Blackburn, *Proc. Roy. Soc.*, 89A, 277 (1949).
12. V. S. Starunov, *Doklady Akademii Nauk* (U.S.S.R.) 153, 1055 (1963) [Translation: *Soviet Physics, Doklady* 8, 1206 (1964)].
13. V. S. Starunov, E. V. Tiganov, and I. L. Fabelinskii, *J. Exptl. Theoret. Phys. Letters* (U.S.S.R.) 4, 262 (1966) [Translation: *Soviet Physics, JETP Letters* 4, 176 (1966)].
14. G. E. Uhlenbeck and G. W. Ford, *Lectures in Statistical Mechanics* (American Mathematical Society, Providence, R. I., 1963).
15. C. S. Wang Chang, G. E. Uhlenbeck, and J. DeBoer, *The Heat Conductivity and Viscosity of Polyatomic Gases*, in Vol. II of *Studies in Statistical Mechanics*, DeBoer and Uhlenbeck editors, (Wiley, N. Y. 1964).

16. B. Rossi, Optics, section 8.9 (Addison-Wesley, Reading, Mass. 1957).
17. Kerson Huang, Statistical Mechanics, (Wiley, N. Y. 1963).
18. G. Benedek, Lecture Notes 'Thermal Fluctuations and the Scattering of Light,' Brandeis Summer Institute in Theoretical Physics (1966). To be published.
19. R. D. Mountain, *Rev. Mod. Phys.* 38, 205 (1966).
20. For a discussion of relaxation processes in gases, see the articles by H. J. Bauer and H. O. Kneser in Volume II - Part A of Physical Acoustics, edited by Warren P. Mason (Academic Press, N. Y. 1965).
21. R. D. Mountain, *Journal of Research of N. B. S.* 70A, 207 (1966).
22. W. S. Gornall, G. I. Stegeman, B. P. Stoicheff, R. H. Stolen, and V. Volterra, *Phys. Rev. Let.* 17, 297 (1966).
23. T. T. Saito, M. S. Thesis, MIT, 1966 (unpublished).
24. C. S. Wang Chang and G. E. Uhlenbeck, University of Michigan Engineering Research Institute Report, Project M999 (1952).
25. S. Ranganathan and S. Yip, *Phys. Fluids* 9, 372 (1966). The value of v_0 used in this reference is smaller by a factor of $\sqrt{2}$ than the value v_0 used throughout the present thesis.
26. The notation and derivation used here is patterned after that in L. Sirovich and J. K. Thurber, *JASA* 37, 329 (1965).
27. Sidney Yip, private communication; and reference 14, page 107.
28. S. Chapman and T. G. Cowling, The Mathematical Theory of Nonuniform Gases (Cambridge University Press, N. Y. 1953).
29. P. F. Bhatnagar, E. P. Gross, and M. Krook, *Phys. Rev.* 94, 511 (1954).
30. S. Yip and M. Nelkin, *Phys. Rev.* 135, A1241 (1964).
31. E. P. Gross and E. A. Jackson, *Phys. Fluids* 2, 432 (1959).
32. L. Sirovich, *Phys. Fluids* 5, 908 (1962).

Chapter III

Experimental Apparatus and Methods

A. Introduction

The experimental problem is to resolve the spectrum of the light scattered by a gas at well defined angles from the forward to the backward directions. The small frequency shifts involved, from about 100 MHz at 10^0 to 1000 MHz in the backward direction, necessitate the use of optical spectrometers with resolving powers ($\nu/\Delta\nu$) of about 2×10^7 . Here ν is the light frequency and $\Delta\nu$ is the instrumental width. The light source must be monochromatic to better than 10MHz so that its spectrum does not obscure details of the spectrum being studied. Finally, since the scattering cross section of the gas is very small, a low noise, high efficiency photon detection system must be used.

A description of the overall arrangement and operation of the experimental system is first given below. Subsequent sections discuss (in detail) the operation of the individual components. Figure 3.1 is a schematic representation of the system as arranged while scattering toward the forward direction. The beam from a single mode, frequency stabilized gas laser is focused to a thin line along the axis of the scattering cell. The light scattered at some specific forward angle leaves the cell through a conical lens⁽¹⁾ (a prism of revolution) by which it is made parallel to the axis. Light scattered at other angles and passing through the conical lens will either diverge

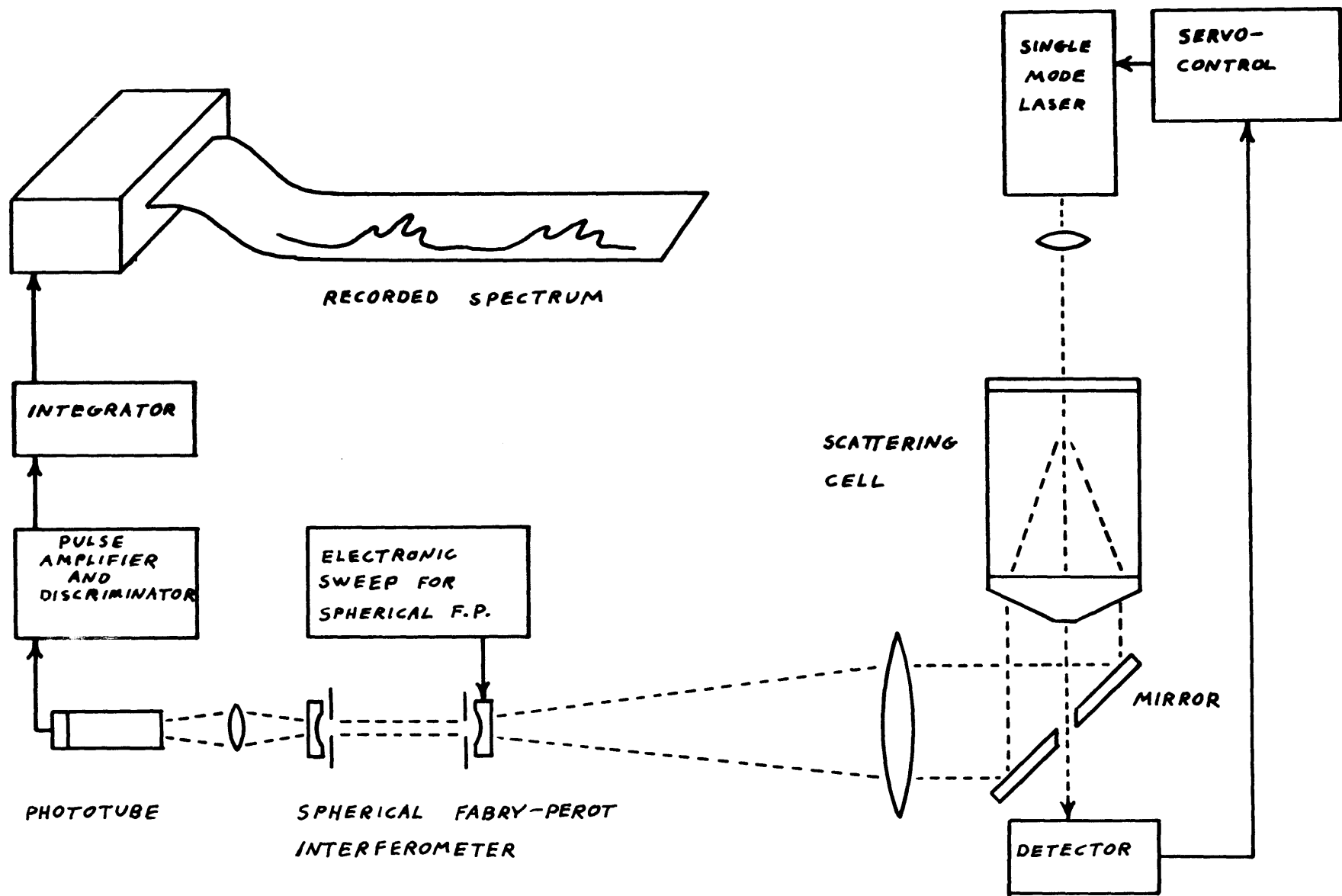


Fig. 3.1 Block diagram of experimental arrangement for forward scattering.

or converge relative to the axis. In front of the cell a mirror set at 45° to the axis deflects the scattered light into the spectrometer. The unscattered laser beam passes through a hole in the mirror and falls on a detector used in the stabilization of the laser. In the spectrometer the scattered light is passed through a spherical Fabry-Perot interferometer. The interferometer has a certain solid angle of acceptance and it is this which ultimately limits the range of scattering angles accepted on either side of the average scattering angle. The average scattering angle itself is determined by the geometry of the conical lens; therefore a different lens is employed for each angle.

The Fabry-Perot acts as an optical filter whose pass band is swept across the spectrum of the scattered light at a uniform rate. The light passing through the interferometer is focused on the photocathode of a photomultiplier tube. The photoelectron pulses arriving at the anode of the tube are processed by a pulse counting system and a signal proportional to the average photon counting rate is recorded. The recorded signal is the convolution of the instrumental profile (corresponding to the spectrum of the laser radiation and the interferometer band pass characteristic) with the spectrum imparted to the scattered light by the fluctuations in the gas.

In order to investigate the back scattered light the cell is turned around so that the conical lens faces the laser. The 45° mirror is then placed between the cell and the laser. A flat Fabry-Perot is used in the spectrometer to resolve the spectrum encountered in the backward direction.

The next four sections of this chapter describe in detail the laser, the scattering cell, the interferometers, and the photon detection system. The last section presents an expression for the sensitivity of the system.

B. The Laser

1. Description of the Laser

The laser used in these experiments is an experimental device on loan from the Bell Telephone Laboratories. The D. C. discharge tube is 17 cm. long with a 1.5 mm. bore and Brewster angle windows. The optical cavity is formed by two 10 meter radius of curvature mirrors separated by about 18 cm. One of the mirrors is mounted on a piezoelectric tube. The supporting frame and integral, adjustable mirror holders are made of invar. The laser delivers on the average 0.7 mW of power in a single longitudinal cavity mode at a vacuum wavelength of 6329.9 Å.

The separation $\Delta\nu_1$ between adjacent longitudinal modes is inversely proportional to the cavity length L,

$$\Delta\nu_1 \approx \frac{c}{2L}, \quad 3.1$$

where c is the velocity of light. Therefore lasers of this sort are purposely kept short, a fact which explains their proportionally low power output, in order to insure that only one mode at a time can oscillate under the gain curve of the Doppler broadened emission line. For example, expression 3.1 gives a value of about 830 MHz for the

longitudinal mode spacing. The 6329.9 \AA line is known to have a full width at half power of about 1500 MHz, but the range of possible laser action is usually limited to a region somewhat narrower than this near the peak of the line due to the losses in the cavity. In the laser used the active region is slightly wider than the mode spacing since, when two adjacent modes exactly straddle the center of the line, both modes can oscillate simultaneously.

The position of the cavity mode, and therefore the laser frequency, relative to the center of the gain curve of the gas is affected very strongly by thermal expansion of the cavity, pressure changes of the air between the Brewster angle windows and the mirrors, and by mechanical and acoustical vibration. The short term changes in frequency are minimized by several precautions. The laser is surrounded by a plexiglas box fitted to the outside of the invar framework in order to reduce pressure and temperature changes caused by air currents in the room. Before the laser is operated, the cavity is brought up to its known equilibrium temperature, about 65°C , by a heater inside the box. Experimental runs are made when the building is quiet (usually at night) and with the experimenter in the room only briefly from time to time to check the progress of the run. Even under these conditions it was found that reliable results could be obtained only if the frequency was stabilized by a servo-control system.

2. Details of the Servo-Control System

The servo-control system used here is based on the method employed in the single mode, stabilized laser built by Spectra-Physics

(their model 119). In fact, that commercial laser could have been used in these experiments except that its output power was only 1/5 of that from the Bell Labs unit. The method is based on the fact that the output power of a single mode laser exhibits a small dip, the "Lamb dip", ⁽²⁾ as the mode is tuned through the peak or center of the Doppler broadened emission line. The manner in which the Lamb dip is employed in the stabilization of the laser can be explained with the aid of figure 3.2, which shows the response of the cavity length, laser power, and laser frequency to the applied voltage on the piezoelectric element. The mirror displacement is linear in the voltage. The shift in the frequency $\delta\nu$ of a specific cavity mode is proportional to the mirror displacement δL :

$$\frac{\delta\nu}{\nu} = - \frac{\delta L}{L} \quad 3.2$$

A comparison of this equation with equation 3.1 shows that as the mirror separation is changed by one half wavelength, a cavity mode will move away from its initial frequency and be replaced by its neighboring mode. The figure shows this process taking place. At position 1 in the figure a mode is at the center of both the Doppler line and the Lamb dip: at position 2 it has moved out of the dip and is descending the side of the Doppler line: at 3 this mode ceases oscillation but its neighboring mode has begun to oscillate on the other side of the Doppler line: and finally at 4 the new mode has moved to the center of the Lamb dip.

Since the absolute frequency of the center of the Lamb dip is

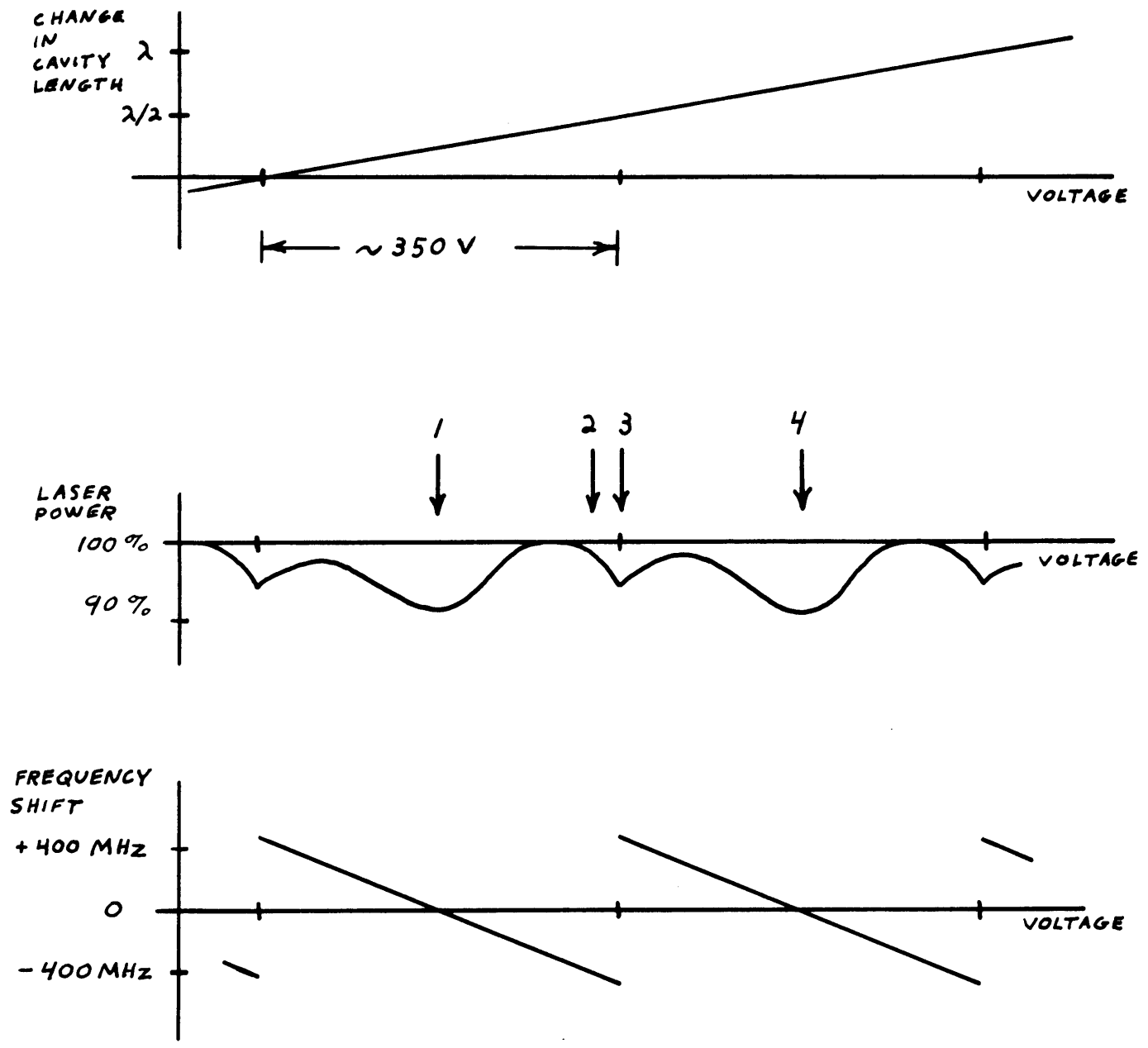


Fig. 3.2 Response of the laser to a change in the voltage on the piezoelectric element.

independent of external laboratory conditions it can be employed as a reference frequency. One must then lock the cavity mode to the bottom of the dip. Figure 3.3 shows a schematic representation of the servo system. The voltage which controls the minor position is made up of three components: a bias voltage manually adjustable from 150 to 600 V, an amplified error signal capable of producing ± 150 V, and a 2.4 V peak to peak reference signal at 1000 Hz. With the servo loop open the bias voltage is adjusted so that a cavity mode lies at the center of the Lamb dip. This mode is actually being swept back and forth about its equilibrium position by the 1000 Hz reference signal. The resulting frequency modulation of the laser is about ± 3 MHz. In this position there is effectively no amplitude modulation of the laser beam. If the cavity mode were to deviate a small amount from the center of the dip, the beam would be amplitude modulated at 1000 Hz by an amount proportional to the deviation and with a phase that differs by 180° on either side of the center. Amplitude modulation of the beam is detected by a solar cell placed in the beam, amplified, and fed into a lock-in amplifier (Princeton Applied Research model JB-4). The lock-in also serves as the source of the reference signal. In response to the detected modulation it produces a D. C. error voltage whose magnitude is proportional to the deviation from the center of the dip and whose sign depends on the sense of the deviation. The phase of the error signal relative to the reference signal is adjusted at the lock-in so that the amplified error signal will, when the servo loop is closed, push the cavity mode back toward the center.

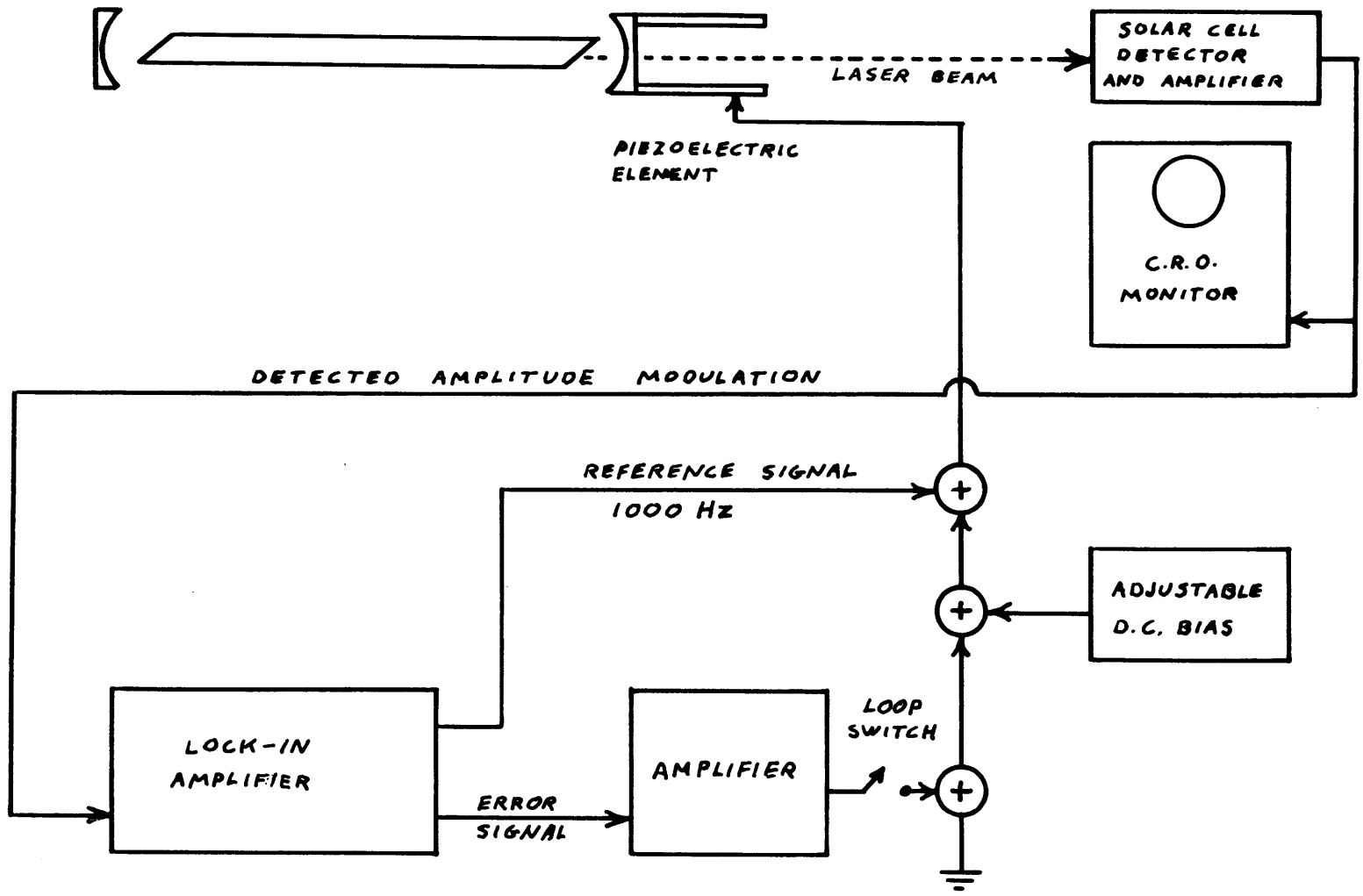


Fig. 3.3 Block diagram of the servo-control system.

Assume that with the loop open the cavity mode finds itself slightly displaced from the center of the dip. That displacement can be measured by the voltage change, ΔV , that the bias voltage would have to undergo to return the mode to the center of the dip. The open circuit amplified error voltage will have some value, V_E . Since V_E is proportional to ΔV one may define a dimensionless gain for the system, $G = V_E/\Delta V$. One can show that for $G \gg 1$ the closed loop frequency offset, $\Delta\nu_c$, is related to the open loop offset, $\Delta\nu_o$ by the relation $\Delta\nu_c = \Delta\nu_o/G$. In practice the gain is increased to a point just below the threshold for oscillation of the servo system and is generally of the order of 100 when the response time is .03 seconds. The amplified error signal can deliver at most ± 150 V, which from figure 3.2 is seen to correspond to ± 350 MHz. This means that the system will automatically compensate for open loop frequency drifts over a region of almost one cavity mode spacing. If the laser mode were to be in danger of exceeding this limit, the bias voltage could be manually adjusted to return the mode to the center of the dip. This procedure is seldom required in practice, however, and the laser has been left unattended for as long as eight hours. This implies that the laser frequency had drifted no farther from the center of the dip than 350 MHz divided by G , or about 3.5 MHz.

C. The Scattering Cell

Figure 3.4 is a full scale representation of the scattering cell as it is used when scattering toward the forward directions. The conical lens D and the reticle blank B form the front and back windows of the

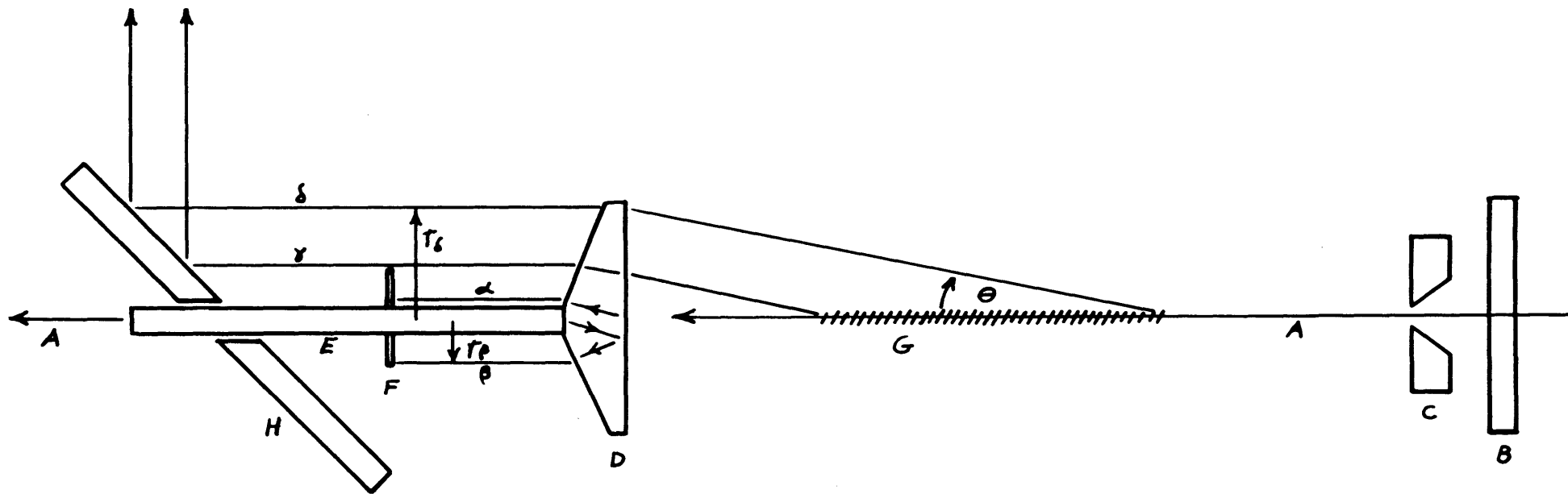


Fig. 3.4 Full scale drawing of the scattering cell.

cell whose body has been omitted for clarity. The laser beam A enters through the back window and passes along the axis of the cell. It leaves through the conical lens,⁽¹⁾ whose apex has been ground flat and parallel to its plane face. The beam emerging from the lens is surrounded by an opaque tube E which prevents light scattered by the air in front of the mirror, or by dust particles in the air, from reaching the spectrometer. A disk shaped aperture F is mounted on the tube to absorb certain rays scattered by the lens itself. In the figure only those scattered rays are traced which are made parallel to the axis by the lens. α indicates a ray originating from imperfections and dust at the point where the beam enters the lens. β indicates a ray back-scattered from the point where the beam (whose diameter is less than 1 mm) leaves the lens. This ray is reflected from the index of refraction mismatch between the lens and the gas in the cell and exits through the front of the cell. γ and δ are rays which delineate the region of rays due to the scattering from the gas alone. The hatch marked region G indicates the portion of the laser beam's path from which scattered light is accepted by the spectrometer.

In order to express the properties of the conical lens quantitatively it is convenient to introduce an intermediate angle ζ defined by the relation

$$n_L \sin \zeta = \cos \phi, \quad 3.3$$

where n_L is the index of refraction of the lens material and ϕ is the half apex angle of the cone. If the index of refraction of the medium in the cell is denoted by n_M , then the scattering angle θ is given by

$$\sin \theta = \frac{n_L}{n_M} \cos (\phi + \zeta). \quad 3.4$$

The radius r_β of the aperture necessary to block the spurious ray β is given by

$$r_\beta = 2T \frac{\tan \phi \cot (\phi + \zeta)}{\tan \phi + \cot (\phi + \zeta)} \quad 3.5$$

where T is the base to apex thickness of the lens.

The length L of the beam which is accepted by the spectrometer (the region marked G in figure 3.4) is given by

$$L = (r_\delta - r_\beta) \cot \theta \quad 3.6$$

where r_δ designates the maximum usable radius of the lens (corresponding to the ray marked δ in the figure). The spectrometer will accept not only those rays scattered at exactly θ , but also those within some range of angles $\Delta\theta_M$ about θ . Then for each point in the region G the conical light gathering geometry leads to an accepted solid angle of $\Omega = 2\pi \Delta\theta_M \sin \theta$. Therefore the product of scattering length and solid angle for this arrangement is

$$L \Omega = 2\pi (r_\delta - r_\beta) \Delta\theta_M \cos \theta. \quad 3.7$$

By passing through the lens the rays which form the increment of angle $\Delta\theta_M$ inside the cell are mapped into a slightly different increment $\Delta\theta_A$ in the air outside the cell. Their ratio is given by the expression

$$\frac{\Delta\theta_A}{\Delta\theta_M} = \frac{n_s \cos \zeta}{\sin(\phi + \zeta) \sin \phi} \sqrt{1 - \left(\frac{n_L}{n_M} \cos(\phi + \zeta)\right)^2} \quad 3.8$$

The parameters ϕ , θ , T , r_β and $\Delta\theta_A/\Delta\theta_M$ are given in table 3.1 for the two conical lenses used in these experiments. They are computed for an index of refraction of the scattering medium of 1.000, a value which applies to most gases at one atmosphere. The lenses were fabricated from Borosilicate Crown glass by the A. D. Jones Optical Company of Burlington, Massachusetts. The lenses have a radius of 1.91 cm but the cell in which they are mounted limits the effective radius r_δ to 1.27 cm. Lenses designed to give larger scattering angles would be inefficient since r_β rapidly approaches r_δ as θ is increased. For example the lens corresponding to $\theta = 22.7^\circ$ has $r_\beta/r_\delta = .61$. From figure 3.4 it can be seen that reversing the direction of the laser beam will present the spectrometer with light that has been scattered through an angle of $180 - \theta$. This adds the angles 169.4° and 157.3° to those that can be investigated with the two lenses.

The primary advantage of a conical light gathering geometry for scattering in an isotropic material (that is where the spectrum depends only on the magnitude of K and not its direction) is the precise definition of the scattering angle. In this experiment $\Delta\theta_M$ is always less than $1/2^\circ$. The more conventional method used to observe scattering⁽³⁾ employs a spherical lens positioned to one side of the beam with its focal point on the laser path. In this case the range of angles accepted $\Delta\theta_M$ is given by the ratio of the diameter of the lens to its focal length.

Table 3.1
Data for the Conical Lenses*

Quantity	Lens	
	70°	50°
ϕ	70°	50°
θ	10.6°	22.7°
T	.98 cm	1.75 cm
r_{β}	.23 cm	.77 cm
$\Delta \theta_A / \Delta \theta_M$	1.03	1.13

* Calculated on the basis of the indices of refraction $n_L = 1.515$
and $n_M = 1.000$ at 6329.9 Å.

In general, for a given value of $\Delta\theta_M$, the product of scattering length and solid angle (which determines the amount of scattered light detected) of the spherical lens system is much less than that given in equation 3.7 for the conical system.

It would be desirable to exploit the advantages of a conical geometry for scattering angles closer to 90° . The impracticality of conical lenses for scattering angles of more than 25° from the forward or backward direction led to the investigation of conical reflectors. The basic design is shown in figure 3.5. A conical reflector B is placed inside a cell with windows A and C. The body of the cell has been omitted for clarity. The laser beam D passes along the axis of the cone. If the half apex angle of the cone is ϕ , then a ray α scattered at an angle $\theta = 2\phi$ will leave the cell parallel to the axis. The only conceptual disadvantage to this rather simple arrangement is that some rays will emerge parallel which have been reflected more than once inside the cell. In the figure, β designates a ray of this type. They would correspond to scattering at angles other than 2ϕ . Reflectors with $\phi = 15^\circ, 25^\circ, 35^\circ$, and 45° were fashioned from Borosilicate Crown glass by the A. D. Jones Optical Company. The conical surface had a diameter of 3.81 cm at the base. The reflecting surface was coated with aluminum and an overlay of aluminum oxide. When used in experiments on the scattering of light from liquids,⁽⁴⁾⁽⁵⁾ the $15^\circ, 25^\circ$ and 35° reflectors gave detectable intensities simultaneously at as many as three scattering angles. This effect can be eliminated, however, by placing an opaque screen inside the cell which obscures 180° of the circumference of the reflector. The 45°

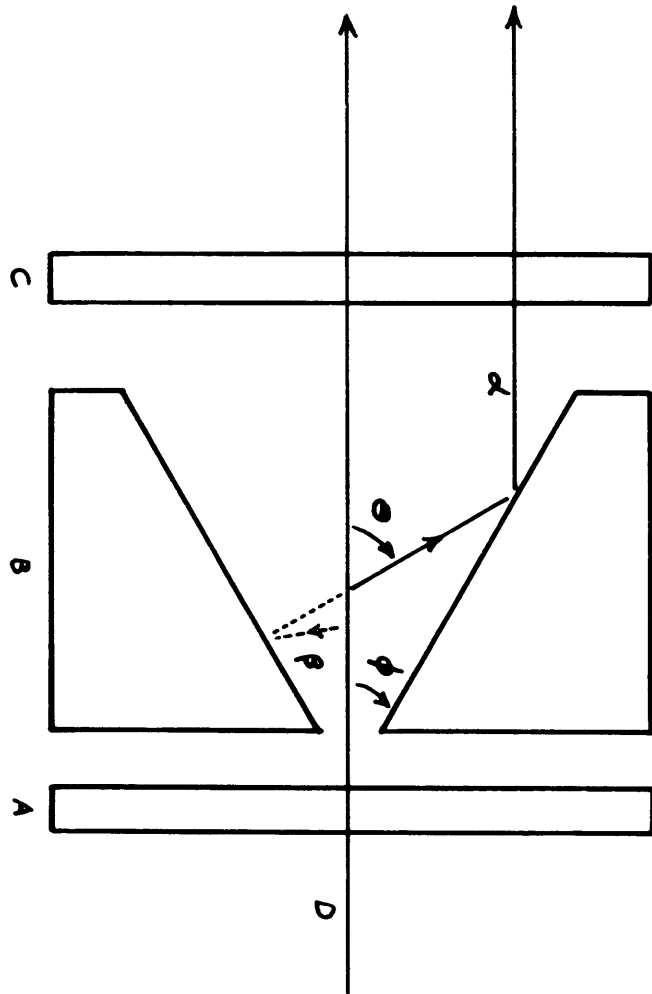


Fig. 3.5 A scattering cell using a conical reflector.

reflector will give rise to only 90° scattering and the opaque screen need not be employed.

During the experiments on liquids the relative performance of the lenses and reflectors was evaluated. The lenses seem to deviate from the idealized operation outlined above only by the partial reflection of the scattered ray as it passes through the front and back surfaces. The reflectors, on the other hand, never lived up to their theoretical performance, even when the partial absorption of the rays at the reflecting surface was taken into account. This is probably due to the poorer quality of their conical surfaces relative to those of the lenses. The concave conical surfaces of the reflectors showed visible tool marks and waves. The convex conical surfaces of all but the initial batches of lenses appear to be free of such technical flaws. The optical company admitted that the finishing of an inside conical surface is much more difficult than the finishing of an outside cone. As a result of this situation the reflectors were not employed in this work on the gases. It is believed, however, that conical reflectors will be of great value for studying scattering angles between 30° and 150° when the technical difficulties involved in their fabrication have been solved.

Tyndall scattering from dust particles suspended in the gas could obscure the scattering from the gas itself, but the problem is avoided in the following way. When the cell is evacuated the dust suspended in the air is either swept out with the gas or is deposited on the walls of the cell. The gas to be studied is admitted into the cell through a Millipore⁽⁶⁾ filter of 0.22 micron pore diameter and is therefore dust

free. Fortunately the dust which had remained in the cell adheres to the walls and, as long as the gas flow rate into the cell is not too high, it is not re-suspended in the gas. A small amount of as yet unexplained stray light does enter the spectrometer from the cell even when it is evacuated. This is elastically scattered light and contributes a small but significant amount to the experimental traces. This is measured by taking the spectrum of the evacuated cell after a run and it is later subtracted from the experimental results.

The pressure of the gas in the cell is measured to ± 1 mm. Hg by a mercury manometer. No attempt is made to control the temperature of the cell and the gas temperature is taken to be the ambient room temperature, which remains constant to $\pm 0.2^\circ\text{C}$ during a run.

D. The Fabry-Perot Interferometers

Two types of Fabry-Perot interferometers are used in this experiment: the conventional flat Fabry-Perot⁽⁷⁾ (FFP) and a newer spherical Fabry-Perot (SFP) first devised by P. Connes.⁽⁸⁾ The theory and operation of the SFP will be reviewed in detail here because of the novelty of the device. In order to relate the SFP to the better known FFP a short review of the properties of the latter will be given first.

1. The Flat Fabry-Perot

Consider the idealized FFP consisting of two rigorously flat lossless surfaces of reflectivity \mathcal{R} separated by a distance d and perfectly parallel to each other. The gas in which they are immersed has an index of refraction n . As shown in figure 3.6 a ray falling on

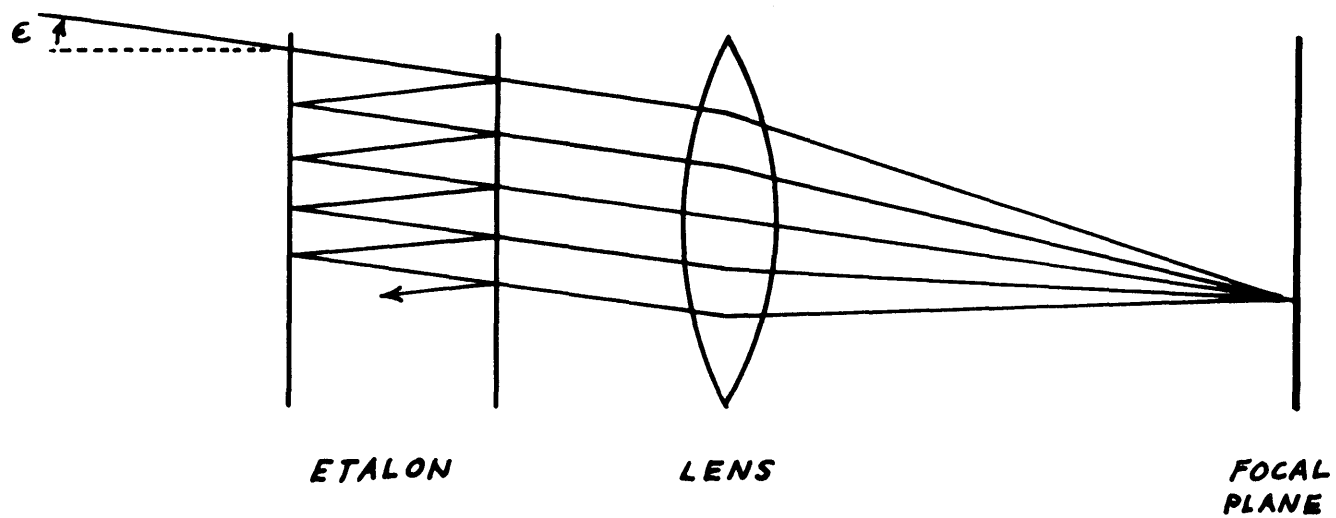


Fig. 3.6 Division and recombination of a ray in a flat Fabry-Perot.

the surfaces is divided into a number of parts and these parts, each differing in optical path length from next by some amount l , are recombined at a point in the focal plane of a lens. The ratio of the intensity I_L measured in the focal plane of the lens to the incident intensity I_I of the ray is given by

$$\frac{I_L}{I_I} = \left[1 + \frac{4 \mathcal{K}}{(1 - \mathcal{K})^2} \sin^2 \left(\frac{\pi l \nu}{c} \right) \right]^{-1} \quad 3.9$$

where ν is the light frequency.

For simplicity consider first only normally incident rays. For this case $l = 2nd$. Equation 3.9 has the form of a 'picket fence' in frequency and the distance between the pickets is defined to be the free spectral range f ,

$$f = \frac{c}{2nd} . \quad 3.10$$

The shape of each picket is referred to as the instrumental profile and for $\mathcal{K} > 85\%$ (a condition which is almost always met in practice) it is closely approximated by a Lorentz line shape with full width at half height of $\Delta\nu$. The ratio of f to $\Delta\nu$ is defined as the finesse F_R of the interferometer:

$$F_R = \frac{\pi \sqrt{\mathcal{K}}}{1 - \mathcal{K}} . \quad 3.11$$

The finesse and free spectral range are convenient parameters for the discussion of the FFP because they are functions of separate quantities.

f depends on the optical path variables n and d but is independent of the properties of the reflecting surfaces. The finesse as it has been used so far depends only on the reflectivity (hence the subscript R) but will later be generalized to include the effects of imperfect surfaces and a finite range of incident angles. Using these new variables equation 3.9 can be rewritten as

$$\frac{I_L}{I_I} = \left[1 + \left(\frac{2F_R}{\pi} \sin \frac{\pi \nu}{f} \right)^2 \right]^{-1} \quad 3.12$$

If n , the index of refraction, is now changed linearly with time by changing the pressure of the gas surrounding the mirrors, the picket pattern seems, to a high degree of approximation, to simply translate linearly past any fixed optical frequency. A change in n of $\lambda/2d$ (1.05×10^{-5} when $\lambda = 6330 \text{ \AA}$ and $d = 3 \text{ cm}$) causes one picket to be replaced by its neighbor, that is a particular instrumental profile translates by one free spectral range. For nitrogen gas at one atmosphere $n = 1.0003$ so a change in pressure of one atmosphere in a 3 cm etalon covers about 30 free spectral ranges. If the perpendicular incident ray has a spectrum of frequencies whose extent is less than f , then each time a picket sweeps across the spectrum the transmitted intensity undergoes a variation which is the convolution of the instrumental profile with that spectrum. This is the basic principle involved in the FFP spectrometer.

Thus far only normally incident rays have been considered, but it is clear that in order to detect an appreciable amount of light a

certain solid angle about the normal must be allowed. It must be determined, therefore, how large this solid angle can be made without smearing out the transmission characteristics outlined above. If a ray makes a small angle ϵ to the normal, its transmission is given by equation 3.9 with a value of l slightly smaller than that for the normal ray:

$$l \approx 2nd(1 - \epsilon^2/2). \quad 3.13$$

In particular the picket pattern has the same f and F_R as the one for normal rays; but, the absolute frequency of a particular picket is shifted relative to that for normal rays by an amount $\delta\nu$ given by

$$\frac{\delta\nu}{f} = -\frac{\delta l}{l} = -\frac{nd\epsilon^2}{l}. \quad 3.14$$

Clearly the maximum acceptance angle ϵ_M should be chosen in such a way that the $\delta\nu_M$ resulting from it is some fraction of the instrumental width caused by the reflectivity alone. In practice a convenient choice is $\delta\nu_M = \frac{1}{2} f/F_R$, or one half the reflectance limited instrumental width. With this choice

$$\epsilon_M = \left(\frac{f}{F_R \nu} \right)^{\frac{1}{2}} = \left(\frac{\Delta\nu}{\nu} \right)^{\frac{1}{2}}. \quad 3.15$$

The acceptance solid angle Ω is $\pi\epsilon_M^2$ and since $\nu/\Delta\nu$ is the resolving power of the instrument one has the useful relationship

$$\Omega \times \text{RESOLVING POWER} = \pi. \quad 3.16$$

The angles of acceptance are limited in practice by placing a pinhole whose radius is ϵ_M times the focal length in the focal plane of the lens following the interferometer. It can be shown that the instrumental profile of the spectrometer consisting of the ideal FFP, the lens, and the pinhole is nearly Lorentzian with a width 1.2 times the reflectance limited $\Delta\nu$. This then corresponds to an effective finesse F given by

$$F = F_R/1.2 . \quad 3.17$$

The factor which limits the resolution of most high finesse instruments is neither the reflectivity nor the finite acceptance angle, but defects in the surface flatness of the mirrors and their parallel alignment. The actual separation between the reflecting surfaces may deviate from the average value d from place to place over the useful area of the mirrors. The most common causes of this distribution of thicknesses are the following: improper alignment of the plates resulting in a residual wedge angle between the surfaces, bending of the mirrors caused by too large a pressure employed to hold or align the plates, curvature in the plates themselves, and rough surfaces caused by improper polishing or poor quality coatings. As a result of this variation there will be a finite width instrumental profile even in the limit of very large \mathcal{K} and very small ϵ_M . The shape of this profile will of course depend on the nature of the deviations but in general if the RMS average deviation over the illuminated area of the plates is some fraction $1/m$ of a wavelength of light then the defects limited finesse F_D is given roughly by⁽⁹⁾

$$F_D \sim m/2. \quad 3.18$$

When it is found experimentally that F_D is the major limitation on F , then the estimated value of F_D should be used in equation 3.15 to determine ϵ_M . A smaller value of ϵ_M would decrease the light gathering ability, but give no increase in resolution. More important is the fact that the instrumental profile is probably no longer Lorentzian, nor for that matter can it be expected to be any analytic shape. If the defects are mainly in alignment rather than surface quality, the shape and width may even change at each realignment of the instrument. For this reason each time a run is made in these experiments, an instrumental profile is measured for the system using elastically scattered laser light and it is later used when making a comparison between the theoretical spectra and the experimental ones. This will be discussed in detail in Chapter IV.

The FFP used in these experiments employs a pair of fused silica plates which are flat to $\lambda/100$ and coated to a reflectivity of 97% at 6328 \AA . The etalon for holding them was machined from solid invar and was copied from a design used by Dr. B. Stoicheff.⁽¹⁰⁾ The spacer is also made of invar and has a measured length of 1.1904 inches corresponding to a vacuum f of 4.96 GHz. The two plates taken together should have a surface figure of better than $\lambda/70$ corresponding to a $F_D \gtrsim 35$, neglecting any decrease due to misalignment. This is much smaller than F_R which is about 100. The system as a whole when carefully aligned gives a finesse of about 33, a satisfactory agreement with the considerations mentioned above.

The etalon is mounted in a vacuum tight enclosure and the value

of n is swept by evacuating the enclosure and letting dry nitrogen gas leak in through a limiting orifice.⁽¹¹⁾ As the pressure in the enclosure increases from zero to one atmosphere, about 30 pickets of the transmission function pass across a fixed optical frequency. The deviation of the sweep from linearity for the first ten free spectral ranges is experimentally negligible. The sweep rate is controlled by either switching orifices or by adding ballast volumes in series with the etalon enclosure.

2. The Spherical Fabry-Perot

The idealized SFP is formed by two concave spherical reflecting surfaces of equal radius of curvature placed so that the center of curvature of one is on the center of the surface of the other. This is a confocal geometry since the focal points of both mirrors coincide at the center of the cavity. Figure 3.7 shows such a cavity being traversed by a ray which is incident parallel to the axis and displaced from it by a distance r . Of course, this is not the most general ray that can pass through the cavity; but, because it can be drawn in two dimensions and its path is easily traced, it is a convenient ray to illustrate the physical principles involved in the SFP. The ray is divided into a number of parts, each differing by some optical length l from the next. These parts recombine as they leave the cavity (for example at A) rather than at the focal plane of a lens as in the FFP. Notice that portions of the ray under consideration also leave the cavity at B and that the resulting ray formed outside the cavity at B has the same transmission characteristic as the ray formed at A.

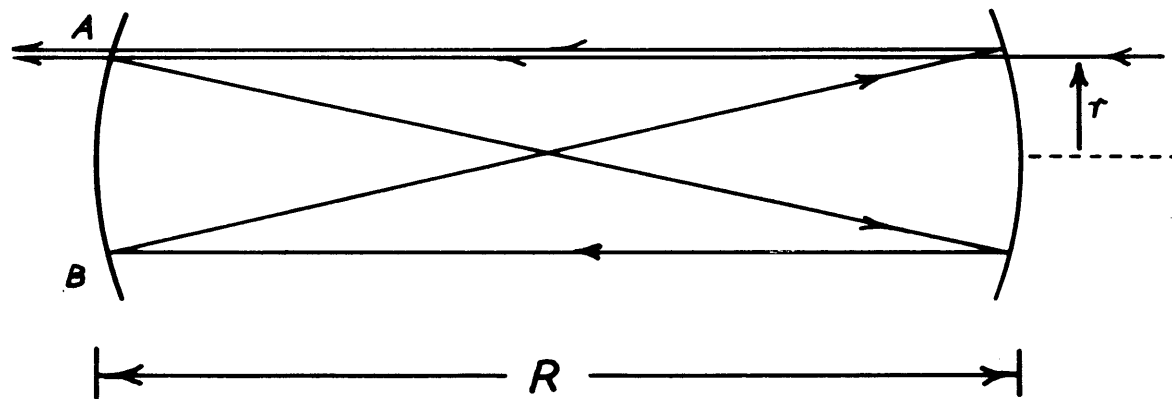


Fig. 3.7 Path of a particular ray in a spherical Fabry-Perot cavity.

In the more general case this leads to an intensity pattern at the exit mirror which is symmetric with respect to reflection through the center of the mirror surface.

The particular choice of incident ray used here allows the path in the cavity to be followed easily: the ray alternately travels parallel to the axis at a distance r from it and travels on a diagonal passing through the focal point. As was done in the case of the FFP, the transmission properties of a special ray will be discussed first. This reference ray is taken to be the ray shown in figure 3.7 in the limit $r \rightarrow 0$, and is called an 'on-axis ray'. For an on-axis ray $l = 4 n R$. By analogy with the interference phenomena in a FFP one may immediately draw two important conclusions. First, the free spectral range will be

$$f = \frac{c}{4 n R} , \quad 3.19$$

one half as large as that of a FFP of the same separation. This is because the path between interfering rays is twice as long. Second, the reflectivity finesse will be

$$F_R = \frac{1}{2} \frac{\pi \sqrt{\mathcal{R}}}{1 - \mathcal{R}} , \quad 3.20$$

one half as large as that of a FFP of the same reflectivity. This results because the distance l in the SFP involves twice as many reflections, and therefore twice the energy loss from the ray due to transmission, as does the path l in the FFP. As a result of these physical observations it follows that the intensity transmission

characteristic for the on axis ray looks identical to that of the FFP, but now depends on the new expressions for f and F_R given in equations 3.19 and 3.20.

Again the change in the transmission characteristic must be studied as the incident ray departs slightly from an on-axis ray. A more general ray is shown traversing the cavity in figure 3.8. Let \vec{r}_1 , be the position vector from the center of the surface of the first mirror to the point at which the incident ray first strikes it. Similarly let \vec{r}_2 completely specify the incoming ray. The angle between these two vectors is defined to be ψ_{12} . It is shown in Appendix A that the interference path length l for such a ray differs from the value for an on-axis ray by an amount Δl given by⁽⁸⁾

$$\frac{\Delta l}{R} = - \frac{r_1^2 r_2^2}{R^4} \cos 2\psi_{12} \quad 3.21$$

where R is the radius of curvature of the mirrors. In practice the rays accepted by the SFP are limited by a pair of identical apertures, each opaque except for a hole of radius a , placed in front of the mirrors and concentric with the axis. Therefore the magnitude of the vectors \vec{r}_1 and \vec{r}_2 must be less than a , and the maximum possible deviation in path length that any ray can have relative to an on-axis ray is a^4/R^3 . If the same criterion is used here that was used to choose the maximum Δl in the case of the FFP, that is

$$\delta l_M = \frac{\lambda}{f} \delta \nu_M = \frac{\lambda}{f} \left(\frac{1}{2} \frac{f}{F_R} \right), \quad 3.22$$

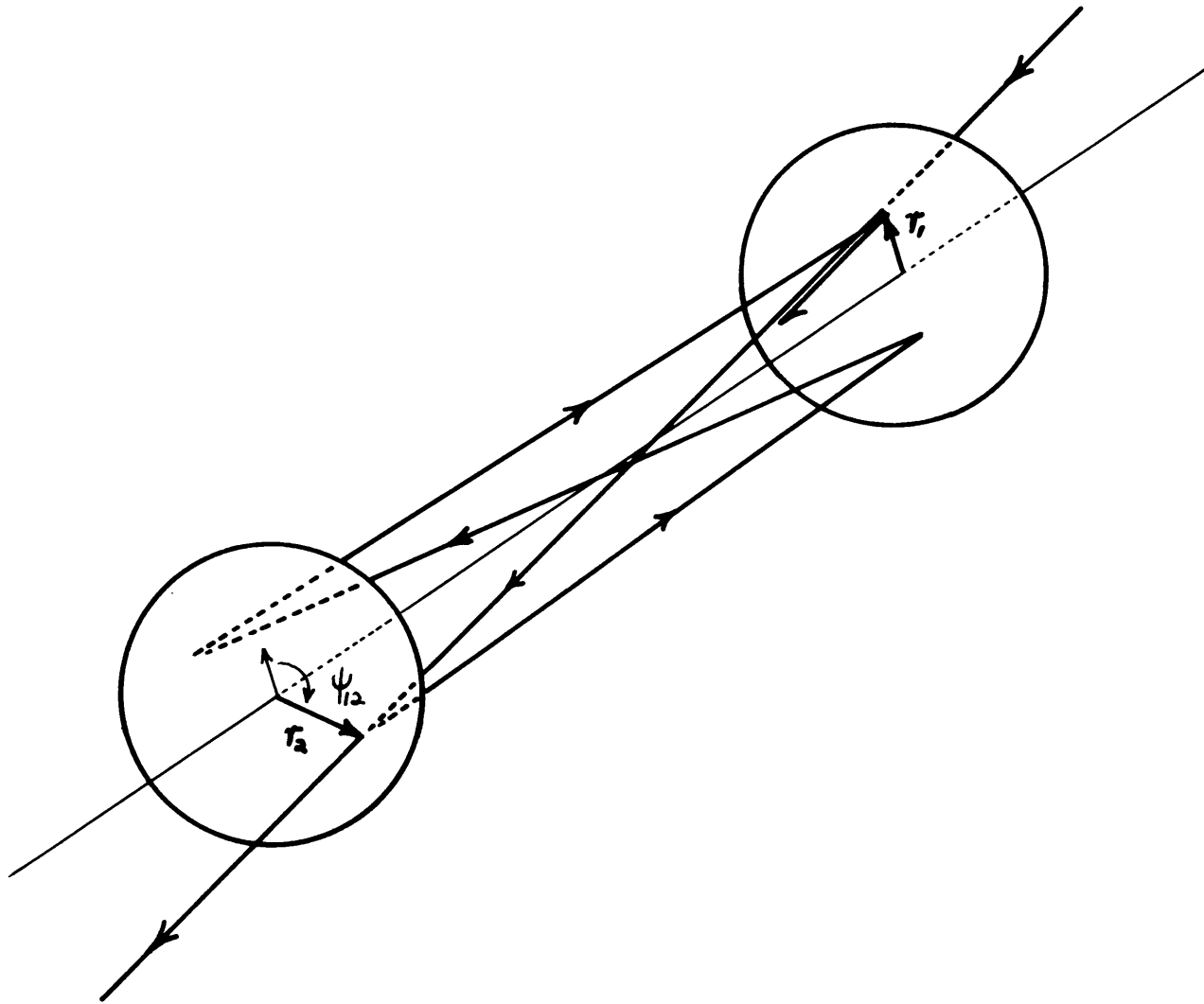


Fig. 3.8 Path of a general ray in a spherical Fabry-Perot cavity.

then the radius of the aperture is determined by the relation

$$\left(\frac{a}{R}\right)^4 = \frac{\lambda}{2RF} \cdot \quad 3.23$$

The limiting instrumental width, f/F_R , is the same for the SFP as it is for a FFP of the same spacing and reflectivity. The primary advantage of the SFP is that for large mirror separations, and consequently high resolution, its light gathering power exceeds that of the comparable FFP. The light gathering ability of an interferometer is proportional to the integral over the area of the aperture of the solid angle of acceptance. The French designate this quantity as the 'etendue' of the system. For the FFP the solid angle is the same at each point on the plates and equal to $\pi \epsilon_M^2$. If the usable area of the plates is denoted by A then the etendue E_F of the FFP is given by

$$E_F = \pi A \frac{\Delta\nu}{\nu} = \pi A \frac{f}{F\nu} \quad 3.24$$

and is inversely proportional to its resolving power. For the SFP the solid angle at any point on the input aperture is just the solid angle subtended by the other aperture, $\pi(a/R)^2$. Then the etendue E_S of the SFP by

$$E_S = \frac{\pi^2 a^4}{R^2} = \frac{\pi^2 \lambda R}{2F} \quad 3.25$$

Notice that, since the resolving power is proportional to R , if the resolution of a SFP is increased by increasing R , its light gathering

power will increase proportionally. This expression can be rewritten as

$$E_s = \pi (\pi R^2) \frac{f}{F\nu} . \quad 3.26$$

This form allows one to compare the light gathering abilities of spherical and flat interferometers. If both interferometers have the same f and F , that is have equivalent transmission characteristics, then a comparison of equations 3.26 and 3.24 shows that the ratio of the light gathering power of the SFP to that of the FFP is

$$\frac{E_s}{E_F} = \frac{\pi R^2}{A} . \quad 3.27$$

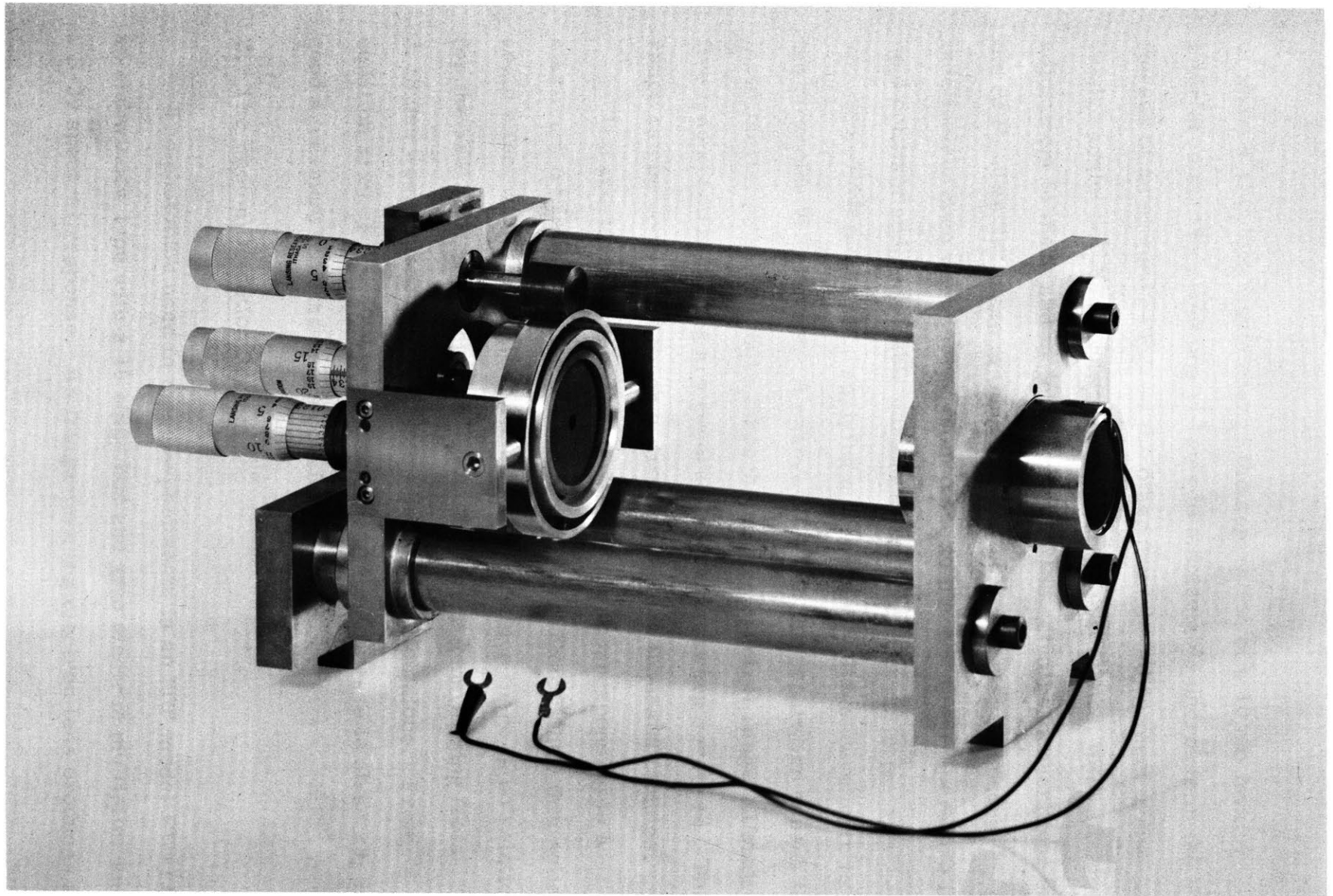
This is simply the square of the ratio of the separation of the SFP (or one half the separation of the equivalent FFP) to the usable radius of the FFP mirrors.

For example the etalons used for the FFP's in this laboratory allow a usable radius of 1.27 cm, and the SFP has a separation of 10 cm. Therefore equation 3.27 shows that this SFP has 62 times the light gathering power of an equivalent FFP. Moreover the equivalent FFP would have a separation of 20 cm and would be very difficult to align. The FFP used in this experiment has a separation of 3 cm. The SFP equivalent to it would have a radius of 1.5 cm and its light gathering power would only be 1.4 as great as the FFP. In practice mirrors of such small radius of curvature would be more difficult to fabricate to high tolerances than the 10 cm radius mirrors used here.

The SFP used in these experiments employs two 9.962 cm radius of curvature mirrors, whose radii are equal to $\lambda/75$ over a central aperture of 0.5 cm diameter and whose surfaces are spherical to $\lambda/75$ over the same central aperture.⁽¹²⁾ The mirrors are formed in fused silica blanks $3/8''$ thick and $1.5''$ in diameter. The reflecting surfaces are multi-layer dielectric coated to a reflectivity of 96% at 6328 \AA . The interferometer is shown in figure 3.9. Three invar rods are supported between two brass end plates. One mirror is attached to the larger end plate by a piezoelectric element. The other is in a gimbal mounting on a brass carriage which can be moved along the rods. Two differential micrometers adjust the two angular degrees of freedom of the gimbal mount and a third drives the carriage for fine adjustments about its proper location.

When the cavity, set up with a spacing other than R , is illuminated by diffused laser light interference rings are observed in the plane of the back mirror. Experimentally, the diameter of the central spot reaches a maximum when the cavity spacing approaches R . This fact is used to bring the SFP into rough alignment. By maximizing the central spot diameter the separation can be brought to within ten wavelengths of the optimum operating position. Final alignment of separation and mirror tilt is accomplished by driving the piezoelectric element by about $\lambda/4$ with an A. C. voltage and observing the instrumental profile on an oscilloscope. The maximum finesse occurs over a region of separations of about 2λ around R , but it is relatively insensitive to mirror tilt. As a consequence, a change in temperature

Fig. 3.9 The spherical Fabry-Perot mount.



of about 4°C (which would change the separation of a 10 cm invar interferometer by about one λ) leads to a detectable decrease in the finesse of an aligned SFP. On the other hand the adjustment of the 'wedge angle' between the two mirror surfaces (the most difficult adjustment to make and maintain in a FFP) is actually non-critical in the SFP. The SFP used in these experiments will stay aligned indefinitely even when moved from place to place if the temperature is held constant and reasonable care is exhibited.

The SFP is swept by applying a triangular voltage wave form to the piezoelectric element. A change of $\lambda/4$ in the separation causes the instrumental profile to move through one free spectral range. Usually five free spectral ranges are covered before the sweep reverses. This range can be covered in times of from one to one thousand minutes.

The aperture diameter used was 1.8 mm corresponding to a maximum Δl from equation 3.21 of about $\lambda/60$. Exactly how this solid angle effect will change the finesse is unclear since there is no relation for the SFP similar to equation 3.17. However, generalizing from 3.18 one would expect $F \sim 30$ from this contribution alone. From equation 3.20, $F_R \approx 40$. In practice the system finesse is about 28, in good agreement with the above considerations.

E. The Photon Detection System

The phototube used in these experiments is an ITT model FW-130, an end window type with a 16 stage box and grid electron multiplier and a S-20 spectral response. An image-forming electron lens produces an

image of the emitting photocathode in the plane of a small aperture immediately preceding the first dynode. A hole in the aperture limits the electrons entering the dynode chain to those coming from a $1/4''$ diameter spot on the photocathode. These features combine to reduce the number of dark pulses received at the anode to a very low rate without the necessity of cooling the phototube. The pulse height distribution of these dark pulses is shown by curve a in figure 3.10. This corresponds to a total tube voltage, kept constant in all these experiments, of 1700 V. Curve b in the figure shows the pulse height distribution resulting from a well illuminated photocathode, and can be assumed to be the distribution corresponding to those electrons which enter the dynode chain from the photocathode. A comparison of the two curves shows that a higher proportion of the dark pulses relative to signal pulses are concentrated at low pulse amplitudes. This is generally interpreted as indicating that most of the dark pulses begin to traverse the dynode chain beyond the photocathode, although the presence of thermal and field emission from the photocathode is indicated by the shape of the distribution for larger amplitude pulses.

The pulses from the anode are processed by a model PA-603 preamplifier, model 901-A linear amplifier, and a model 901-SCA single channel analyzer, all made by Cosmic Radiation Labs., Inc. The single channel analyzer is set to accept all pulses above the threshold height indicated in figure 3.10.⁽¹³⁾⁽¹⁴⁾ Comparing the area under curve b which falls above the threshold to the total area, one finds that only 12% of the signal counts are lost by this pulse height

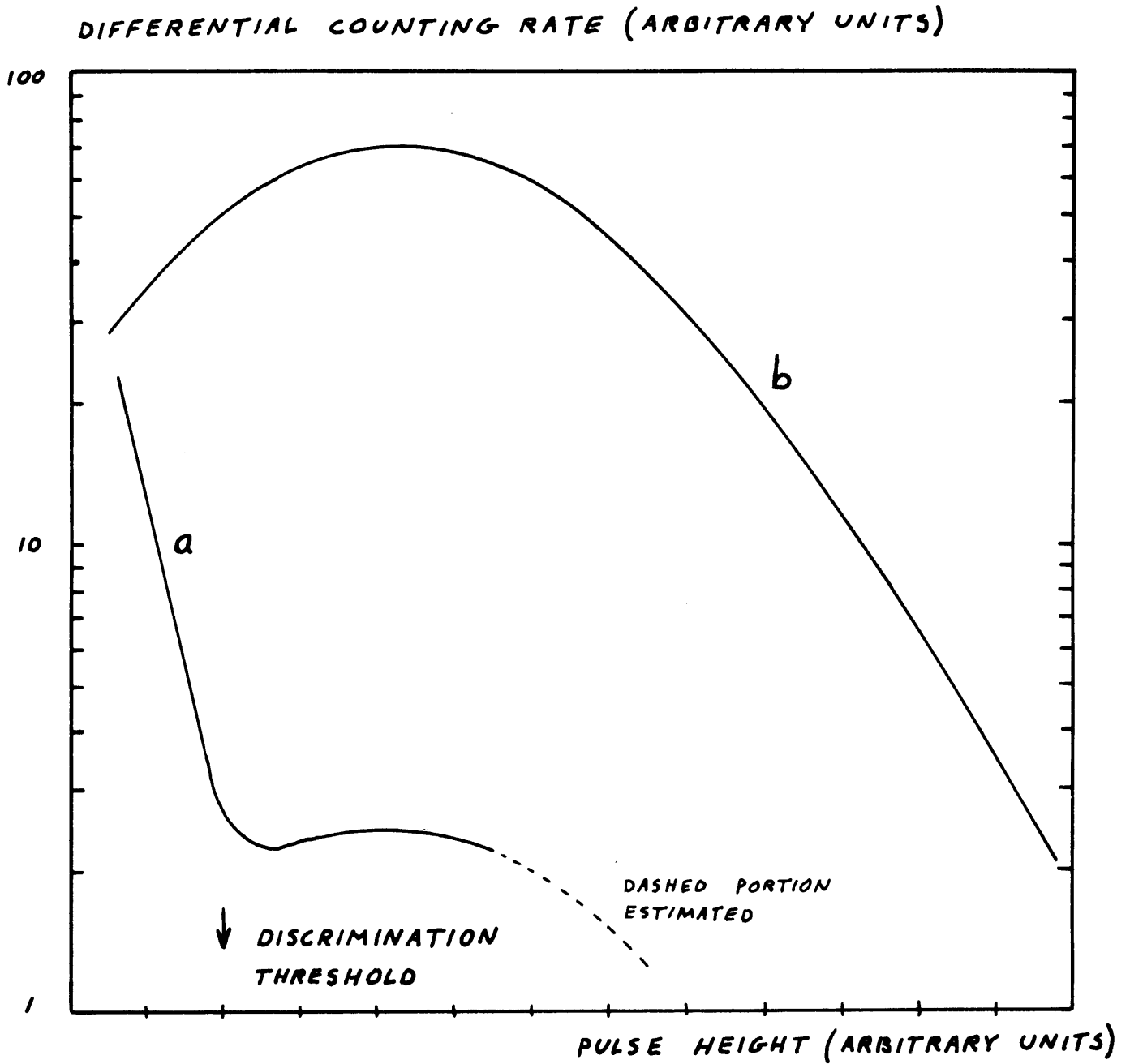


Fig. 3.10 Pulse height spectrum for the phototube.

discrimination. A similar comparison made on curve b indicates a rejection of most of the dark pulses. For each pulse it accepts, the analyzer produces a single standardized pulse, thereby giving equal experimental weight to all anode pulses above the discrimination level. The resulting system has a dark count of 3 pulses per second and has an effective quantum efficiency of about 2.5%. The signal consisting of the pulses from the single channel analyzer is passed through a filter with an adjustable time constant. The output of the filter is a voltage proportional to the counting rate averaged over a period equal to the time constant of the filter. This voltage is recorded on a strip chart recorder.

The significant portions of all spectra investigated produced a counting rate at least 5 times larger than the dark counting rate. Therefore the signal to noise ratio expected, and indeed observed on the traces, is given by the square root of the average number of signal counts occurring within one time constant of the filter. The noise in the experiment is just this shot noise due to the signal itself.

F. Sensitivity

In order to determine the sensitivity of this method of investigating the scattering spectrum, it is convenient to make the following definitions:

$\sigma(\theta)$ is the probability per unit length that a given photon in the laser beam will be scattered into a unit solid angle about the scattering angle θ ,

Ω is the solid angle about θ that is detected by the spectrometer,

L is the length of the beam under observation,

$W(\omega)$ is the fraction of the total spectrum that falls under the instrumental profile of the spectrometer when it is centered at a frequency shift ω ,

α is probability that a scattered photon is lost while going through the optics of the system (this corresponds to imperfect optics, absorption in the coatings and general misalignment),

and Q is the effective quantum efficiency of the detector.

If the laser beam contains N_L photons per second, then the detected counting rate, N_D , is given by

$$N_D = Q \sigma(\theta) \Omega L W(\omega) \alpha N_L. \quad 3.28$$

When conical lenses are used to gather the scattered light $L \Omega$ is given by equation 3.7. In that equation $\Delta\theta_A$ may be substituted for $\Delta\theta_M$ since their difference is small (see table 3.1). For the FFP, $\Delta\theta_A$ corresponds to $2\epsilon_M = 1.1 \times 10^{-3}$ radians. For the SFP, $\Delta\theta_A$ corresponds to the acceptance angle of the apertured cavity, $2a/R$ radians, multiplied by the demagnification of the lens shown in figure 3.1. The lens reduces the scattered beam from a radius $r_\delta = 12.7$ mm outside the cell to a radius $a = 1.8$ mm as it enters the SFP; this corresponds to a demagnification of $1.8/12.7 = .14$ and $\Delta\theta_A = 5 \times 10^{-3}$ radians.

Equation 3.28 can be reduced in complexity somewhat by

substituting in values which are known up to now for the case of the particular lens which gives scattering at $\theta = 10.6^\circ$ or 169.4° . Let the power of the laser beam be denoted by P and be measured in watts. To convert between power and counting rate note that 3.19×10^{18} photons per second correspond to one watt at 6328 \AA . Therefore equation 3.28 becomes

$$N_D \sim (5 \times 10^{14} \frac{\text{cm}}{\text{watt}})_F \sigma W \alpha P, \quad 3.29$$

$$\sim (25 \times 10^{14} \frac{\text{cm}}{\text{watt}})_S \sigma W \alpha P.$$

These relations will be used in the next chapter to estimate the efficiency of the system.

References for Chapter III

1. The use of conical lenses was suggested to us by Professor D. J. Bradley, now at the Physics Department, University of Belfast, Northern Ireland.
2. W. E. Lamb, Phys. Rev. 134, A 1429 (1964).
3. P. A. Fleury and R. Y. Chiao, J.A.S.A. 39, 751 (1966).
4. G. B. Benedek and T. J. Greytak, Proc. I. E. E. E., 53, 1623 (1965).
5. T. T. Saito, M. S. Thesis, MIT, 1966 (unpublished).
6. Millipore Filter Corporation; Bedford, Massachusetts.
7. K. W. Meissner, J.O.S.A., 31, 405 (1941).
8. P. Connes, Revue d'Optique, 35, 37 (1956) and J. de Physique et Radium, 19, 262 (1958).
9. P. Jacquinet, Reports on Progress in Physics, 23, 273 (1960).
10. We are particularly grateful to Professor B. Stoicheff, now at University of Toronto, Canada, for loaning to us a copy of the plans for his etalon.
11. D. H. Rank and J. N. Shearer, J.O.S.A., 46, 463 (1956).
12. The necessity for specifications as stringent as these for the successful operation of a SFP were first emphasized by D. Jackson, Proc. Roy. Soc., 263A, 289 (1961).
13. The use of pulse height discrimination as a means of increasing the signal to noise ratio in photomultipliers was first suggested by G. E. Kron, Astrophys. J. 103, 324 (1946). In the same article he also pointed out the advantage of a small photocathode.
14. The most recent and extensive work on the use of photomultipliers for photon counting has been done by E. H. Eberhardt of ITT Industrial Laboratories. Some of this work is reported in E. H. Eberhardt, Electrical Communication 40, 124 (1965) and in the Final Report on NASA Contract # NAS w 1038, "Research in the Development Effort of an Improved Multiplier Phototube". The latter is available from the NASA Scientific and Technical Information Facility.

Chapter IV

Experimental Results

In this chapter the experimental results are presented and the physical information which they contain is discussed. Sections A and B deal with scattering through angles of 10.6° and 22.7° respectively. The wavelengths of the fluctuations observed at these angles are long compared to the mean free paths in the gases under the experimental conditions. A comparison of the theoretical Maxwell molecule spectra in this region with the theoretical hydrodynamic spectra for a monatomic gas has been made by Ranganathan and Yip⁽¹⁾. The results show that the differences between the two sets of spectra cannot be observed with the resolution of the present experiment. Therefore the experimental spectra at these two angles are compared only to hydrodynamic calculations.⁽²⁾ Section C deals with scattering through an angle of 169° . The wavelength of the fluctuations observed at this angle approaches the mean free path of the molecules. The experimental results for xenon and carbon dioxide show a qualitative disagreement with the theoretical spectra computed on the basis of hydrodynamics. The results for xenon can also be compared with kinetic spectra based on the model of Bhatnagar, Gross, and Krook⁽³⁾ and on the Maxwell molecule calculations.⁽¹⁾ The comparison afforded by the Krook model is ambiguous but shows a qualitative agreement between experiment and theory. The Maxwell molecule spectrum represents the general features of the experimental results very well, but a quantitative difference outside the

experimental limits of error is observed. The overall efficiency of the experimental arrangement, relative to a perfectly aligned, lossless optical system, is calculated in section D.

A. Scattering at 10.6°

The scattering of light of wavelength 6328 \AA in the medium through an angle of 10.6° corresponds to a scattering vector \vec{K} whose magnitude (equation 2.2) is $1.84 \times 10^4 \text{ cm}^{-1}$. The wavelength of the fluctuations which give rise to this scattering λ_F is then $2\pi/K = 3.41 \times 10^{-4} \text{ cm}$. Most of the data presented in this thesis was taken at pressures near one atmosphere. The mean free path L of the molecules under these conditions can be estimated from the relation⁽⁴⁾

$$\eta = \frac{1}{3} m L \rho_0 \langle |\vec{v}| \rangle \quad 4.1$$

where η is the viscosity, $m\rho_0$ is the mass density and \vec{v} is the molecular velocity. Five gases are studied at this angle (Xe, CO_2 , CH_4 , N_2 , and A) and by using the thermal parameters given in table 2.2 one finds that L increases in that order from $0.6 \times 10^{-5} \text{ cm}$ in Xe to $1.0 \times 10^{-5} \text{ cm}$ in A. Therefore λ_F/L varies from about 57 in Xe to 34 in A. Using the expression for the kinetic parameter y relevant to the Maxwell molecule calculations (equation 2.84) and the mean free path L defined on the basis of 4.1 one has the relationship $\lambda_F/L = 2\pi \sqrt{4/\pi} y$. Of course y is defined only for monatomic gases. At this angle, then, for Xe one finds $y \sim 8$.

Figure 4.1 shows sections of typical experimental runs on Xe,

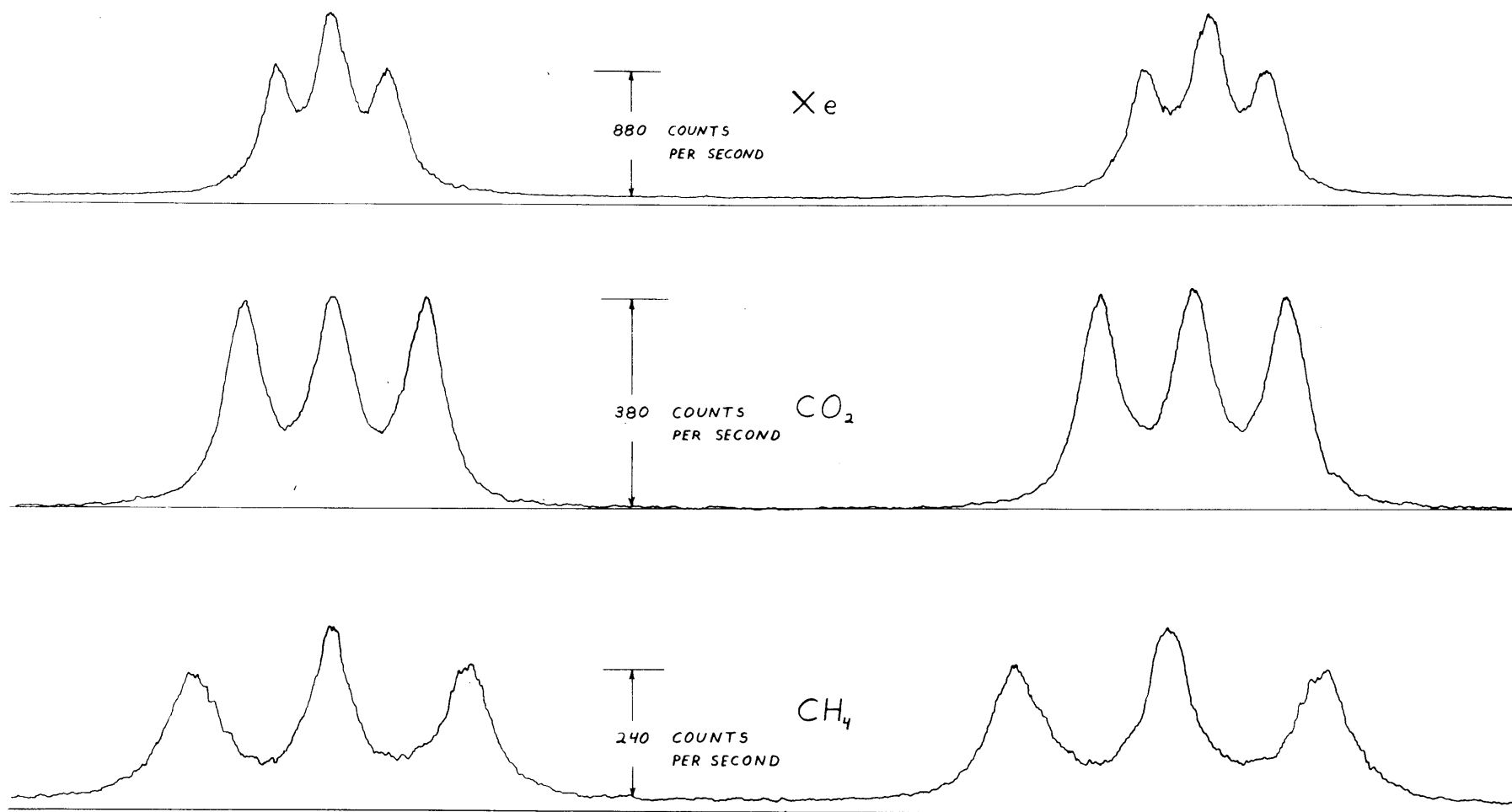


Fig. 4.1 Experimental traces taken at $\theta = 10.6^\circ$.

CO₂, and CH₄. Each spectrum shows clearly an unshifted line due to the scattering from entropy fluctuations and to stray light which is present even if the scattering cell is evacuated. Also present are a pair of Brillouin components shifted by about 100 MHz to either side of the central line. The distance between successive spectra on each trace corresponds to the free spectral range of the spherical Fabry-Perot interferometer (750 MHz). A displacement of some fraction of the inter-order spacing corresponds to a frequency shift of that fraction of 750 MHz. The shape of each of the three lines is determined primarily by the instrumental profile of the interferometer since its full width at half height (about 28 MHz) is larger than the intrinsic widths of the lines expected at this angle (see table 2.3). The spectrometer sweeps through one free spectral range in about 10 minutes. The integration times used were 1, 3, and 2 seconds for the Xe, CO₂ and CH₄.

Table 4.1 lists the Brillouin shifts measured in the five gases and the velocities calculated from them using equation 2.66. The frequency shifts represent the average from about 10 spectra taken during a single run and the uncertainties listed are the RMS fluctuations of the separate values about their average. Also listed in the table are velocities measured by standard acoustic techniques at lower frequencies. In the polyatomic gases a dispersion in the sound velocities is known to occur at frequencies well below 1 MHz (~ 1 Hz in N₂⁽⁵⁾, 35×10^3 Hz in CO₂⁽⁵⁾, and 186×10^3 Hz in CH₄⁽⁶⁾; at one atmosphere) due to the relaxation of the vibrational degrees of

Table 4.1

Brillouin shifts and velocities for scattering at an angle 10.6° .

Gas	Pressure mm Hg	Temperature $^\circ\text{C}$	$\Delta\nu$ MHz	Computed C m/s (Hypersonic)	Low Frequency* C m/s (Ultrasonic)
A	770	28°	93.0 ± 2.0	318 ± 6	323^a
Xe	795	25.2°	50.8 ± 2.0	174 ± 7	178^a
N_2	770	28°	100.5 ± 2.0	344 ± 7	354^b
CO_2	770	24.9°	81.5 ± 1.2	279 ± 4	281^c
CH_4	777	24.7°	129 ± 4	442 ± 13	454^d

* Measured at frequencies above any vibrational relaxations.

^a M. Greenspan, J. Acous. Soc. Am. 28, 644 (1956).

^b M. Greenspan, J. Acous. Soc. Am. 31, 155 (1959).

^c Henderson and Peselnick, J. Acous. Soc. Am. 29, 1074 (1957).

^d B. T. Kelly, J. Acous. Soc. Am. 29, 1005 (1957).

freedom. The velocities listed for the polyatomic molecules are those measured above the region of vibrational dispersion.

The low frequency sound speed computed on the basis of hydrodynamics is given by⁽⁷⁾⁽⁸⁾

$$C = \left(\gamma \frac{RT}{m} \right)^{1/2} (1 + \delta) \quad 4.2$$

where R is the gas constant and δ is a correction (of the order of 10^{-3} at one atmosphere) for the non-ideal nature of the gas. Well above the vibrational relaxation frequencies mentioned above, polyatomic gases exhibit a sound speed which is higher than that given by equation 4.2. Physically this effect is attributed to the fact that vibrational energy levels of the molecules have life times which are long compared to the period of the sound wave. Therefore the population of these vibrational levels cannot change fast enough to enter into the dynamics of sound wave propagation. The vibrational degrees of freedom are said to be 'frozen out' at frequencies whose corresponding periods are much shorter than the lifetimes of the vibrational levels.

Classically the specific heat ratio γ for a gas can be expressed in terms of the number of degrees of freedom N of the molecules by the relation $\gamma = 1 + 2/N$. If one were to take into account only the translational and rotational degrees of freedom, γ would therefore assume the value 1.667 for monatomic gases, 1.400 for a gas of linear molecules, and 1.333 for more complex polyatomic gases. These values of γ are higher than the thermodynamic ones given in

table 2.2 since physically the vibrational energy levels are populated to some extent at room temperature and enter into the macroscopic energy balance and energy transport phenomena. The picture of a vibrational dispersion of the sound velocity as a 'freezing out' of the vibrational degrees of freedom therefore suggests that equation 4.1 might still hold well above the relaxation frequency if the thermodynamic value of γ were replaced by the vibrationless γ 's listed above. The velocities measured by ultrasonic methods show that this is indeed the case. In fact, equation 4.2 can be used to define a frequency dependent specific heat ratio in terms of the sound speed data. This concept of a frequency dependent γ will be useful below when other details of the spectrum are discussed.

The 'hypersonic' velocities measured from the Brillouin shift agree within experimental uncertainty with the ultrasonic values. However, the hypersonic velocities are on the average 2% lower than the ultrasonic ones. This is strongly suggestive of a systematic error. The apparent center of the Brillouin components is drawn toward the center of the spectrum by the overlap between the central and Brillouin portions of the trace. This effect amounts to about 1% of the Brillouin shift and was taken into account in the reduction of the data. The free spectral range of the interferometer was checked against the side bands of a laser beam modulated at about 10 GHz by a KDP crystal driven by an extremely accurate microwave source.⁽⁹⁾ It was found that at the mirror separation corresponding to the optimum finesse the spherical Fabry-Perot interferometer had a free spectral

range of $750.39 \pm .05$ MHz. As a result of these checks the systematic error if it does exist is believed to lie in the determination of the angle of the conical lens.

Next, a detailed examination of the spectra can be made by comparing the experimental traces with the theoretical results based on the hydrodynamic theory outlined in section C1 of chapter II. The result obtained by measuring a frequency spectrum $A(\nu)$ with a spectrometer whose instrumental profile $B(\nu)$ is swept at a constant rate across A can be shown to be the convolution $A \otimes B$ of the two functions:⁽¹⁰⁾

$$A(\nu) \otimes B(\nu) \equiv \int_{-\infty}^{\infty} A(\nu') B(\nu - \nu') d\nu' \quad 4.3$$

In these experiments $A(\nu)$ is proportional to the spectral power density function $S_{\rho}(K, 2\pi\nu)$ of the fluctuations in the number density. This was discussed at length in Chapter II and has been calculated digitally by a computer for the three approximations outlined there. The instrumental profile $B(\nu)$ includes the transmission function of the interferometer, the finite width of the frequency spectrum of the laser (about 5 MHz due to the frequency stabilization scheme employed; see section B.2 of Chapter III), and the effect of the finite integration time. The instrumental profile is measured experimentally by recording the output of the system in response to the light elastically scattered by a dilute aqueous suspension of polystyrene balls placed in the scattering cell after an experimental run is made. This instrumental profile is digitalized and

and convolved numerically by the computer with the theoretical spectrum intrinsic to the scattering process.

Figures 4.2, 4.3, and 4.4 show individual traces taken in the three strongest scatterers investigated: Xe, CO₂, and CH₄. Superimposed on these traces are the theoretical results (the dashed curves) computed from the exact solution of the linearized hydrodynamic equations given by Mountain.⁽²⁾ The parameters involved in the theory were taken, with the exception of the velocity, from table 2.2. The velocity used was that measured from the Brillouin shift. Of the three gases, CH₄ has the broadest intrinsic line widths; figure 4.5 illustrates the results of the convolution for CH₄ by showing on the same frequency scale $A(\nu)$, $B(\nu)$, and $A(\nu) \otimes B(\nu)$. The experimental traces include a certain amount of stray elastically scattered light (which would have a spectrum identical to that of the instrumental profile). The height of the central peak due to the gas alone can be found by subtracting the amplitude of the stray light spectrum obtained when the evacuated cell is run. This corrected central peak height and its estimated uncertainty is indicated by the vertical interval I. The theoretical spectra are normalized to the heights of the Brillouin peaks, which are not effected by the stray light.

Figure 4.2 shows that the comparison between theory and experiment for Xe is good; but, it must be pointed out that the intrinsic widths of the central and Brillouin lines are only 25% and 19% of the instrumental line. The Landau-Placzek ratio is defined to be the ratio of the intensity in the central line to the sum of the intensities in the two

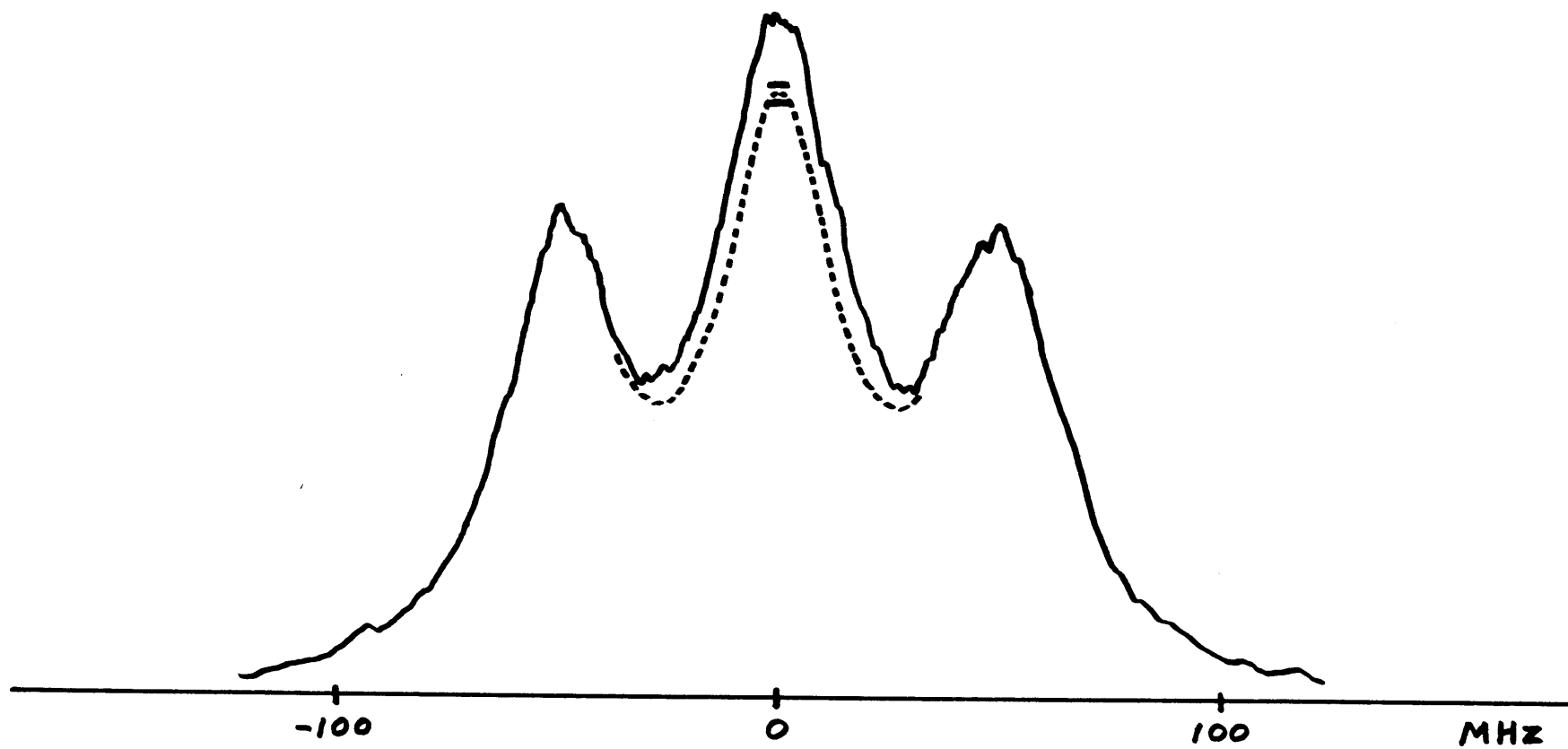


Fig. 4.2 Xe spectrum at $\theta = 10.6^\circ$.

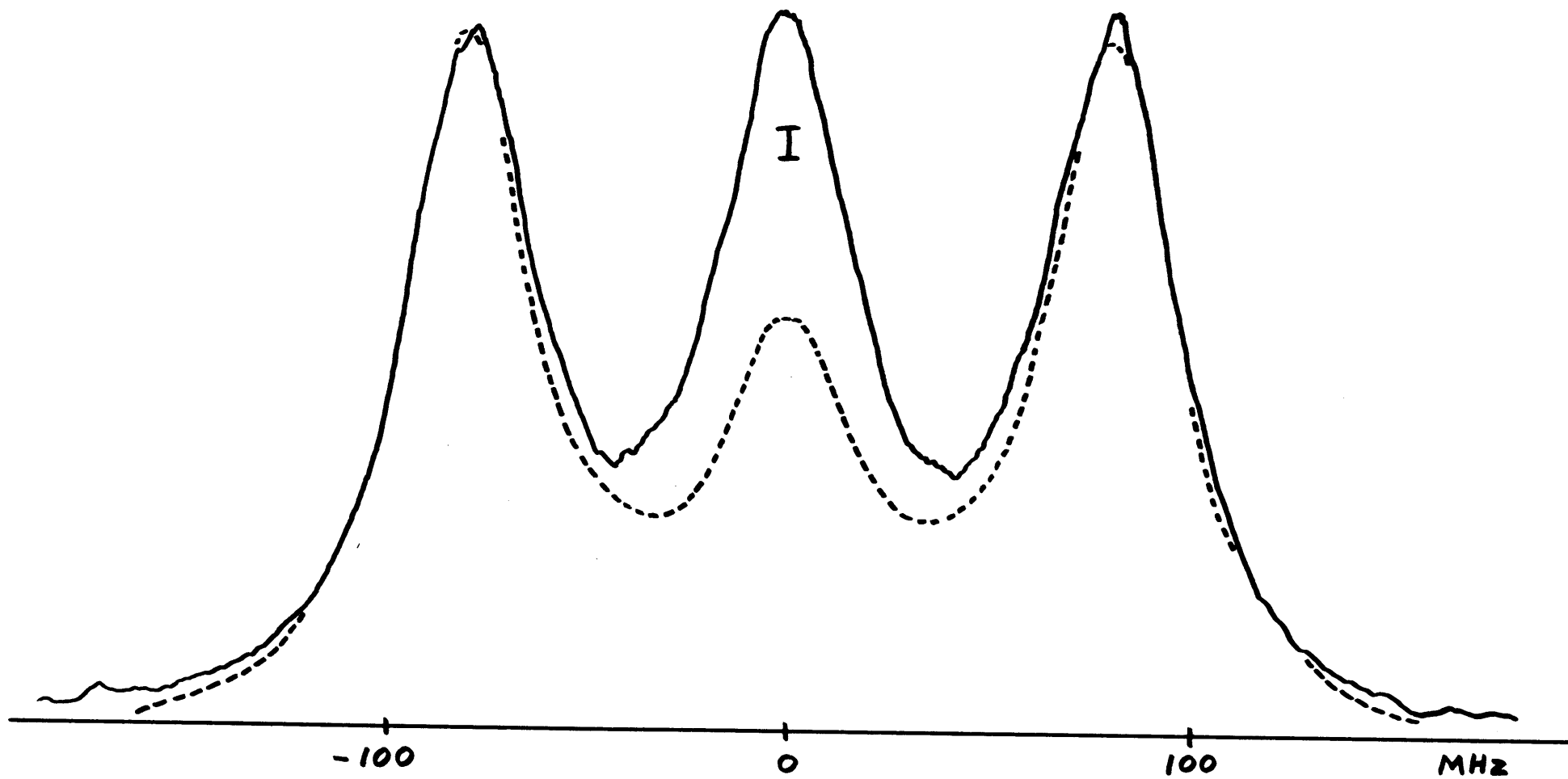


Fig. 4.3 CO₂ spectrum at $\theta = 10.6^\circ$.

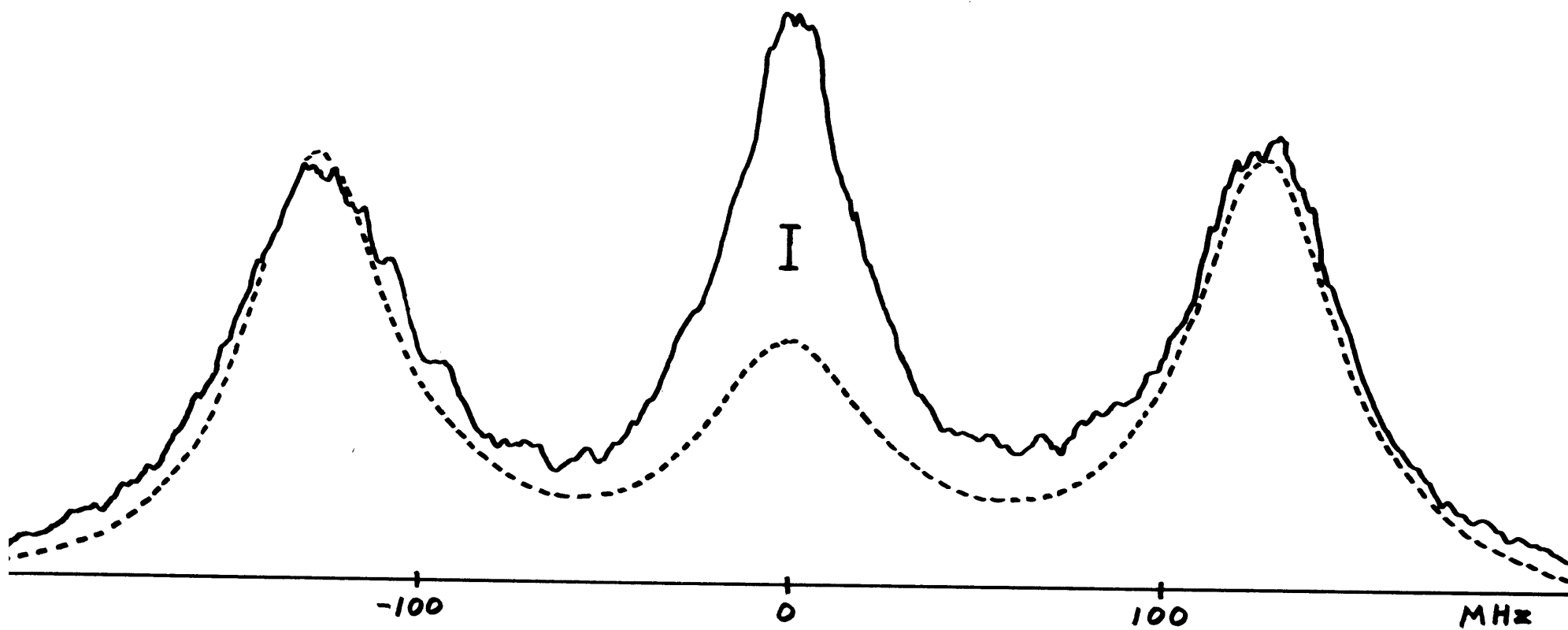


Fig. 4.4 CH_4 spectrum at $\theta = 10.6^\circ$.

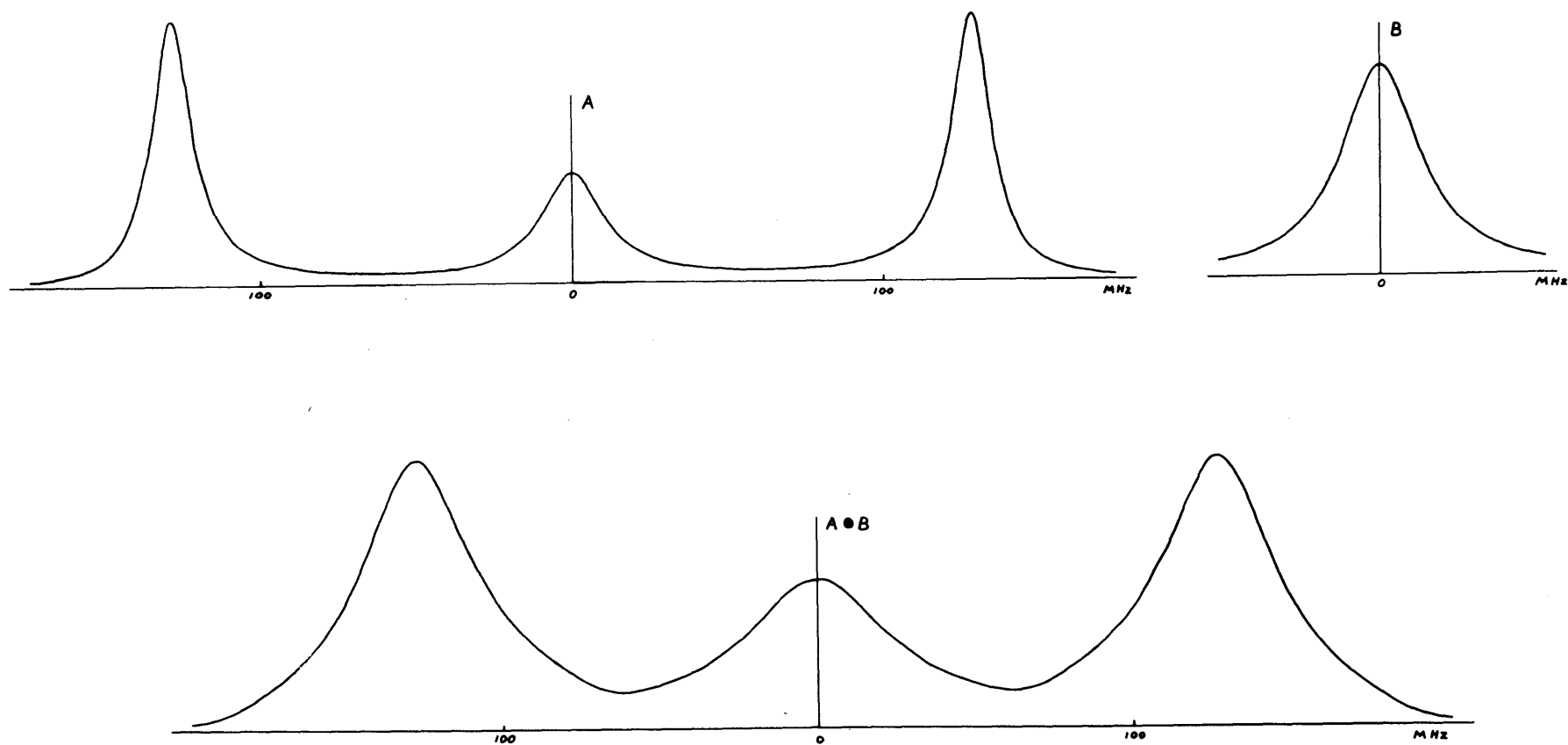


Fig. 4.5 Effect of convolution on the spectrum of CH_4 at $\theta = 10.6^\circ$.

Brillouin components. This ratio, computed from the hydrodynamic theories, is $\gamma - 1$. If the intrinsic line widths are narrow compared to the instrumental width and there is no overlap between the lines on the recorded trace, then the Landau-Placzek ratio is given by the ratio of the height of the corrected central peak to twice the height of the Brillouin components. From figure 4.2 it can be seen that the condition of non-overlapping lines does not apply. In fact the Landau-Placzek ratio computed from the heights of the components in the theoretical convolved trace is 0.656, while the true ratio of the areas of the components computed from the theoretical spectrum before convolution is the correct value 0.667. Therefore the height ratio as measured from the experimental traces is not an accurate way of determining the Landau-Placzek ratio, and thereby finding γ . Nevertheless a comparison of this ratio between the theoretical spectra and the measured spectra can indicate whether the value of γ used in the theory is consistent with the experimental results. The fact that the central peak of the theoretical trace in figure 4.2 passes exactly through the corrected experimental peak indicates that a value of $\gamma = 1.667$ applies even to phenomena occurring at 50 MHz (the frequency of the thermal sound waves giving rise to the Brillouin components).

Figure 4.3 shows a good agreement between theory and experiment in the Brillouin components of CO_2 . The intrinsic Brillouin width from table 2.3 is 27% of the instrumental width. In the region of the central peak, however, there is a substantial difference between theory and experiment. The theoretical curve rises only to about 70%

of the corrected experimental central peak. This is to be expected, however, since the theory is based on a static value for γ of 1.302. Acoustic measurements show that in this frequency region, at least as far as sound velocities are concerned, the vibrational degrees of freedom are 'frozen out' and the proper value of γ is 1.400. The way in which the 'freezing out' of the vibrational degrees of freedom would modify the hydrodynamic spectrum (which includes the diffusion as well as acoustic behavior) is not clear. Yet, it is tempting to consider a Landau-Placzek ratio which excludes the vibrational levels. This ratio would have the value 0.400. Scaling the theoretical central peak height by the appropriate factor, $0.400/0.302$, brings it up to 94% of the corrected experimental central peak height, just below its RMS experimental uncertainty.

Figure 4.4 represents the situation in CH_4 . The experimental Brillouin components seem slightly wider than the theory indicates. From table 2.3 one finds that the intrinsic Brillouin and central components based on the hydrodynamic theory are 57% and 89% as wide as the instrumental profile. This makes a marked and measurable effect on the resulting spectrum as illustrated in the convolution example in figure 4.5. Again the theory, based on a static $\gamma = 1.310$, underestimates the height of the central component. The vibrationless γ would be 1.333. Scaling the theoretical central peak by $0.333/0.310$ raises it from 72% to 77% of the corrected experimental central peak. This is still outside the RMS uncertainty in the central peak, but the scaling procedure itself is made suspect by the broad intrinsic lines

and strong overlap. Increasing the theoretical Brillouin widths to secure a closer fit to the experiment would, simply because of the overlap, increase the height of the theoretical central peak.

There is some experimental evidence that sound waves in N_2 ⁽¹¹⁾, O_2 ⁽¹²⁾, and CH_4 ⁽¹³⁾ undergo a rotational relaxation at very high frequencies analogous to the vibrational relaxation at lower frequencies. Relaxation frequencies, both vibrational and rotational, are generally directly proportional to the pressure. The experiments cited above were done at pressures well below one atmosphere to bring the frequency region of interest into the range of ultrasonic techniques. At a pressure of one atmosphere the rotational relaxation frequencies would be in the several hundred MHz region. The effects of such a relaxation would be an increase in the sound speed corresponding to an increase in γ in equation 4.2, and an increase in the attenuation of sound waves above the classical value calculated from equation 2.67. Kelly's results⁽¹³⁾ on CH_4 suggest a rotational relaxation frequency of 300 MHz at one atmosphere. At about 130 MHz (the Brillouin shift in the present experiment at one atmosphere) his results would indicate an increase in the sound velocity of 3% over that given in table 4.1 and an increase in the attenuation of the sound wave by a factor of about 1.8. This velocity increase is about equal to the uncertainty in the velocity measured in this experiment. The increase in attenuation seems a bit higher than that necessary to explain the Brillouin widths in figure 4.4. In any case, the scattering experiments will be improved with regard to resolution, stray light, and signal to noise ratio. The question of a

rotational relaxation, particularly in CH_4 , can then be studied easily with this technique as these preliminary measurements have shown.

B. Scattering at 22.7°

At this angle $K = 3.91 \times 10^4 \text{ cm}^{-1}$ and the wavelength of the fluctuations observed is $1.61 \times 10^{-4} \text{ cm}$. Only two gases, Xe and CO_2 , were investigated at this angle and for them the ratios of the wavelength of the fluctuation to the mean free path are 28 and 25. The value of the kinetic parameter γ is about 4 for Xenon. The spectra at this angle differ in two aspects from those discussed above for $\theta = 10.6^\circ$. First, since the ratio of λ_F/L is smaller, one expects that the differences between the spectra calculated on the basis of hydrodynamics and those based on kinetic theory will be more pronounced. Second, on the basis of hydrodynamics alone the central and Brillouin components are beginning to overlap, indicating that diffusion and sound propagation are no longer completely independent normal modes of the medium. Unfortunately the conical lens for $\theta = 22.7^\circ$ is not as efficient as the one for $\theta = 10.6^\circ$ because of its smaller effective aperture. The fact that the lines now have widths comparable to or larger than the instrumental width is an advantage in comparing the theoretical spectra to the experiment. On the otherhand, a smaller fraction of the total intensity in a given spectrum passes through the spectrometer at one time. For this reason CH_4 , although a strong scatter, could not be investigated. Its Brillouin components were so broad (72 MHz from table 2.3) that they could barely be resolved from the background.

Because of the overlap between the central and Brillouin parts of the spectrum the concept of a Brillouin shift is no longer well defined. For this reason no calculations of hypersonic sound velocities are made for this scattering angle. The experimental traces are compared directly with the hydrodynamic spectra based on the ultra-sonic sound velocities shown in table 4.1. Figures 4.6 and 4.7 show typical traces of Xe and CO₂ upon which the theoretical hydrodynamic spectra have been superimposed. Figure 4.8 is the convolution example relative to the CO₂ trace.

Figure 4.6 shows that for Xe the agreement between the theory and experiment is good. The apparent displacement of the center of the theoretical Brillouin components relative to the experimental ones is a property of this particular experimental trace. On the basis of an average taken over a number of traces, the Brillouin components do coincide. A comparison of this figure with figure 4.2 representing Xe at 10.6° shows that the stray elastically scattered light forms a much larger part of the spectrum at this angle. The corrected height of the central peak can still be determined quite accurately and can be seen to agree with the theoretical value. From table 2.3 the intrinsic theoretical Brillouin and central line widths are 0.9 and 1.1 times as wide as the instrumental profile.

Figure 4.7 shows the spectrum of CO₂ at this angle. The agreement between theory and experiment is satisfactory in the region of the Brillouin components, however, the large proportion of stray light prevents a meaningful comparison in the region of the central compon-

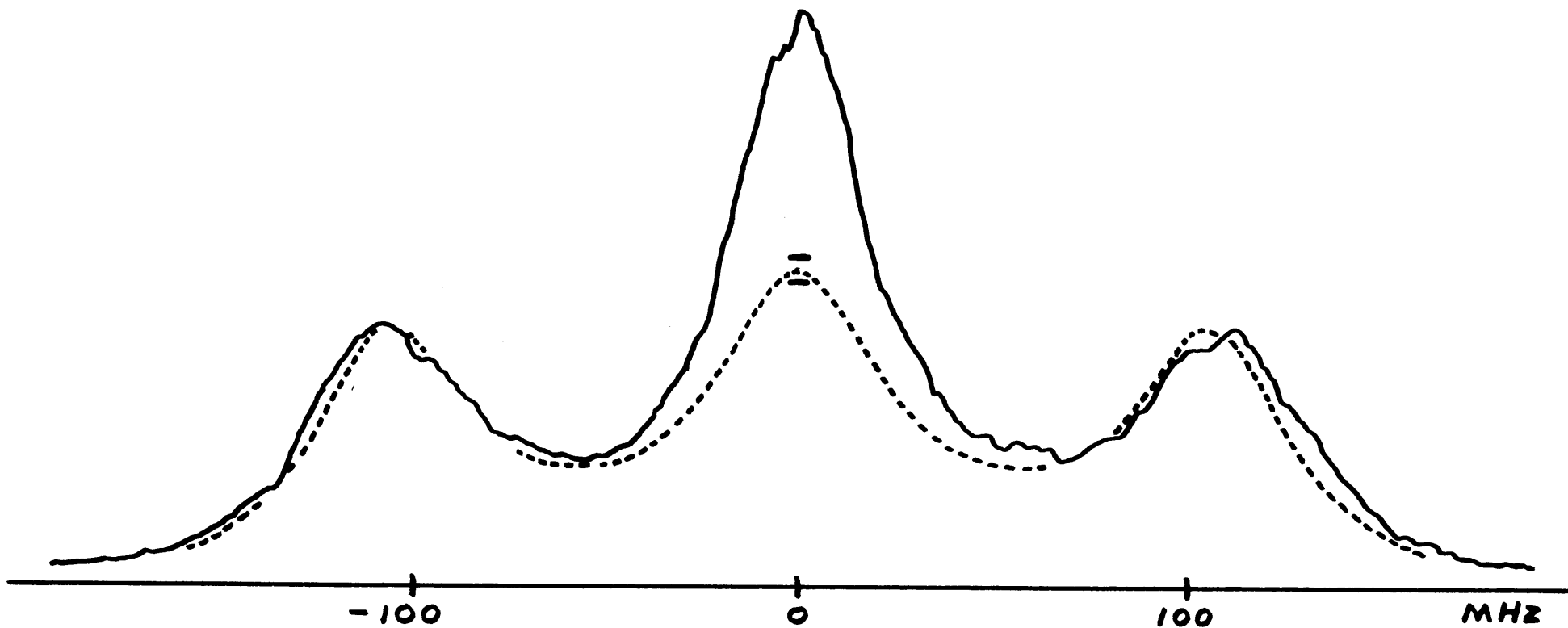


Fig. 4.6 Xe spectrum at $\theta = 22.7^\circ$.

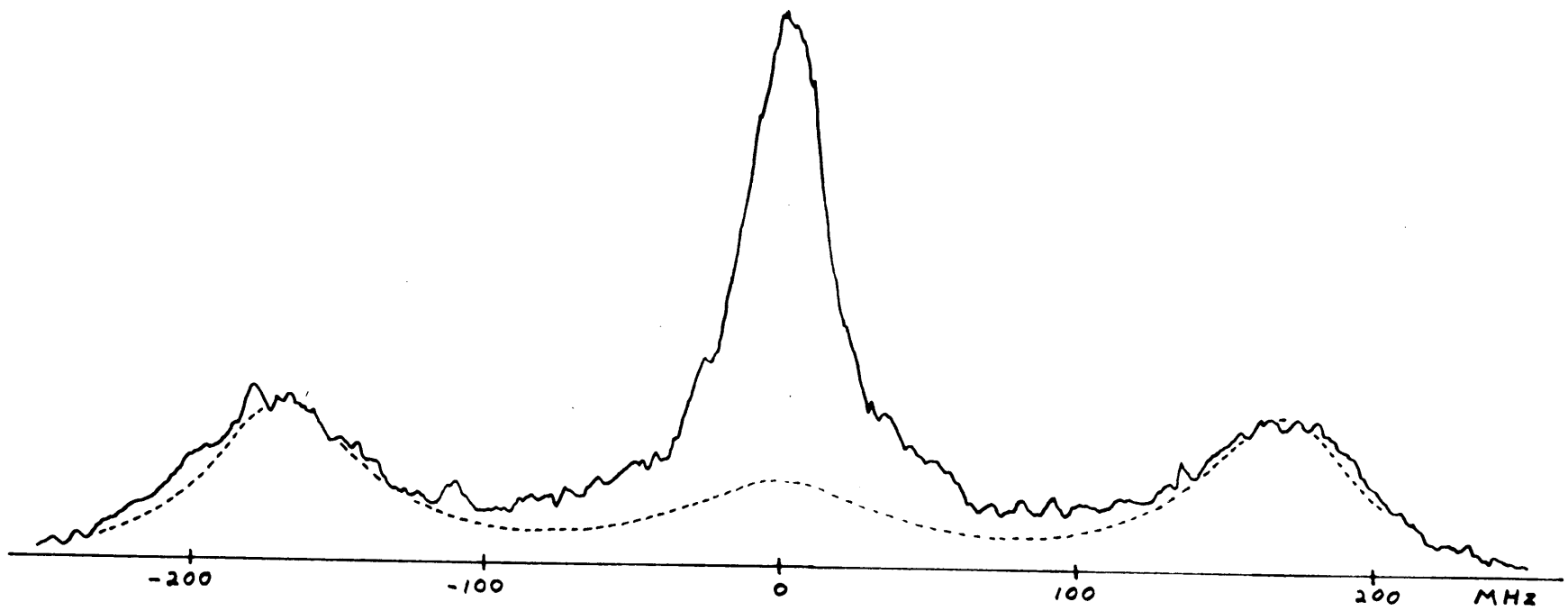


Fig. 4.7 CO₂ spectrum at $\theta = 22.7^\circ$.

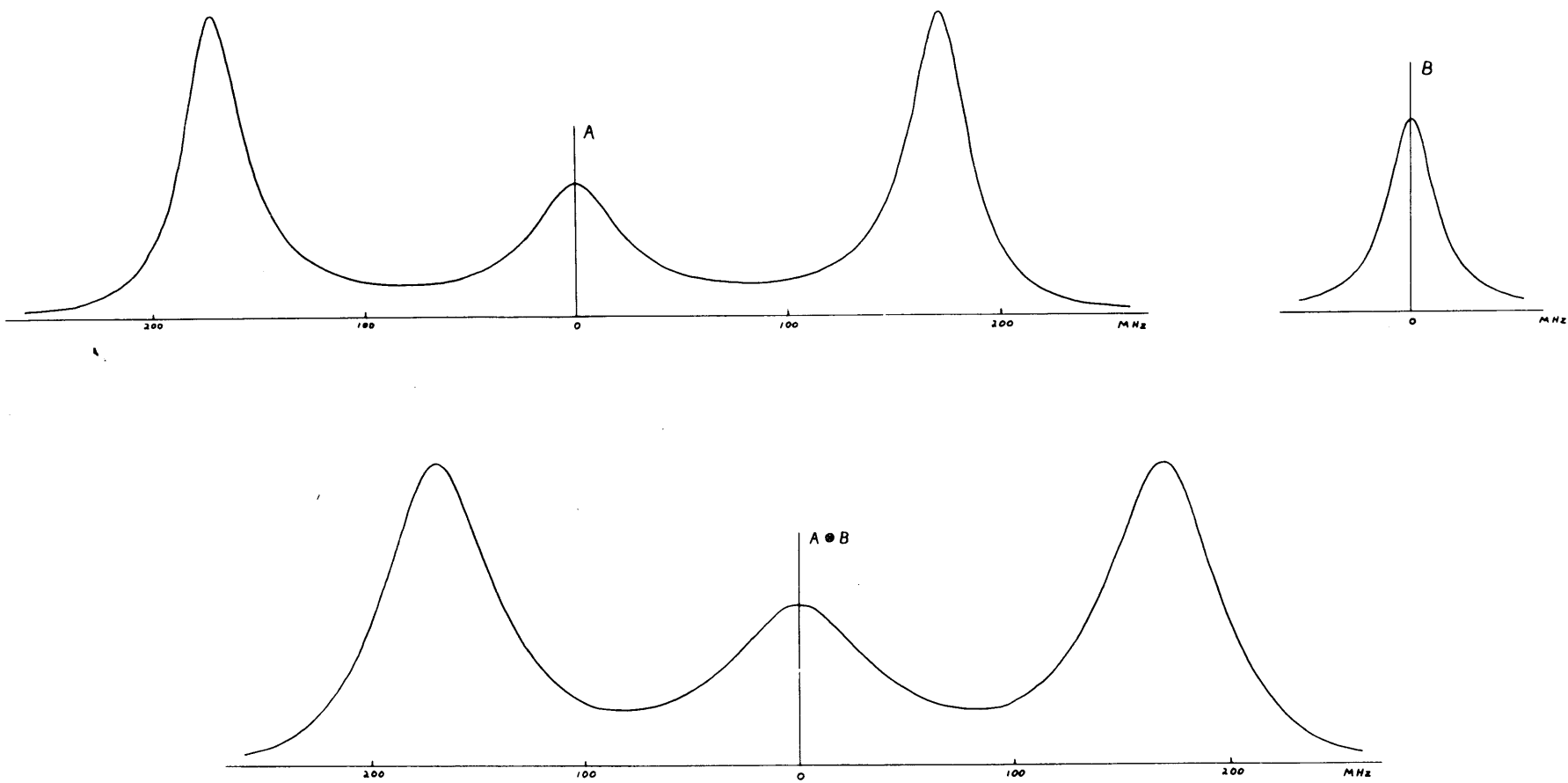


Fig. 4.8 Effect of convolution on the spectrum of CO_2 at $\theta = 22.7^\circ$.

ent. The values taken from table 2.3 show that in theory the Brillouin and central component widths are 1.2 and 1.9 times as wide as the instrumental profile. The curve $A(\nu)$ in figure 4.8 represents the intrinsic theoretical spectrum and shows considerable overlap between the three components.

C. Scattering at 169°

At this angle $K = 1.98 \times 10^5 \text{ cm}^{-1}$ and the wavelength of the fluctuations giving rise to the scattering is $3.18 \times 10^{-5} \text{ cm}$, about half of the wavelength of the light being scattered. Only two gases, Xe and CO_2 , were studied at this angle and they correspond to ratios λ_F/L of 5.5 and 5.0 respectively.

Figure 4.9 shows typical traces taken for Xe and CO_2 . The spectra no longer show the three distinct lines characteristic of hydrodynamic behavior. The separation between adjacent orders on each trace is 4.96 GHz, the free spectral range of the flat Fabry-Perot used in the spectrometer. The counting rates indicated in this figure are much lower than those given in figure 4.1 for the same gases in the forward direction. This results from two facts: first, a smaller fraction of the spectrum falls under the instrumental profile of the spectrometer at a given time and, second, the light gathering ability of the flat Fabry-Perot used here is not as high as that of the spherical Fabry-Perot used in the forward direction. One free spectral range was swept every 49 minutes. The integration times were 10 seconds for the Xe trace and 5 seconds for the CO_2 .

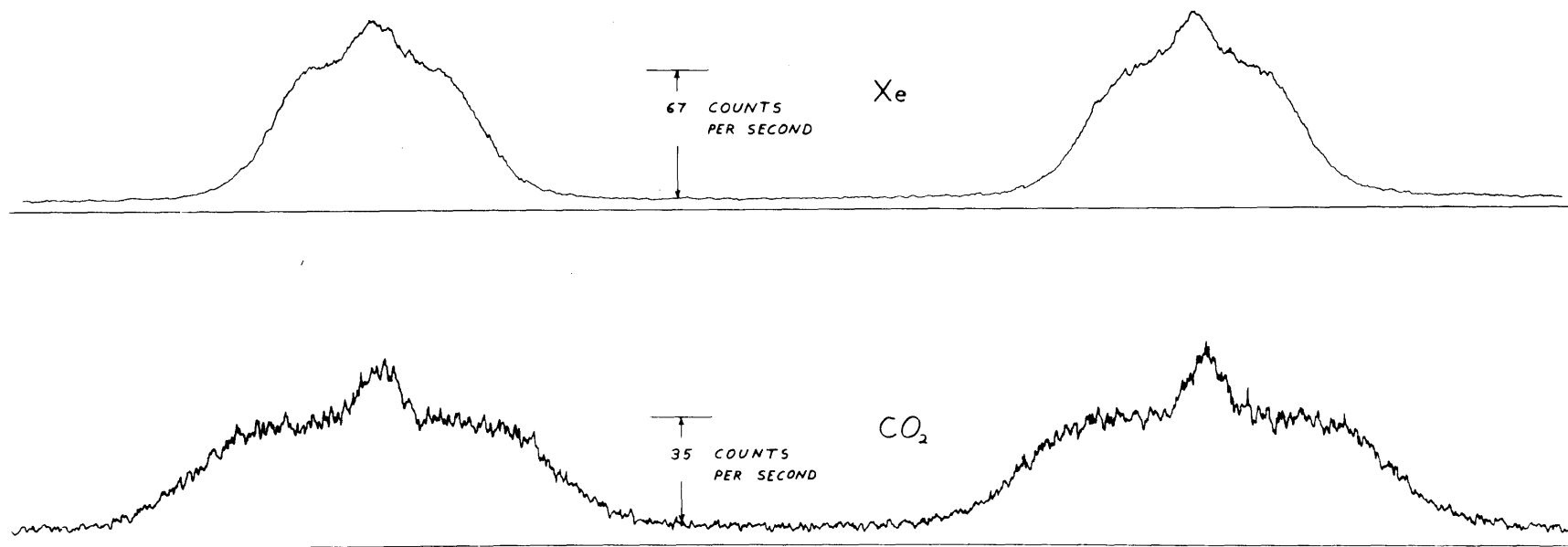


Fig. 4.9 Experimental traces taken at $\vartheta = 169^\circ$.

In order to facilitate a quantitative examination of the Xe spectrum, an average was taken at 41 points across the spectrum for the eight successive traces that comprised one experimental run. For this particular run the temperature was 24.8°C and the pressure was 780 mm of Hg. The average of the stray light spectrum (obtained with an evacuated cell) was computed at the same points. The resulting average experimental spectrum, from which the stray light spectrum has been subtracted, is shown in figures 4.10, 4.11 and 4.12. The RMS variation of the eight individual traces about the average is indicated by the length of the vertical bar through each point. Also shown in the figures are the theoretical traces obtained on the basis of the linearized hydrodynamic equations,⁽²⁾ the Krook kinetic model,⁽³⁾ and the Maxwell molecule calculations.⁽¹⁾ The theoretical traces are obtained by numerical convolution of the instrumental profile and the intrinsic theoretical spectra. They have been normalized to match the experiment (after subtraction of the stray light) at zero frequency shift. Figure 4.13 has been inserted to illustrate the relation between the intrinsic spectrum and the convolved spectrum for Maxwell molecules.

From figure 4.10 it can be seen that the hydrodynamic spectrum differs qualitatively from the experimental results. Hydrodynamics predicts a smooth 'bell shaped' spectrum, yet the experimental spectrum has distinct 'shoulders' in the region where the acoustic modes would appear if the density were increased. The frequency corresponding to $CK/2\pi$ for this angle is 561 MHz. This theory also underestimates

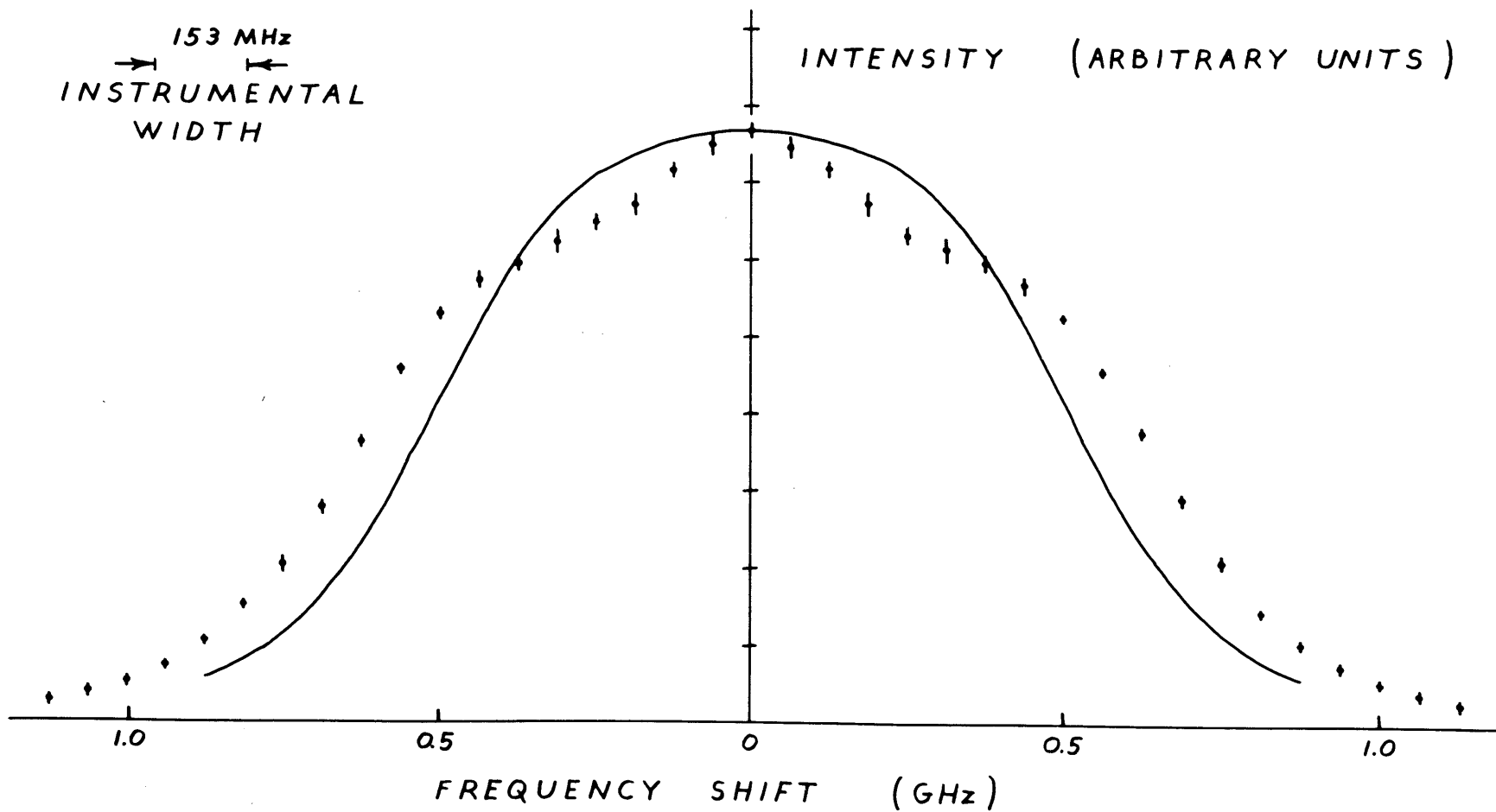


Fig. 4.10 Xe spectrum at $\theta = 169^\circ$ and the hydrodynamic theory.

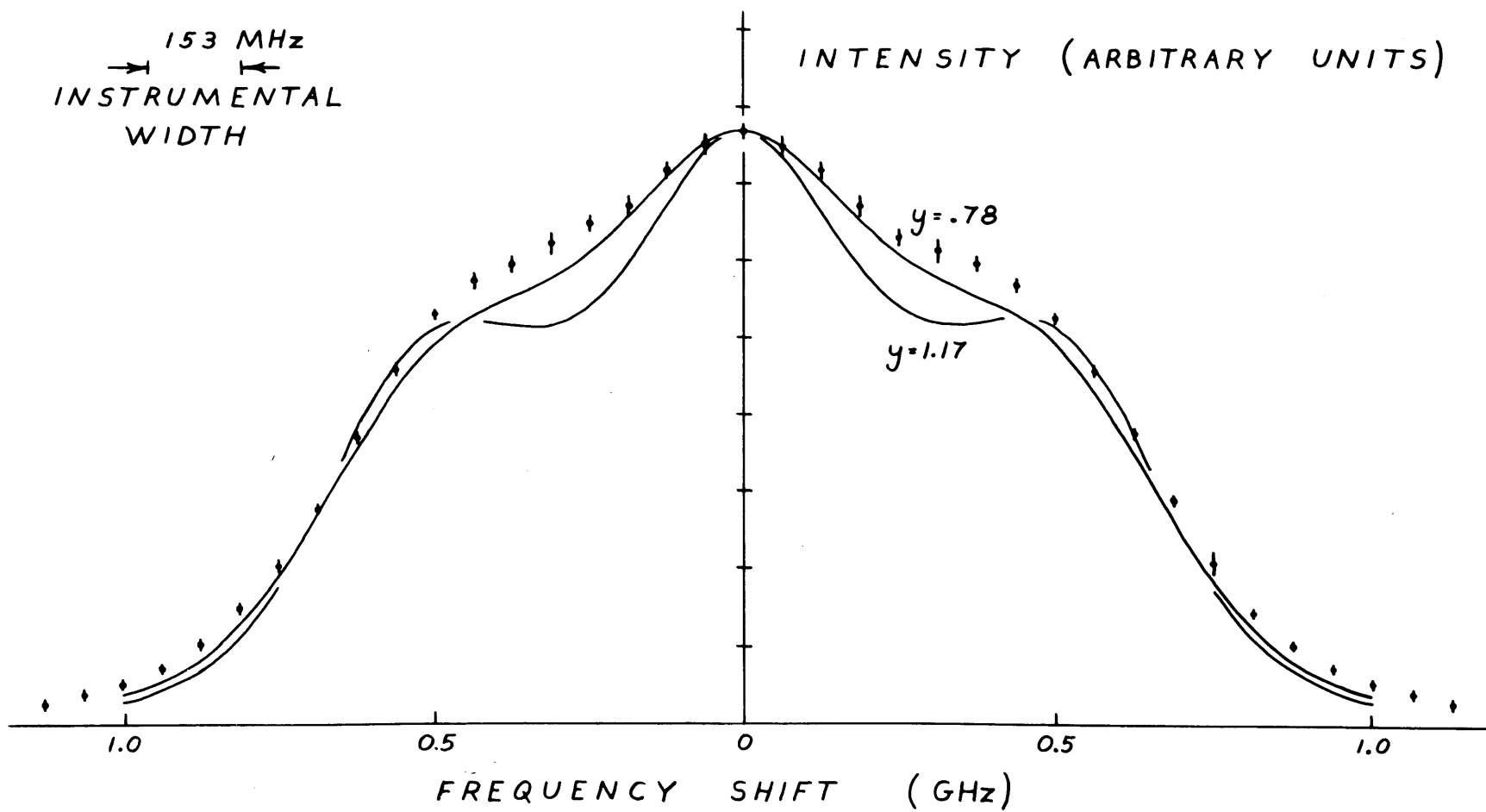


Fig. 4.11 Xe spectrum at $\theta = 169^\circ$ and the Krook model.

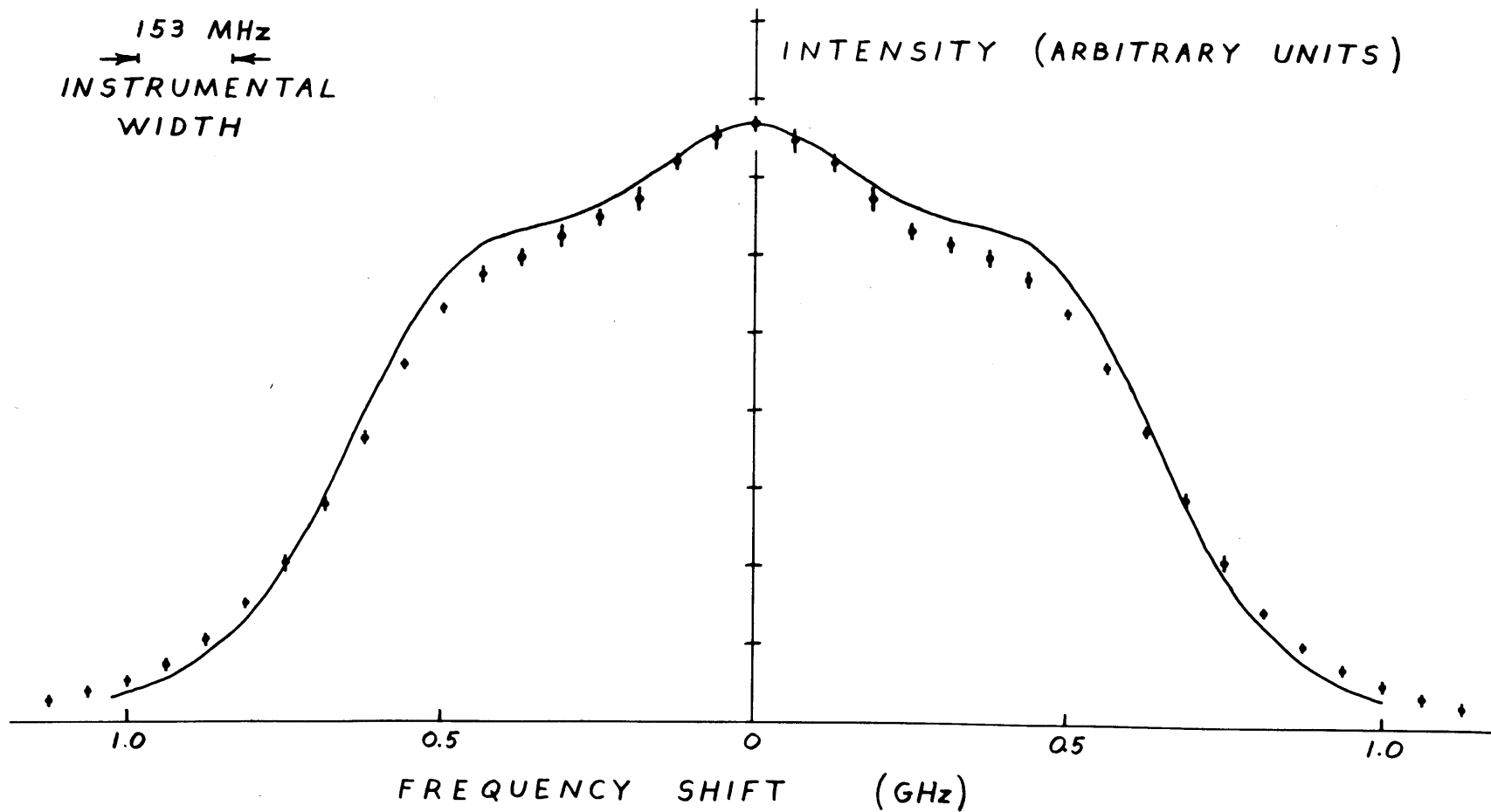


Fig. 4.12 Xe spectrum at $\theta = 169^\circ$ and the Maxwell molecule theory.

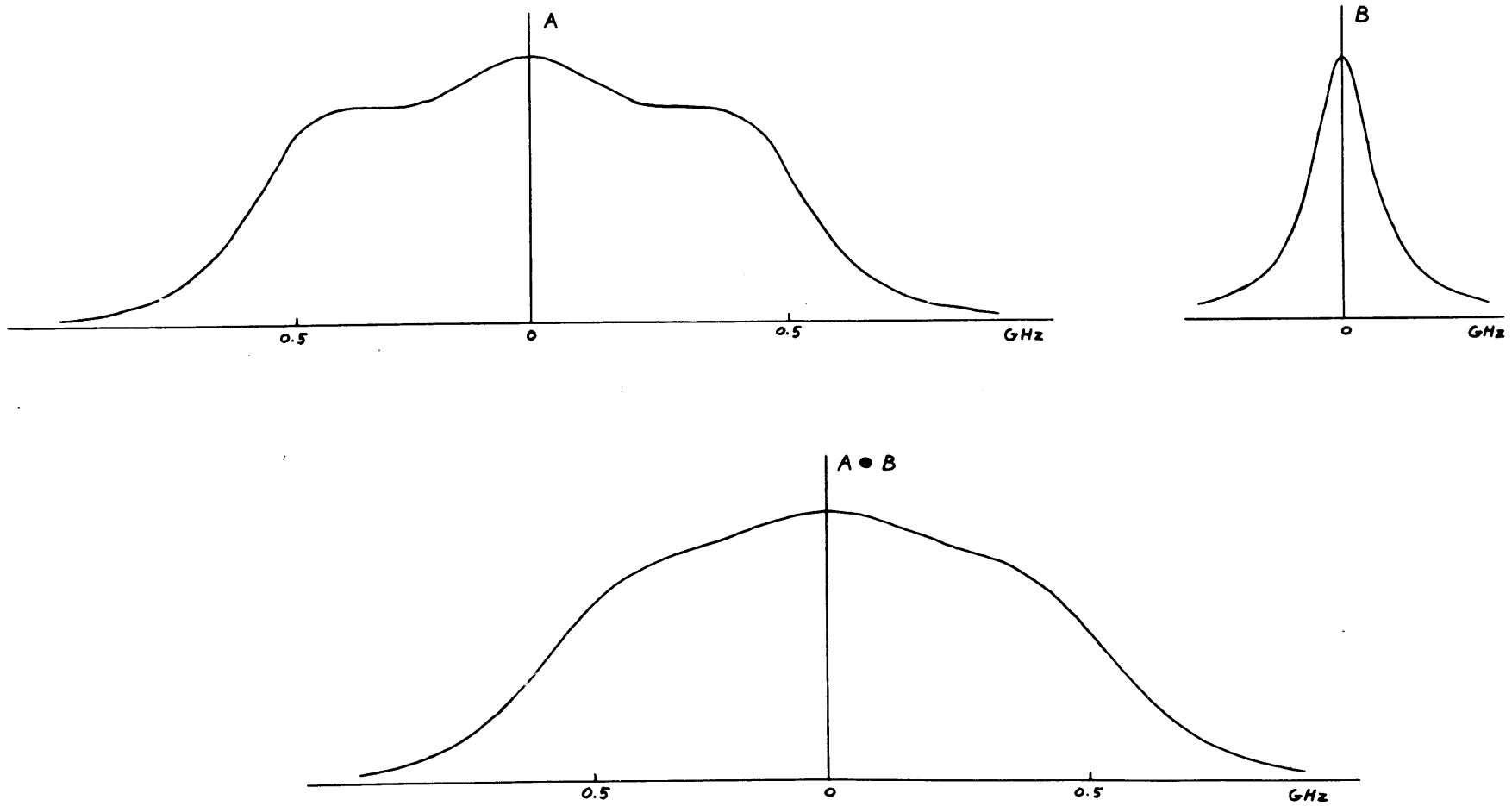


Fig. 4.13 Effect of convolution on the Maxwell molecule spectrum at $\theta = 169^\circ$.

the fraction of the power at large frequency shifts.

In figure 4.11 representing the spectrum of the Krook model there are two theoretical curves given because the value of the kinetic parameter γ cannot be determined unambiguously from the experimental conditions. The two curves correspond to γ determined from the thermal conductivity ($\gamma = .78$) and from the viscosity ($\gamma = 1.17$) according to equation 2.94.⁽¹⁴⁾ Both curves show the proper qualitative features of a 'shoulder' in the acoustic region and 'tails' which extend to higher frequencies than the hydrodynamic spectrum. The curve based on the thermal conductivity lies closer to the data than that based on the viscosity, but the agreement is not quantitative.

In calculating the value of γ to be used for the Maxwell molecule spectrum shown in figure 4.12, the value determined from the thermal conductivity and that determined from the viscosity coincide (equation 2.84 and the thermal parameters in table 2.2 are used). The resulting value of γ is 0.78⁽¹⁴⁾. The Maxwell molecule spectrum shows the qualitative features of the data. However, it over emphasizes the height at the 'shoulder' (by about 8% at 440 MHz) and seems to fall below the data in the tails of the spectrum (above about 800 MHz). These differences are small but do fall outside the estimated uncertainty in the measurements.

Figure 14.14 shows the experimental spectrum in CO_2 obtained by averaging five traces from a single run and subtracting an averaged stray light spectrum. The run was made at a temperature of 25.1°C and at a pressure of 750 mm of Hg. The reflectivity of the plates in

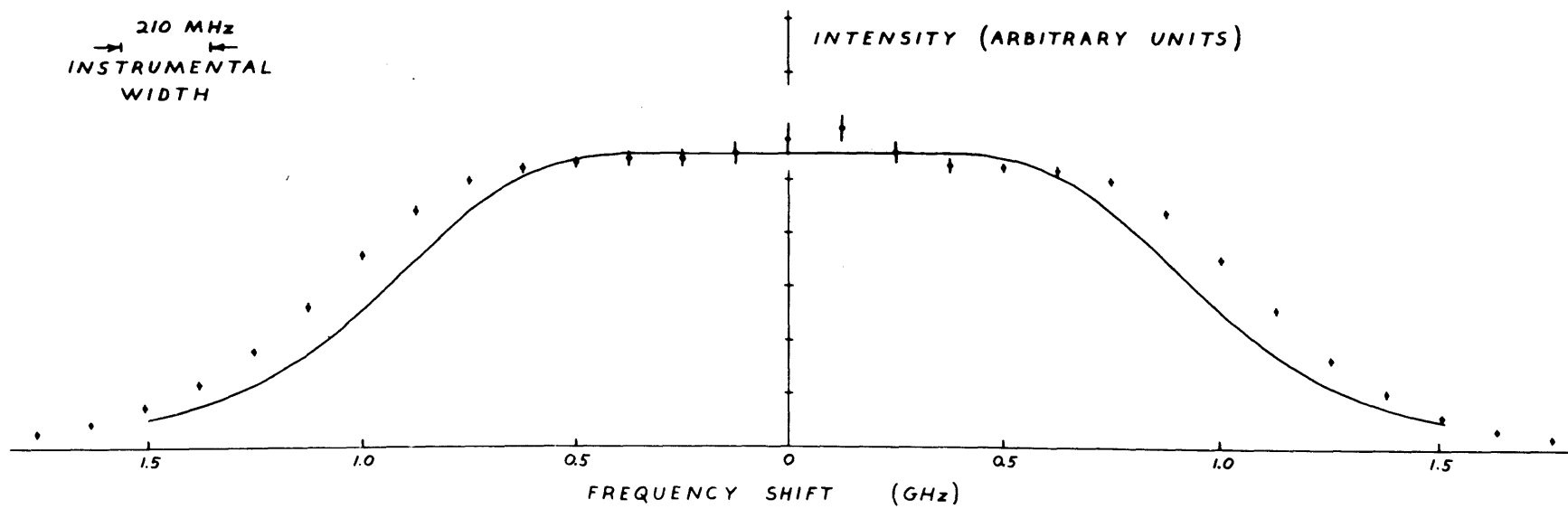
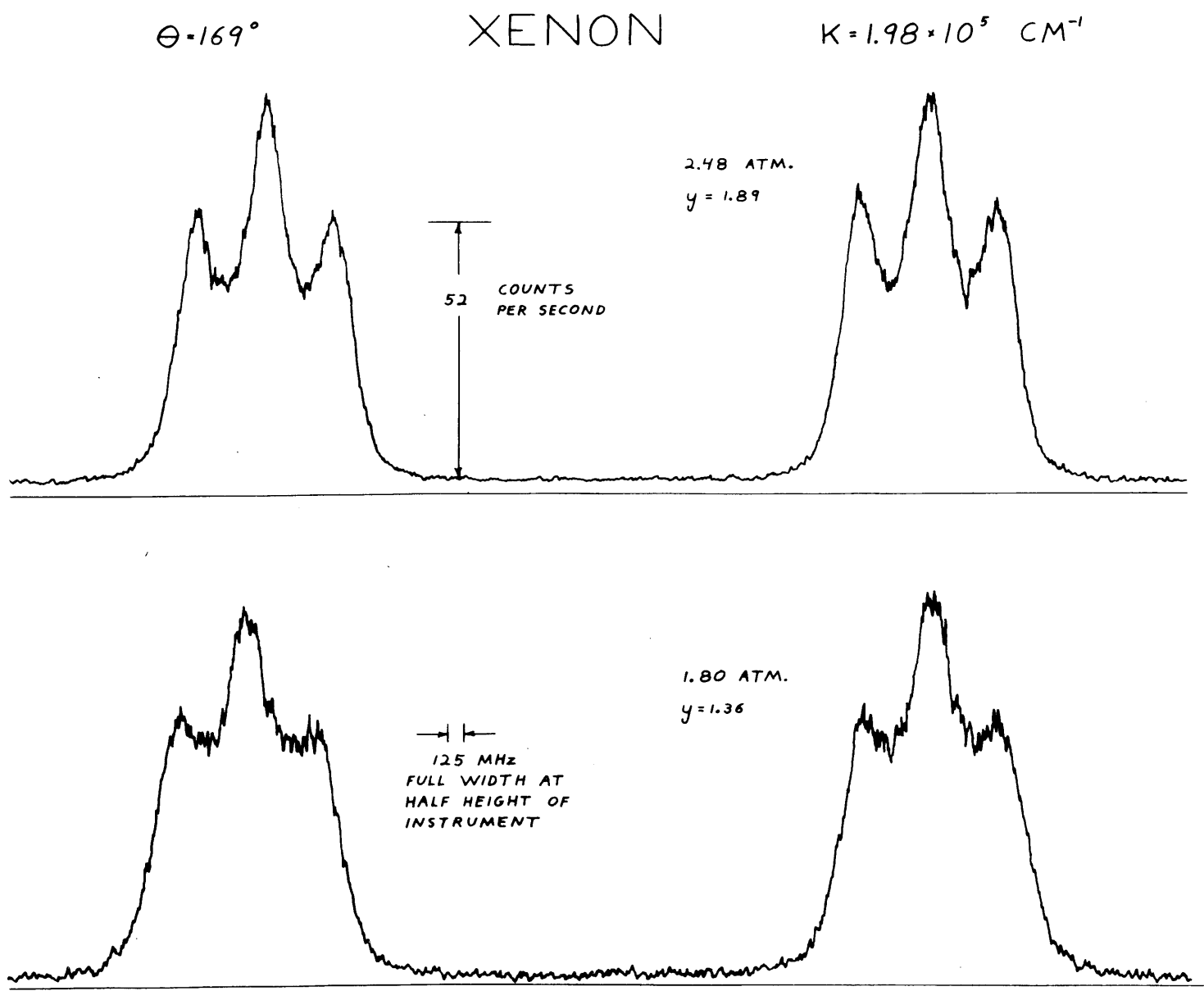


Fig. 4.14 CO_2 spectrum at $\theta = 169^\circ$ and the hydrodynamic theory.

the interferometer was decreased slightly (resulting in a broader instrumental profile) in order to increase the light gathering power. The results are compared with a theoretical hydrodynamic spectrum based on the thermal parameters from table 2.2. The hydrodynamic spectrum differs qualitatively from the data. It underestimates the amount of energy at the higher frequency shifts. The data for CO_2 cannot be compared with the kinetic theories since they are applicable only to monatomic gases.

The experiments discussed so far show that as the scattering angle is increased from 0 to 180° , at a pressure of one atmosphere, the spectrum changes from a hydrodynamic to a kinetic character. This is a result of decreasing the ratio λ_F/L by decreasing the wavelength of the fluctuation observed λ_F . It is possible, of course, to change this ratio by changing the mean free path L . In this region of pressures, L is inversely proportional to the pressure. For example the spectrum for a scattering angle of 169° can be made to regain its hydrodynamic character by increasing the pressure. This effect is illustrated in figure 4.15 which shows the experimental traces of Xe taken at pressures of 1.80 and 2.48 atmospheres corresponding to values of y of 1.36 and 1.89. The reflectivity of the plates in the interferometer has been increased slightly to increase the resolution. More extensive experiments, based on the methods introduced in this work, can take advantage of this effect. First, it will allow the value of the kinetic parameter y to be changed continuously and easily while employing only one conical lens and a fixed scattering geometry.

Fig. 4.15 Effect of a pressure increase on the spectrum of Xe at 169°.



Second, the density dependence of the scattering spectra can be investigated by comparing spectra corresponding to the same value of y , but occurring at different densities. For example a spectrum taken at $y = 3$ for $\theta = 169^\circ$ would require a pressure of about 3.8 atmospheres in Xe. At $\theta = 10.6^\circ$ $y = 3$ occurs at about .36 atmospheres. The difference in densities is about a factor of 10.

D. Calculation of the Experimental Efficiency

In Chapter III relations were derived for the detected counting rate N_D . These can be written as

$$N_D = A \sigma W \alpha P, \quad 4.4$$

where

$$A = 25 \times 10^{14} \frac{\text{cm}}{\text{watt}} \text{ for the SFP,}$$

$$A = 5 \times 10^{14} \frac{\text{cm}}{\text{watt}} \text{ for the FFP.}$$

In 4.4, σ is the cross section for scattering into a unit solid angle regardless of frequency shift, W is the fraction of the scattered spectrum falling under the instrumental profile, P is the power in watts in the laser beam, and α is the efficiency of the system relative to a perfectly aligned and adjusted lossless configuration. The factor A is based on the use of the conical lens whose half apex angle is 70° ; it therefore applies to the scattering at 10.6° and 169° . At these angles the term $\sin \phi$ in equation 2.35 can be taken as being unity, in which case σ is simply $\frac{3}{8\pi} \sigma_T$.

The calculations presented here are carried out for Xe. Using the value of σ_T given in table 2.1 one finds $\sigma = 4.49 \times 10^{-8} \text{ cm}^{-1}$. Consider first the scattering at 10.6° as shown in the Xe trace of figure 4.1. In the hydrodynamic region, one of the Brillouin components should contain a fraction $1/(2\gamma)$ of the total intensity. This is 0.30 for Xe and this value is taken to be W since the instrumental profile in this case is large compared to the intrinsic width of the Brillouin component. The power in the laser beam during this particular run was 0.66×10^{-3} watts. By substituting this information into equation 4.4 one finds that $N_D/\alpha = 22 \times 10^3$. From figure 4.1 one finds that the counting rate at the top of the Brillouin component, which is the N_D calculated here, is about 880. This leads to an efficiency α of about 4%. The peak transmission through the Fabry-Perot is limited to a figure of the order of 30% by losses in the coatings. To this loss one must add losses at the mirrors, lenses, and windows in the path of the scattered beam. These effects bring the estimated transmission of the system down to about 10%, which accounts for the major portion of the calculated efficiency.

Next, consider the backward scattering arrangement and the Xe trace shown in figure 4.9. It is estimated that at the 'shoulder' of the spectrum a lossless interferometer with the instrumental width indicated would pass about 1/10 of the power in the spectrum so $W = 0.1$. The laser power for this particular trace was 0.58×10^{-3} watts. From equation 4.4 one therefore obtains the value $N_D/\alpha = 1.3 \times 10^3$. The counting rate measured at the shoulder of the spectrum

is about 67 photoelectrons per second. This corresponds to an efficiency of 5%, in agreement with the value found in the forward scattering arrangement.

References for Chapter IV

1. S. Ranganathan and S. Yip, *Phys. Fluids*, 9, 372 (1966).
2. R. Mountain, *Rev. Mod. Phys.*, 38, 205 (1966).
3. S. Yip and M. Nelkin, *Phys. Rev.* 135, A1241 (1964).
4. P. M. Morse, *Thermal Physics* (Benjamin, N. Y. 1964).
5. H. O. Kneser, *Relaxation Processes in Gases*, in Volume II part A of *Physical Acoustics* edited by Warren P. Mason (Academic Press, N. Y. 1965).
6. J. C. Gravitt, C. N. Whetstone, and R. T. Lagemann, *J. Chem. Phys.* 44, 70 (1965).
7. M. Greenspan, *JASA* 28, 644 (1956).
8. M. Greenspan, *JASA* 31, 155 (1959).
9. The microwave modulator was built in this laboratory by J. Lunacek specifically to calibrate spectrographs and spectrometers.
10. A clear treatment of the convolution of two frequency spectra can be found in S. Mason and H. Zimmermann, *Electronic Circuits, Signals, and Systems* (Wiley, N. Y. 1960).
11. Zmuda, *JASA* 23, 472 (1951).
12. Thaler, *JASA* 24, 15 (1952).
13. B. T. Kelly, *JASA* 29, 1005 (1957).
14. The theoretical spectra for the Krook and Maxwell molecule cases shown in the first report of these experiments (T. Greytak and G. Benedek, *Phys. Rev. Lett.* 17, 179 (1966)) were based on incorrect values of γ .

Chapter V

Conclusions

The spectrum of the light scattered inelastically by five dilute gases (A, Xe, N₂, CO₂, and CH₄) has been measured. The character of the spectrum is determined by the ratio of the wavelength λ_F of the fluctuations responsible for the scattering to the mean free path L of the gas molecules. This physical ratio is about a factor of seven (depending on the exact definition of L) larger than the kinetic parameter γ defined rigorously for the various kinetic spectra.

For the monatomic gases the spectra measured in the range $\lambda_F/L \sim 60$ to 20 match those calculated on the basis of linearized hydrodynamics to within the experimental uncertainty. The spectra of the polyatomic gases in this region deviate from those calculated on the basis of the static thermodynamic parameters of the medium. The deviation is explained qualitatively using the concept of frequency dependent thermodynamic parameters first introduced to describe forced sound propagation experiments in the ultrasonic region. The velocity and lifetimes of thermally excited sound waves in the hypersonic region are deduced from the measured spectra and are in agreement with an extrapolation of the ultrasonically measured values.

The spectra measured at $\lambda_F/L \sim 5$ in Xe and CO₂ differ qualitatively from the theoretical hydrodynamic spectra, therefore allowing an upper bound to be set on the range of validity of the hydrodynamic equations. A spectrum corresponding to the exact solution of the linearized Boltzmann equation for molecules with a repulsive $1/r^4$

potential (Maxwell molecules) shows all the qualitative features of the spectrum measured for Xe, and deviates from it by no more than about 8% at any point. The quantitative differences, however, do lie outside the experimental uncertainty and are felt to reflect the non-physical nature of the Maxwell molecule potential.

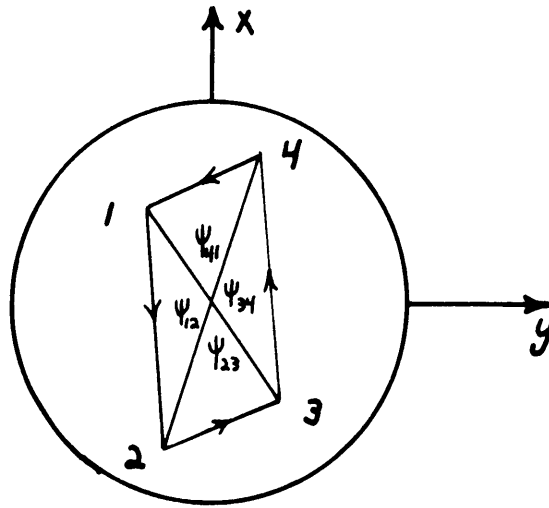
It may at first seem surprising that the experimental spectra can be fit so well by such a potential. However, it must be remembered that an exact kinetic calculation based on any nonpathological potential between molecules must give the hydrodynamic spectrum for large λ_F/L , give a Gaussian spectrum for small λ_F/L , and have a smooth transition between the two in the region $\lambda_F/L \sim 1$. Spectra computed from various kinetic equations show that the region most sensitive to the form of the potential is around $\lambda_F/L \sim 7$ (that is, where the kinetic parameter $y \sim 1$). These experiments have shown that the inelastic scattering of light in this region is capable of distinguishing between various potentials and testing the validity of equations introduced to approximate the exact Boltzmann equation.

Appendix A

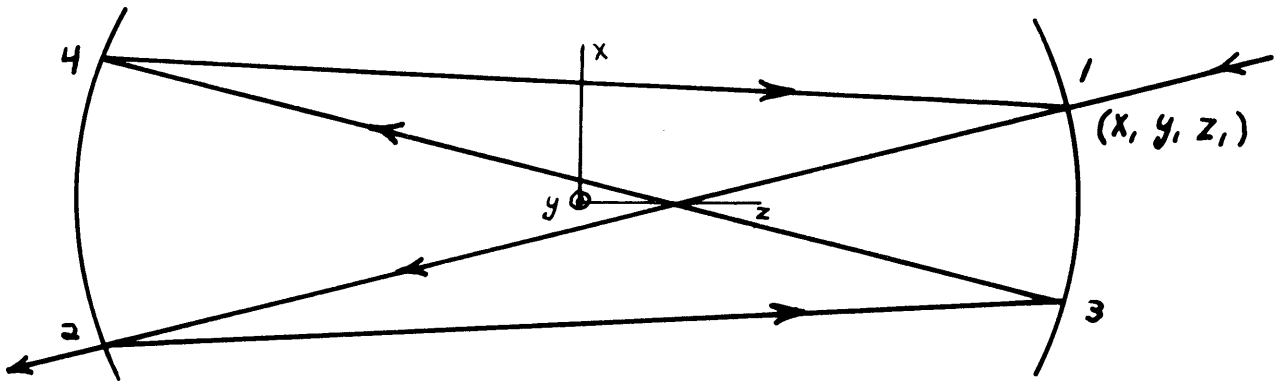
Calculation of Optical Path Lengths in the Spherical Fabry-Perot

The optical length of the interference path for an arbitrary ray entering the cavity may be evaluated most simply by a two-step procedure. First, the focusing properties of a spherical mirror are used to determine the path which the ray follows inside the cavity. In particular it is shown that after traversing the cavity four times the path closes on itself as the ray returns to the spot at which it entered the cavity. Then, by using an expression for the distance between two points on opposite mirrors, the total length of this path is computed. It is shown to differ from the value $4R$ by terms of fourth order in the displacement of the ray from the axis.

Figure A. 1 shows the path of an arbitrary ray traversing a SFP cavity as it would appear projected on an end view (a) and on a side view (b). Such a ray is shown in perspective in figure 3. 8. The ray first enters the cavity at 1 and first strikes the opposite mirror at 2. 3 and 4 indicate the other spots at which the ray will be reflected before returning to 1. It is convenient to erect on the end view of the cavity a rectangular coordinate system whose origin corresponds to the center of the mirrors. Then the point i may be represented by a two dimensional vector \vec{r}_i with components x_i and y_i where $i = 1, 2, 3,$ and 4 . \vec{r}_1 and \vec{r}_2 serve to specify the incoming ray and are the independent variables of the calculation. The vectors \vec{r}_3 and \vec{r}_4 must now be determined.



a. END VIEW OF A RAY
TRAVERSING A SFP CAVITY



b. SIDE VIEW OF A RAY
TRAVERSING A SFP CAVITY

Fig. A.1 End and side views of a ray in a spherical Fabry-Perot.

It is assumed that $|\vec{r}_i|/R \ll 1$. Path length expressions will be carried to a certain power or order of this ratio: for example $O(6)$ will indicate terms involving the sixth and higher powers of the ratio. The first mirror lies at a distance of two focal lengths from the opposite mirror and the points considered on either mirror are never far from the axis. It follows as a consequence of the geometrical optics of spherical mirrors that a spot located at 1 will be imaged into a spot at 3 given by

$$\vec{r}_3 = -\vec{r}_1. \quad \text{A. 1}$$

Similarly, the first mirror forms a real image of a spot at 2 in position 4 given by

$$\vec{r}_4 = -\vec{r}_2. \quad \text{A. 2}$$

Finally, since 3 is imaged at 1, the path closes on itself at its starting point. These results are based on the assumption that the focusing takes place without aberration. For this reason equations A. 1 and A. 2 give values of r inaccurate in $O(2)$. The deviation of the actual path length from $4R$ will be shown to be $O(4)$. Therefore these corrections to the values of r (and therefore to r/R) will contribute terms $O(6)$ to the deviation and can be neglected.

In order to calculate the length of each of the four segments of the path, a third coordinate z_i is defined as the horizontal distance of the i^{th} point from the center of the cavity. x , y , and z now form a rectangular coordinate system about the center of the cavity. The

distance s_{12} between point 1 and point 2 is then simply

$$s_{12} = \left[(x_1 - x_2)^2 + (y_1 - y_2)^2 + (z_1 - z_2)^2 \right]^{\frac{1}{2}}. \quad \text{A. 3}$$

The z 's are uniquely determined in terms of the x 's and y 's by the equation for a spherical surface:

$$(z_1 + R/2)^2 = R^2 - (x_1^2 + y_1^2) \quad \text{A. 4}$$

$$(z_2 - R/2)^2 = R^2 - (x_2^2 + y_2^2).$$

By substituting equations A. 4 into A. 3, it follows after a good deal of algebra that

$$\frac{s_{12}}{R} = 1 - \frac{1}{R^2} (x_1 x_2 + y_1 y_2) \quad \text{A. 5}$$

$$+ \frac{r_1^2 r_2^2}{4 R^4} (1 - 2 \cos^2 \psi_{12}) + o(6)$$

where ψ_{12} is the angle between \vec{r}_1 and \vec{r}_2 as shown in figure A. 1a and in figure 3. 8.

Now the total path length, $4R + \Delta l$, can be calculated:

$$\frac{\Delta l}{R} = \frac{s_{12} + s_{23} + s_{34} + s_{41}}{R} - 4. \quad \text{A. 6}$$

By using the relations $x_3 = -x_1$, $x_4 = -x_2$, $y_3 = -y_1$, and $y_4 = -y_2$ which follow from equations A. 1 and A. 2, and the fact that $\psi_{12} = \psi_{34}$ and $\psi_{23} = \psi_{41} = 180^\circ - \psi_{12}$ which are obvious from figure A. 1a, equation A. 6 can be expressed as

$$\frac{\Delta l}{R} = - \frac{r_1^2 r_2^2}{R^4} \cos 2\psi_{12} + o(6). \quad \text{A. 7}$$

The phase difference between this interference path and that of an on-axis ray is then $2 \pi \Delta l / \lambda$.

Acknowledgements

I was very privileged to have as an advisor in this work Professor George Benedek. His ability to abstract the physical meaning from complex concepts and to stimulate understanding by well pointed questions is demonstrated in the laboratory as well as in the classroom. His encouragement and criticism are gratefully acknowledged.

Professor Dan Bradley, who visited this laboratory for a month, was a boundless source of knowledge on experimental optics. It was he who suggested the use of conical optics and spherical Fabry-Perot interferometers, without which this experiment would not have been feasible.

Special thanks are due to Mr. Albert Pukt, whose skill as an instrument maker is on exhibit in every experimental set up in this laboratory. The spherical Fabry-Perot mount in figure 3.9 is only one of the many smoothly working devices he built for this experiment.

I wish to thank Professor Sidney Yip for several helpful discussions of the theory. Dr. S. Ranganathan of Cornell University gave us a copy of his Maxwell molecule program, and was kind enough to supply us with the results of his own calculations to be compared with our early data. The computations necessary for the analysis of the data were carried out on the IBM 7094 computer at the MIT Computation Center.

I wish to thank Joseph Lastovka and Paul Lazay who engineered and assembled the photon counting system. I am indebted to Dr. E. I. Gordon of the Bell Telephone Laboratories for help with the single mode laser.

The manuscript was expertly typed by Miss Carole Johnson.
Her conscientious hard work is greatly appreciated.

Finally, I wish to thank the National Science Foundation for
generous financial support during my graduate study.

Biographical Note

Thomas John Greytak was born in Annapolis, Maryland, on March 24, 1940. After attending numerous primary schools he completed secondary school in Seattle, Washington. In 1958 he entered MIT where he participated in both the honors program and the industrial cooperative program in the Department of Electrical Engineering. In February 1963 he was graduated with the degrees of Bachelor of Science and Master of Science. His academic honors include election to Eta Kappa Nu, Tau Beta Pi, and Sigma Xi. He transferred to the Department of Physics at MIT to complete his graduate work.

His professional experience consists of four summers with the Bell Telephone Laboratories at Murray Hill, New Jersey, where his master's thesis was done in the fall of 1962.

He was married on June 25, 1966, to Elizabeth Ann Bardeen of Champaign, Illinois.